

PREDICTABILITY OF
AN ATMOSPHERE WITH LARGE-SCALE
MOISTURE PATTERNS

by

DAVID ALAN SALSTEIN

S.B., Massachusetts Institute of Technology

1972

S.M., Massachusetts Institute of Technology

1973

SUBMITTED IN PARTIAL FULFILLMENT

OF THE REQUIREMENTS FOR THE

DEGREE OF DOCTOR OF

PHILOSOPHY

at the

MASSACHUSETTS INSTITUTE OF

TECHNOLOGY

August, 1976

Signature of Author.....

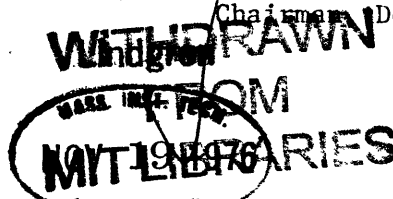
Department of Meteorology,
August 9, 1976

Certified by.....

Thesis Supervisor

Accepted by.....

Chairman, Departmental Committee
on Graduate Students



PREDICTABILITY OF AN ATMOSPHERE
WITH LARGE-SCALE MOISTURE PATTERNS

by

David Alan Salstein

Submitted to the Department of Meteorology on
9 August 1976 in partial fulfillment of the
requirements for the degree of Doctor of Philosophy

ABSTRACT

The additional error growth and concomitant decrease in predictability due to large-scale moisture patterns is examined through the use of a limited area quasi-geostrophic grid point model.

The exact patterns of latent heat release due to condensation are studied and it is demonstrated that condensation is a critical factor to the growth of errors. Predictability of condensation in the spatial sense is discussed and the dispersion in the certainty of condensation location is shown to increase with time. The contribution of condensation to imparted error energy is examined and it is shown that higher wavenumbers receive the most error energy.

The magnitude of the difference in errors between dry and moist model atmospheres amplifies in time and becomes appreciable after about three days. A statistical study of 15 pairs of model runs shows that when initial random errors of the order of $.5 \text{ m sec}^{-1}$ are inserted, "moist" errors, as measured by both error kinetic energy and square temperature error grow to an order of 20% greater than "dry" errors within several days.

The effect of various types of initial errors are discussed, in the mean and shear wind fields and in the humidity field, and it is determined that for typical errors, errors in the mean wind field are the most sensitive for predictability. It is observed also that the higher sea surface temperatures yield more rapid error growths.

Also, previous studies in the field of atmospheric predictability and related concepts are reviewed.

Thesis Supervisor: Edward N. Lorenz
Title: Professor of Meteorology

Dedicated to my parents,

Mr. and Mrs. William Salstein

Acknowledgments.

The author wishes to thank Professor Edward N. Lorenz for his advice and guidance during this study. The author feels privileged to have been able to work with Prof. Lorenz, from whom he has gained so much.

Thanks are also due to Prof. John Young, who helped in the initial stages and Dr. Cecil Leith for helpful discussions.

The National Science Foundation, under Grant # OCD74-03969, provided support. Computations were performed at the National Center for Atmospheric Research, Boulder, Colorado, which is sponsored by the National Science Foundation.

Help was given by fellow students and the staffs of the Department of Meteorology, M.I.T., and the Computation Facility of NCAR. Thanks are to be extended to Mr. Steve Ricci for his drafting of the figures and to Mrs. Susan Ary for technical assistance.

The author also worked under the late Prof. Victor P. Starr in the first years of graduate study and his guidance contributed greatly to a perspective on the science of meteorology.

Table of contents.

List of figures.	7
List of tables.	9
Chapter 1. General Introduction.	10
1.1 Past work and rationale behind current model.	12
1.2 Studies of atmospheric predictability.	13
Chapter 2. The dry and moist models.	22
2.1 Approach to model formulation.	22
2.2 The basic model equations.	24
2.3 Inclusion of moisture in model equations.	29
2.4 Conditions on ω .	34
2.5 Temperature and moisture conditions on the lower surface.	35
2.6 Lateral boundary conditions.	37
2.7 Numerical scheme.	38
Chapter 3. Results of error growth in representative model runs.	42
3.1 Determination of a relaxation constant for exami- nation of error kinetic energy growth.	49
3.2 Error growth rates from initial random errors.	54
3.3 Error growth in the coarse mesh model.	56
3.4 Error growth in the fine mesh model.	63
3.5 Initial errors in the τ field.	70

3.6 Ekman layer effect.	73
3.7 Dependence of EKE growth upon initial error magnitude.	74
3.8 Dependence of EKE growth rate on sea surface temperatures.	78
Chapter 4. Condensation regions.	84
4.1 Dispersion of condensation regions.	96
4.2 Theoretical spectrum of imparted error impulses.	103
4.3 Effect of initial errors in the humidity field.	115
Chapter 5. Statistics of error growths.	120
Chapter 6. Summary and conclusions.	127
Appendix 1. Approximation in the χ -equation.	134
Appendix 2. The best exponential and square-exponential fit for a data set.	137
Appendix 3. Spectral decomposition of error impulses.	139
Appendix 4. Derivation of the increase of moisture in saturated air.	144
References.	146
Biographical note.	153

List of figures.

2-1	Variables in the moist model.	26
3-1	Initial state of γ field	44
3-2	Initial state of θ field.	45
3-3	Initial state of σ field.	46
3-4	Initial state of ω field.	47
3-5.	Typical state of absolute humidity field, q.	57
3-6	Growth rates of error kinetic energy in the 16 x 17 grid for the dry case and moist case.	59
3-7	Fractional difference in error kinetic energy of the moist case over the dry case.	60
3-8	Long term levels of error kinetic energy in the dry and moist cases.	61
3-9	Growth rates of error kinetic energy in the fine grid for the dry case and moist case.	66
3-10	The average function E (t), the error growth of the moist over the dry case, averaged for the coarse and fine grids.	69
3-11	Growth of error kinetic energy for initial errors in the γ field for the dry and moist cases.	71
3-12	Schematic diagram of transfers of error energy.	72
4-1	Condensation regions for particular run at $t = 8 \times 10^3$ sec.	86
4-2	Condensation regions for particular run at $t = 108 \times 10^3$ sec.	87
4-3	Condensation regions for particular run at $t = 208 \times 10^3$ sec.	88
4-4	Condensation regions for particular run at $t = 308 \times 10^3$ sec.	89

4-5	Condensation regions for particular run at $t = 408 \times 10^3$ sec.	90
4-6	Condensation regions for particular run at $t = 500 \times 10^3$ sec.	91
4-7	Average fractional condensation disagreement points, and dispersion distances.	95
4-8	Fraction of condensation occurring at dispersion distances for selected time steps.	99
4-9	Error impulses as a function of wavenumber and standard deviation of Gaussian fit (one-dimensional case).	107
4-10	Error impulses as a function of wavenumber and standard deviation of Gaussian fit (one-dimensional case--half rising, half sinking).	108
4-11	Error impulses as a function of wavenumber and standard deviation of Gaussian fit (two-dimensions).	110
4-12	Error impulses as a function of wavenumber and standard deviation of Gaussian fit (two-dimensions for typical vertical velocity).	111
4-13	Error impulses as a function of wavenumber and time interval for a typical run with condensation dispersion (Two dimensional case).	113
4-14	Error kinetic energy for run with initial error in the absolute humidity field for three different amplitudes.	116
4-15	Fractional condensation disagreements for run with initial error in the absolute humidity field.	117
5-1	Relative error kinetic energy of moist and dry cases for 15 pairs of runs.	123
5-2	Relative square temperature errors for 15 pairs of runs.	124

List of tables.

1-1	Predictability times of Robinson and Lorenz.	19
2-1	The value F as a function of temperature and potential temperature at two different levels.	32
3-1	Error kinetic energy values for selected values of ϵ .	51
3-2	Successive approximations of $\chi = \nabla^2 \chi$ at five representative grid points in a Gauss-Seidel iteration scheme.	53
3-3	Growth of error kinetic energy over its initial value.	67
3-4	Error growths for initial errors of varying magnitudes.	77
3-5	Error kinetic energy growths for sea surface temperatures and experiment S1.	80
4-1	Average fractional number of condensation disagreement grid points and dispersion distances D_1 and D_2 .	94
4-2	Distribution of condensation dispersion distances.	100
4-3	Best fit curves for decaying exponential, square exponential, and standard deviation.	101
4-4	Relative EKE values for $100-350 \times 10^3$ sec for initial error in absolute humidity.	118
5-1	Average errors from a sample of 15 pairs of runs.	122

Chapter 1. General introduction.

The subject of atmospheric predictability is central to the current study of meteorology. Many researchers in the field are trying to predict future values of physical quantities by a variety of techniques, though chiefly by using numerical models of the atmosphere. The question of how far in advance it is possible to predict states of the atmosphere has been studied for quite some time, and yet there is far from any definite conclusions at the present.

The problem of weather forecasting can be identified with discovering the particular solution to a set of differential equations which describe the physics of the atmosphere and whose initial conditions are the current states of the atmospheric variables. Also, any method or set of equations used for prediction invariably involves errors because of either incomplete description of the physical equations, an inadequate set of initial conditions or numerical reasons.

Though it is often assumed that there is an inherent limit to deterministic prediction, it is not quite clear which of the physical processes are relatively more important to the growth of errors in predicted quantities and what their respective contribution to this error growth is. One of the physical processes which has definite influence upon predictability is that of moisture in the atmosphere. While it is clear that much work has been done in the field in its incorporation into the physical laws, the direct influence of large-

scale moisture patterns upon predictability has yet to be investigated.

Various studies have been done in the past in order to assess the rate of growth of errors of predicted quantities. However, it is not really clear which is the best means of attacking this problem and even which measure of errors would be most meaningful.

The method used in this work comes from the idea that the predictability of the atmosphere can be investigated by using numerical models of a fluid in order to approximate the motions and physics of the atmosphere. Two chief models are developed and referred to as the dry and moist models. For each of these models, two simultaneous runs are made starting from two different sets of initial conditions varying from each other slightly, making four runs in all (moist-A, moist-B, dry-A, dry-B). In time, the differences in the simultaneously running models spread apart from each other in both the dry and moist models, but it is seen that the manner in which the two dry solutions diverge is different from the way the two moist solutions diverge. If the two sets of initial conditions for both types of models represent "true" initial conditions and also initial conditions with an error, then the divergence of solutions represents the growth of error in time, and the different types of divergences represent "dry" and "moist" error growth.

Thus, when the relative contribution to error growths from large-scale moisture patterns is obtained, and also from future studies, when the error growths from certain other specified factors are studied, then it will be known in which direction research in meteorological predictions should proceed. In this way, the best possible results

will be obtained from predictions.

It is helpful to look at past studies in the field of predictability to understand some of the concepts involved and to see the varied approaches to the problem which have been undertaken.

1.1 Past work and rationale behind current model.

In the past, a number of various approaches have been taken to examine the problems of atmospheric predictability and inherent growth of errors in predicting future states of the atmosphere. Some of the chief areas of interest have been (1) the application of turbulence theory to discover predictability times of many scales of motion, (2) the use of large general circulation models in order to discover factors about the nature of atmospheric predictability, and (3) the different nature of predictability in barotropic and baroclinic flows.

In general, most of the theoretical studies have dealt with predictability of a "dry" atmosphere, without the effects of moisture, while the studies using the general circulation models are attempts to simulate the atmosphere in as much detail as possible. While the theoretical turbulence models might not be close enough to the atmosphere to simulate important other physical processes, the studies using the full general circulation models sometime make a basic understanding of atmospheric processes difficult, because of their

complexity. Therefore, it was decided here to develop a straightforward and not too complex model which includes those processes which are necessary for an investigation of the problem.

1.2 Studies of atmospheric predictability.

Early studies of the error growths in the sense of predictability were reported by Charney et. al. (1966) relating the success of the then current versions of general circulation models. In order to estimate the period of time in which an error perturbs atmospheric flow, numerical experiments were done by Leith (1964), Mintz (1965), and Smagorinsky (1963) in which small perturbations were placed in the temperature fields. Although the models themselves did not agree with each other, a reasonable conclusion was that the growth in mean square temperature error was a factor of two in five days. The general predictability times were limited to two weeks in the general circulation models.

Smagorinsky (1969) concluded that the deterministic limit of synoptic scale predictability was three weeks, although the practical limit of the modeling at the time was no more than one week. This study was based upon integration of pairs of states in a numerical model with initial conditions only slightly different from each other.

More current general circultaion models have been used to study

predictive error growth and are based upon the primitive equations of motion. (e.g. Somerville et. al., 1974, Holloway and Manabe, 1971, Kasahara and Washington, 1971, Mintz, 1968, Arakawa, 1970). The Mintz-Arakawa model, for one, studied random errors, sinusoidal errors, and localized errors. It was found that the localized errors grew most rapidly. As an example, the winter RMS error in the upper level grew from 0.2 to 0.9 °K in 10 days, where a random disturbance caused growth from 1.5 to 4.0 and a sinusoidal disturbance from 0.4 to 1.0.

The nature of initial conditions in the problem of predictability of a dry atmosphere was investigated by Thompson (1957). He studied the growth rates of inherent errors in prediction and their dependence upon the characteristic scale of initial error fields, the vertical wind shear, static stability, and various other factors. Barotropic and baroclinic flows tend to be similar but strongly baroclinic initial states are considerably modified by the thermodynamic processes. The error growth can be expressed in equation form, the most significant implication from which is that the growth of errors is sensitive to the scales of the errors, as well as the scales of fluctuations in the flow patterns. If the scale of the initial error were appreciably greater than that of the fluctuations in flow, then error increases even more rapidly. A figure of 7.7 days is obtained for the growth of errors to the point at which the mean square error of fluctuations reaches that of two random states.

The concept of predictability is related to the periodic or non-periodic nature of the atmosphere itself. (see Lorenz, 1963). By the use of finite systems of ordinary differential equations, it was found that for systems of equations with bounded solutions, non-periodic solutions are ordinarily unstable with respect to small perturbations. Thus, solutions of equations whose initial states were slightly different would evolve into different states. This line of thought led to the approach of trying to determine what types of atmospheric states might be analogues of each other (Lorenz, 1969a) as a means of studying predictability. Two states were taken to be analogues if their 200-, 500-, and 850-mb height values at certain hemispheric grid points were close enough in the mean square sense within a five year period. In that study, no truly good atmospheric analogues were discovered. However, the smallest error between analogues took 8 days to double, but an extrapolation revealed that very small errors would take 2.5 days to double.

As a followup study (Lorenz, 1973), it was found that atmospheric states within 12 days of each other were found to be closer to each other than two randomly selected states, in the values of the three height fields and so this was proof that there is at least some predictability within 12 days, however small.

Lorenz (1965), using a three wave model, did experiments to deduce the predictability of flows in a low-order model. Using a linear method to discover the growth of errors, amplification rates of errors for a 64-day forecast were determined. The errors grew at

different rates in different periods and there were even some in which they diminished.

Fleming (1971) investigated the predictability of barotropic and baroclinic flows in a study using a method known as stochastic dynamic prediction and the spectral set of equations in a dry model. He found that error growths were essentially independent of the initial conditions. The predictability of wave number 12, which was used as a reference point and a minimum requirement for useful synoptic forecasts, had a predictability value of 1.5 days. However, these were lengthened in the large scale by addition of forcing and dissipation terms.

Perhaps the most pioneering and remarkable study of predictability was performed by Lorenz (1969b) in which the intrinsic range of atmospheric predictability for each scale was derived. This was based upon a spectral analysis of the barotropic vorticity equation and the use of a turbulence closure assumption that quadratic functions of the error and flow fields are independent. From these equations, an equation whose dependent variables are ensemble averages of error energy in separate scales of motion are derived. Resulting maximum predictability times of several scales are as follows: The cumulus scales in this study have a range of a few days, and the largest scale has some predictability until 16.8 days. Furthermore, this study seems to indicate by extrapolation that even with an arbitrarily small error in an arbitrarily small scale, the range of predictability is not significantly lengthened and is still about 16.8 days.

In addition, errors confined to any scale lead in a short period of time to errors in the smallest scales even if they were not present initially, and these errors behave as if they were there initially and amplify accordingly.

Some of the more recent studies of atmospheric turbulence have been applied to the study of instability and predictability. Leith (1971) used a model known as the eddy-damped Markovian model of two-dimensional turbulence to investigate error growth. This study was based upon the recognition that the atmosphere on the largest scale behaves somewhat like a two-dimensional incompressible fluid, and that the energy contained in this system obeys a -3 power law.

Error growth calculations of Leith show that the predictability of the atmosphere would lengthen by about one day for each factor of two increase in the resolution of observations. However, an uncertainty would seem to be dependent upon a dimensionless coefficient which is added to match observations.

Kraichnan (1970) used the statistical methods of turbulence and an approximation in order to determine a spectrum of error growth, that is, a deviation of two statistically similar flows. Numerical solutions of equations were obtained for the deviation spectrum $D(k,t)$, which represents error growth, where k is the wavenumber and t is time, in order to determine whether the spectrum $D(k,t)$ would grow or damp in time. For a very low Reynolds number (high viscosity), $D(k,t)$ did damp, and for a higher Reynolds number the growth and decay depended upon specific input and output integrals from various wavenumbers for

the case considered. He concluded that at larger wavenumbers for steady state, with $D(k,t) > 0$, $D(k,t)$ would grow until it reached the total kinetic energy of the spectrum, called $E(k,t)$.

Leith and Kraichnan (1972) did a further study trying to determine the predictability of turbulent flows in both two and three dimension. It was found that using a closure approximation known as the test-field model, for two- and three-dimensional turbulence, errors initially confined to high wavenumbers spread into the lower wavenumber range in a well-defined manner.

Robinson (1971) expanded upon the studies of predictability by considering the additional effects of dissipation upon flows. His results were dependent as well upon scale size, because the hypothesis was made that dissipation can be described by a virtual coefficient of viscosity K , which is a function of the scale.

The predictability times were similar to those of Lorenz (1969b), although the means of obtaining the results were quite different. Robinson concludes that the method of Lorenz, including many scales of motion through the imposition of an energy spectrum, actually contains the dissipation which otherwise is inserted parameterically.

For two particular flow fields, a simple one (S)

$$u = \sum_{l=1}^{l_{max}} a_l \cos 2\pi l y \quad v = \sum_{l=1}^{l_{max}} a_l \sin 2\pi l x$$

and a more complex one (C)

$$u = \sum_{l=1}^{l_{max}} a_l \cos 2\pi l x \sin 2\pi l y \quad v = - \sum_{l=1}^{l_{max}} a_l \sin 2\pi l x \cos 2\pi l y$$

are considered. Robinson studied a predictability time in two different manners, (1) that of the average time taken for matter at the center of a circle of radius of the scale to diffuse to the boundary in terms of the virtual diffusion coefficient K appropriate to the scale, and that of (2) the average time for 50 per cent dilution of the matter within the boundary of such a circle based upon dissipation. The estimates for his two flow fields and the results of the Lorenz study are shown in Table 1-1, and it can be seen that the second definition (2) of predictability time yields a more similar estimate to that of Lorenz.

Table 1-1

Predictability times of Robinson and Lorenz.

<u>l^{-1}</u> (km)	<u>S-1</u>	<u>C-1</u>	<u>S-2</u>	<u>C-2</u>	<u>Lorenz</u>
10	7 hours	5 hours	1.5 hours	1 hour	1 hour
100	1.5 hours	1.5 hours	6 hours	6 hours	4 hours
1000	7 days	6 days	1.5 days	1 day	1 day
10,000	50 days	42 days	9 days	8 days	5.5 days

The techniques of modeling itself and the use of acquired data play a large role in the errors of predicted quantities, and this is a separate issue within the general predictability question.

In a primitive equation model, for example, Blumen (1976) has used a divergent barotropic model to study atmospheric predictability. He found that a major cause of the decay of predictability was the utilization of initialization schemes with errors, although error growth was essentially independent of which type of initialization scheme was employed. This study also attempted to show that improper initialization leads to exchange in energy between geostrophic and ageostrophic modes.

The use of constant observing systems to "update" observations can certainly reduce error growth and there have been several studies with the hope of finding maximum predictability times and error growth rates in more real situations. Some studies have been made using GCM's to determine error growth in predictions with a view towards more practical uses of observing systems. Jastrow and Halem (1970), in calculations for the first GARP Global Experiment, used the Mintz-Arakawa model to study the effect of constant insertion of global temperature data from a satellite. From the model, it was found that the average errors in the wind field which start at 0.5 m sec^{-1} grow to 6 m sec^{-1} within 10 days, but with continuous updating of temperatures from simulated satellite data, the wind errors level off at 2 m sec^{-1} , and this is a factor of only 4 times as great. In a further report, Jastrow and Halem (1973) tried to determine predictive errors

based upon a more full observing system.

Kasahara (1972) and Williamson and Kasahara (1971) describe predictability experiments with the NCAR General Circulation Model; they found a two to three day doubling time of small errors. They did updating experiments by constant insertion of temperatures or winds and found that the rms error fields are reduced in both cases.

While predictability of atmospheric motions and variables in the present context does seem to be limited, there is at present work being done on prediction of statistical quantities in order to see how long term atmospheric quantities might respond to changes in parameters. As an example, Warshaw and Rapp (1973) discussed error growth in numerical models and tried to determine whether changes in boundary conditions affect longer term average conditions of a model. Despite the fact that small errors destroyed the predictive capacity for each of the two cases of boundary conditions (which was presence and absence of ice), the difference of the longer term (30 day) solutions between the two boundary condition cases was statistically noticeable. This and other studies show that the traditional connotation of "predictability" might not hold on the average for longer term and climatic periods.

Thus there are many complex issues to be studied in the theory of predictions on the short and long term. These must be resolved in order to bring the predictions upon to their potential.

Chapter 2. The dry and moist models.

2.1 Approach to model formulation

The model which has been constructed is used for the purposes of a predictability study. In this method of studying predictability, two initial states are composed which are very similar to each other, and differing by only a small quantity in some of the variables. The model is then advanced in time by numerical means starting with both states as initial conditions.

For each time step, it is possible to compare the different states of the model with each other. If the models are far apart from each other in some measure, it is said that the predictability at this time is small, but if the models are relatively close to each other, the model is still considered predictable.

Since the chief purpose of this study is to assess the effects of large scale moisture patterns upon the growth of errors and the range of predictability of a quasi-geostrophic grid point model, as many factors which are important for the description of the phenomena should be included, but it would not be desirable to further introduce effects or approximations which could overshadow the actual phenomena to be studied.

Both a dry and moist model have been developed for this predictability study. In each of these two cases, two simultaneous runs are made starting from similar initial conditions in order to obtain

estimates of "dry" and "moist" predictability.

Let it be assumed that the inclusion of a certain factor is essentially independent with respect to the phenomenon of large scale condensation. Although it might introduce greater amounts of unpredictability, presumably it would introduce similar quantities of this unpredictability in both the dry and moist models. However, there is a chance that the inclusion of this factor might actually cause some spurious growths of unpredictability because the modeling of each factor is not quite exact. Thus, if a certain factor is not actually necessary to a description of general large scale dynamics, thermodynamics, and water vapor phase change and motions, it is best that it be omitted.

For reasons to be discussed later, it is believed that the role of condensation is instrumental to the growth of additional errors in the moist model. This actual condensation phenomenon is modeled at grid points when conditions are appropriate, and furthermore, this is done in the large scale only. Since the effects of smaller scale phenomena, for example, that of cumulus clouds, cannot be directly calculated, except in the case of an extremely fine grid, they would have to be approximated by means of parameterizations. Since all methods of cumulus parameterization are certainly inexact, their inclusion could overshadow that which it is wished to study; the result could be that a parameterized type of predictability study is less valuable than a large scale one.

2.2 The basic model equations.

The model which has been developed for the purpose of this predictability study is a two-layer quasi-geostrophic model with a variable number of horizontal grid points. The model is based chiefly on Lorenz (1960). The two-layer version of this model integrates in time the sums and differences of both the streamfunction and potential temperatures in the upper and lower layers. The model has variable static stability, in that the difference between the potential temperatures of two vertical levels is a variable.

The original set of dry equations is as follows:

$$\frac{\partial \theta}{\partial t} = -J(\psi, \theta) - J(\tau, \sigma) + \nabla \cdot \sigma \nabla \chi \quad (2.1)$$

$$\frac{\partial \sigma}{\partial t} = -J(\psi, \sigma) - J(\tau, \theta) + \nabla \theta \cdot \nabla \chi \quad (2.2)$$

$$\frac{\partial}{\partial t} \nabla^2 \psi = -J(\psi, \nabla^2 \psi + f) - J(\tau, \nabla^2 \tau) \quad (2.3)$$

$$\frac{\partial}{\partial t} \nabla^2 \tau = -J(\psi, \nabla^2 \tau) - J(\tau, \nabla^2 \psi + f) + \nabla \cdot f \nabla \chi \quad (2.4)$$

$$b c_p \nabla^2 \theta = \nabla \cdot f \nabla \tau \quad (2.5)$$

The boundaries between the layers are pressure surfaces p_0 , p_2 , and p_4 , and the centers of the lower and upper layers are p_1 and p_3 , respectively. The pressures are defined as

$$p_n = 1000 - 250n \quad \text{in mb}$$

The variables used in equations (2.1) - (2.5) are the mean potential temperature, θ , the static stability, σ , the streamfunction for the mean flow, ψ , the streamfunction for the shear flow, τ , and the velocity potential of the lower layer, χ . In this case, the potential temperatures in the upper and lower layers are $\theta_3 = \theta + \sigma$ and $\theta_1 = \theta - \sigma$ respectively, and the streamfunctions in the upper and lower layers are $\psi_3 = \psi + \tau$ and $\psi_1 = \psi - \tau$. (See Figure 2-1).

Here J refers to the Jacobian function

$$J(f, g) = \frac{\partial f}{\partial x} \frac{\partial g}{\partial y} - \frac{\partial g}{\partial x} \frac{\partial f}{\partial y}$$

and the factor b is

$$b = \frac{1}{2} [\rho_1^\kappa - \rho_3^\kappa] = \frac{1}{2} \left[\left(\frac{3}{4}\right)^\kappa - \left(\frac{1}{4}\right)^\kappa \right] \approx 0.124$$

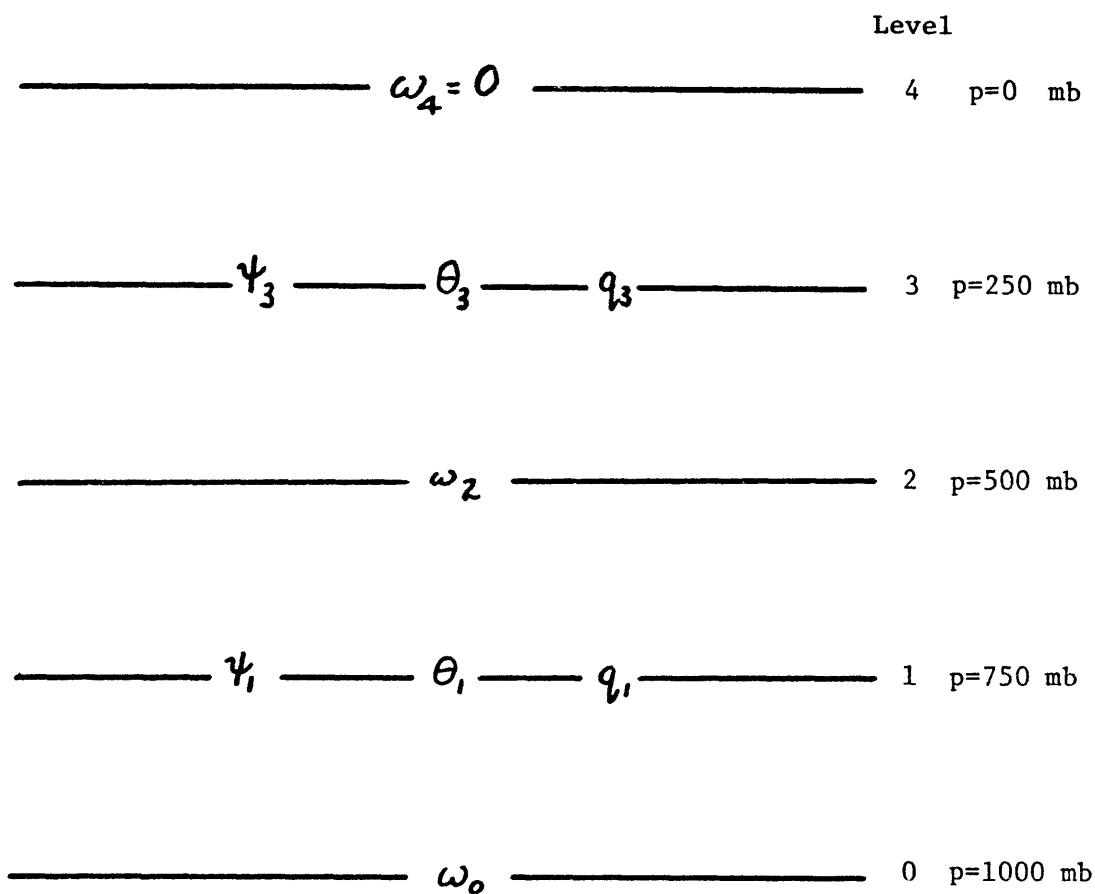
where κ is the ratio $(c_p - c_v)/c_p \approx 2/7$.

If the Coriolis parameter is considered to be a constant (an f-plane approximation), equation (2.5) becomes

$$b c_p \nabla^2 \theta = f \nabla^2 \tau \quad (2.6)$$

otherwise known as the thermal wind relationship.

If the ∇^2 operator is applied to equation (2.1) and if this is taken with equations (2.4) and (2.6) with fixed f, the following diagnostic " ω -equation" results:



$$\psi = (\psi_3 + \psi_1) / 2$$

$$\tau = (\psi_3 - \psi_1) / 2$$

$$\theta = (\theta_3 + \theta_1) / 2$$

$$\sigma = (\theta_3 - \theta_1) / 2$$

Figure 2-1. Variables in the moist model.

$$\nabla^2 \nabla \cdot \sigma \nabla \chi - \frac{f^2}{b c_p} \nabla^2 \chi = \tag{2.7}$$

$$\nabla^2 [J(\psi, \theta) + J(\tau, \sigma)] - \frac{f}{b c_p} [J(\psi, \nabla^2 \tau) + J(\tau, \nabla^2 \psi)]$$

Equation (2.7) can be used as an identity for the solution of χ when all the other variables are known.

The approximation

$$\nabla^2 \nabla \sigma \cdot \nabla \chi \ll \nabla^2 \sigma \nabla^2 \chi$$

is made in order to reduce the left hand side of equation (2.7) to

$$\nabla^2 (\sigma \nabla^2 \chi) - \frac{f^2}{b c_p} \nabla^2 \chi.$$

This enables one to solve for χ in two distinct steps first by solving for $\nabla^2 \chi$ and subsequently by determining the χ field from $\nabla^2 \chi$. The validity of this approximation is discussed in Appendix 1.

Before the method of solution of equations (2.1) - (2.7) will be used, it is desired that they be placed into a non-dimensional form, and this is illustrated below.

The following are considered to be characteristic values for the variables. For convenience, these characteristic values are chosen only as powers of 10.

x, y (=D)	100 km
p	10 ³ mb
t	10 ³ sec
ψ, τ	1 km ² sec ⁻¹
∇ ² ψ, ∇ ² τ	10 ⁻⁴ sec ⁻¹
θ, σ	1 °K
χ	10 ⁻² km ² sec ⁻¹
f	10 ⁻⁴ sec ⁻¹
c _p	10 ⁷ cm ² sec ⁻² (°K) ⁻¹
b	10 ⁻¹

and in this manner, the non-dimensional form of the equations become

$$\frac{\partial \theta_N}{\partial t_N} = 10^{-1} [-J_N(\psi_N, \theta_N) - J_N(\tau_N, \sigma_N)] + 10^{-3} [\nabla_N \cdot \sigma_N \nabla_N \chi_N] \quad (2.8)$$

$$\frac{\partial \sigma_N}{\partial t_N} = 10^{-1} [-J_N(\psi_N, \sigma_N) - J_N(\tau_N, \theta_N)] + 10^{-3} [\nabla_N \theta_N \cdot \nabla_N \chi_N] \quad (2.9)$$

$$\frac{\partial}{\partial t} \nabla_N^2 \psi_N = 10^{-1} [-J_N(\psi_N, \nabla_N^2 \psi_N) - J_N(\tau_N, \nabla_N^2 \tau_N)] \quad (2.10)$$

$$\frac{\partial}{\partial t} \nabla_N^2 \tau_N = 10^{-1} [-J_N(\psi_N, \nabla_N^2 \tau_N) - J_N(\tau_N, \nabla_N^2 \psi_N)] + 10^{-3} \nabla_N \cdot f_N \nabla_N \chi_N \quad (2.11)$$

$$b_N c_{pN} \nabla_N^2 \theta_N = f_N \nabla_N^2 \tau_N \quad (2.12)$$

$$\nabla_N^2 \sigma_N \nabla_N^2 \chi_N - \frac{f_N^2}{b_N c_{pN}} \nabla_N^2 \chi_N \quad (2.13)$$

$$= 10^2 \nabla_N^2 [J_N(\psi_N, \theta_N) + J_N(\tau_N, \sigma_N)] - 10^2 \frac{f_N}{b_N c_{pN}} [J_N(\psi_N, \nabla_N^2 \tau_N) + J_N(\tau_N, \nabla_N^2 \psi_N)]$$

where the N subscript, to be dropped later denotes non-dimensional form.

2.3 Inclusion of moisture in model equations.

Moisture is added to the set of dry equations by inclusion of terms q_1 and q_3 for specific humidity in the lower and upper layers, respectively. The equations for the rate of change of q_1 and q_3 with time are as follows:

$$\frac{\partial q_1}{\partial t} = -J(\psi, q_1) + J(\tau, q_1) - \omega_1 \frac{\partial q}{\partial p} - \dot{q}_c + \dot{q}_E \quad (2.14)$$

$$\frac{\partial q_3}{\partial t} = -J(\psi, q_3) - J(\tau, q_3) - \omega_3 \frac{\partial q}{\partial p} - \dot{q}_c \quad (2.15)$$

Here the term \dot{q}_c refers to the loss of q_1 due to condensation and \dot{q}_E refers to the addition of q_1 into the lower layer resulting from evaporation from the bottom surface, and ω_1 and ω_3 are vertical velocity values at levels 1 and 3. The vertical transport terms $\omega \frac{\partial q}{\partial p}$ are rather difficult to model because the numerical form of the vertical derivative is not straightforward. One can assume that the humidity follows several types of profiles in the vertical. Two possible profiles, both of which are tried in the modeling scheme are linear and logarithmic in pressure. In the linear scheme

$$q = q_3 + \frac{p - p_3}{p_1 - p_3} (q_1 - q_3) \quad \text{and} \quad \frac{\partial q}{\partial p} = \frac{q_1 - q_3}{p_1 - p_3}$$

while in the logarithmic case,

$$\log q = \log q_3 + \frac{p-p_3}{p_1-p_3} \log \frac{q_1}{q_3} \quad \text{and} \quad \frac{\partial q}{\partial p} = \frac{\log \frac{q_1}{q_3}}{p_1-p_3} (p_1-p_3) \log(q_1/q_3)$$

Both these profiles were tried and led to insignificant differences in predictability error results. Since the true profile is usually somewhere in between, the more straightforward linear profile is used in the model equations.

In non-dimensional terms, where the q 's are in units of grams of water vapor per kilogram of dry air and ω is in units of 10^{-3} mb sec⁻¹, the equations appear as follows

$$\frac{\partial q_{1N}}{\partial t_N} = -10^{-1} [J_N(\psi_N, q_{1N}) - J_N(\tau_N, q_{1N})] - 10^{-3} \omega_{1N} \frac{q_1 - q_3}{p_1 - p_3} - \dot{q}_{C1N} + \dot{q}_{EN} \quad (2.16)$$

$$\frac{\partial q_{3N}}{\partial t_N} = -10^{-1} [J_N(\psi_N, q_{3N}) + J(\tau_N, q_{3N})] - 10^{-3} \omega_{3N} \frac{q_1 - q_3}{p_1 - p_3} - \dot{q}_{C3N} \quad (2.17)$$

The presence of water vapor and its role in condensation also influences the forms of the other equations because of the liberation of heat during the condensation process, and this is added to the equations as follows.

Haltiner (1971) gives as a formulation the following form for the increase of saturated specific humidity q_s :

$$\frac{dq_s}{dt} = \frac{\delta F}{p} \omega \quad (2.18)$$

where
$$F = q_s T \left(\frac{L R - c_p R_v T}{c_p R_v T^2 + q_s L^2} \right)$$

This is derived from the Clausius-Clapeyron relation in Appendix 4, assuming that condensation occurs as a result of saturated adiabatic expansion.

Furthermore, it is assumed that upward motion must occur at the same time during which the humidity is almost at saturation. Thus, the following condition determines when the on-off δ factor is 1 or 0 (condensation does or does not occur):

$$\begin{aligned} \delta &= 1 \quad \text{for } \omega < 0 \quad \text{and} \quad q \geq \alpha q_s \\ \delta &= 0 \quad \text{for } \omega \geq 0 \quad \text{or} \quad q < \alpha q_s \end{aligned}$$

In this study α is a critical relative humidity factor which is taken to be .8 following Krishnamurti et. al. (1971) and others. Requiring that condensation occur at a 100% relative humidity would lead to too little condensation. Since the grid point is only one point in the center of a square, it is quite possible that condensation is occurring within the square, although the relative humidity is less than 100% at the central point. A factor of .8 is chosen as a threshold necessary for condensation. However, a functional form for δ as a function of the actual relative humidity q_{rel} , as q_{rel} varies from 0 to 1 could also be proposed.

If latent heat H is being released at level i the following relationship shows that the temperature is being raised accordingly

$$\begin{aligned} c_p \left(\frac{P_i}{P_o} \right)^{\kappa} \frac{d\theta_i}{dt_{cond}} &= c_p \frac{dT_i}{dt} - \frac{RT_i}{P_i} \omega \\ &= L_i \frac{dq_s}{dt} = - \frac{L_i \delta_i F_i}{P_i} \omega_i \end{aligned}$$

and furthermore, since $\nabla^2 \chi = -\frac{\partial \omega}{\partial p}$, from the equation of continuity, the quantities $\omega_1 \approx \omega_3 \approx \omega_2/2$ are expressed as $\omega_1 \approx \omega_3 \approx \nabla^2 \chi / 4$. Adding and subtracting expressions for $\frac{d\theta_i}{dt}$, it is found that the right side of the expression for $\frac{\partial \theta}{\partial t}$ and $\frac{\partial \sigma}{\partial t}$ contain the additional terms

Temp (°C)	θ (°K)	F_3	Temp (°C)	θ (°K)	F_1
-69	303.1	.000074	-10	285.5	.0066
-68	304.6	.000085	-9	286.6	.0070
-67	306.1	.000097	-8	287.7	.0073
-66	307.6	.000112	-7	288.8	.0077
-65	309.0	.000128	-6	289.9	.0081
-64	310.5	.000146	-5	291.0	.0085
-63	312.0	.000167	-4	292.0	.0089
-62	313.6	.000191	-3	293.1	.0093
-61	315.0	.000217	-2	294.2	.0097
-60	316.5	.000247	-1	295.3	.0102
-59	319.5	.000281	0	296.4	.0106
-58	320.9	.000319	1	297.5	.0110
-57	322.4	.000361	2	298.6	.0115
-56	323.9	.000408	3	299.6	.0119
-55	325.4	.000461	4	300.7	.0123
-54	326.9	.000520	5	301.8	.0128
-53	328.4	.000586	6	302.9	.0132
-52	329.9	.000659	7	304.0	.0136
-51	331.4	.000740	8	305.1	.0140
-50	332.8	.000829	9	306.2	.0145
-49	334.3	.000928	10	307.2	.0149
-48	335.8	.001038	11	308.3	.0153

Table 2-1. The value F as a function of temperature and potential temperature at two different levels.

$$\frac{\partial \theta}{\partial t} = \dots + \frac{1}{8} \left[-\frac{L_3 \delta_3 F_3 \nabla^2 \chi}{c_p \rho_3} \left(\frac{\rho_0}{\rho_3} \right)^\kappa - \frac{L_1 \delta_1 F_1 \nabla^2 \chi}{c_p \rho_1} \left(\frac{\rho_0}{\rho_1} \right)^\kappa \right]$$

$$\frac{\partial \sigma}{\partial t} = \dots + \frac{1}{8} \left[-\frac{L_3 \delta_3 F_3 \nabla^2 \chi}{c_p \rho_3} \left(\frac{\rho_0}{\rho_3} \right)^\kappa + \frac{L_1 \delta_1 F_1 \nabla^2 \chi}{c_p \rho_1} \left(\frac{\rho_0}{\rho_1} \right)^\kappa \right]$$

If $k_3 = \frac{L_3}{8 c_p \rho_3} \left(\frac{\rho_0}{\rho_3} \right)^\kappa$ and $k_1 = \frac{L_1}{8 c_p \rho_1} \left(\frac{\rho_0}{\rho_1} \right)^\kappa$, then in non-dimensional terms,

equation (2.8) and (2.9) become

$$\begin{aligned} \frac{\partial \theta}{\partial t} = 10^{-1} [-J(\psi, \theta) - J(\tau, \sigma)] + 10^{-3} [\nabla \cdot \sigma \nabla \chi] \\ - 10^{-3} [k_3 F_3 \delta_3 + k_1 F_1 \delta_1] \nabla^2 \chi \end{aligned} \quad (2.19)$$

$$\begin{aligned} \frac{\partial \sigma}{\partial t} = 10^{-1} [-J(\psi, \sigma) - J(\tau, \theta)] + 10^{-3} [\nabla \theta \cdot \nabla \chi] \\ - 10^{-3} [k_3 F_3 \delta_3 - k_1 F_1 \delta_1] \nabla^2 \chi \end{aligned} \quad (2.20)$$

and the equation (2.13) is modified so that

$$\nabla^2 \sigma_m \nabla^2 \chi - \frac{f^2}{b c_p} \nabla^2 \chi \quad (2.21)$$

$$\begin{aligned} = 10^2 [J(\psi, \theta) + J(\tau, \sigma)] - 10^2 \frac{f}{b c_p} [J(\psi, \nabla^2 \tau) \\ + J(\tau, \nabla^2 \psi)] \end{aligned}$$

where $\sigma_m = \sigma - (k_3 F_3 \delta_3 + k_1 F_1 \delta_1)$

Thus, when condensation occurs in either layer one or layer three, it implies the heating of the center layer, which is the average of the

other two. This influences the factor which multiplies the quantity $\nabla^2 \chi$ in equation (2.21). In this manner, whenever heating occurs, the magnitude of the term containing the Laplacian of χ is reduced.

The quantity L_i refers to latent heat released in layer i . It will be assumed that water vapor is condensing to liquid water in the lower layer and sublimating to ice in the upper layer. The heats of condensation and sublimation are 2520 erg/gm and 2862 erg/gm respectively. The corresponding values for k_1 and k_3 are 454.2 °K and 2118 °K .

Table 2-1 demonstrates the factor F at both lower and upper layers taking into account the temperature ranges associated with the two levels. F in this table is the value associated with a condensation threshold of $.8 q_s$.

In order to obtain an estimate as to the reduction $\sigma - \sigma_m$, it is noted that for $F_1 \approx .01$ and for $F_3 \approx .0002$, it is found that $k_1 F_1 \approx 4.5$ and $k_3 F_3 \approx .42$ compared with the variable σ , which is of the order of 10. Thus the influence of the release of latent heat at the upper layer is roughly a factor of 10 less than that of the lower layer.

2.4 Conditions on ω

The upper layer is considered to end at $p=0$. Since this is the top of the atmosphere, the quantity $\omega = \frac{dp}{dt}$ vanishes. At the bottom of the lower layer, at $p=1.0$, the vertical velocity can be considered

to be either zero or finite. A vanishing lower velocity implies that the bottom of the layer is at a solid surface, from which no air can rise. The finite case arises from the association with a boundary layer below the bottom level. One approximation which will be tried for the vertical velocity is the Ekman pumping relationship. In this case, the vertical velocity $w = \frac{dz}{dt}$ is proportional to the geostrophic vorticity at the top of the Ekman layer (Holton, 1972). The relationship is

$$\omega_E \approx -f g w_E = -f g J_g (K/2F)^{1/2} \quad (2.22)$$

where $K = 10^5 \text{ cm}^2 \text{ sec}^{-1}$, and $J_g = \nabla^2(\psi - \tau)$. Thus, in units of $10^{-3} \text{ mb sec}^{-1}$ the Ekman value for ω is on the order of $\omega_E \approx 3.0$.

The equations will determine a value for the vertical velocity of the middle level, ω_2 . The values for ω at levels 1 and 3 will be assumed to be averages of their values at the levels directly above and below the one in question, and so $\omega_1 = \frac{\omega_2 + \omega_3}{2}$ and $\omega_3 = \frac{\omega_2}{2}$.

2.5 Temperature and moisture conditions on the lower surface.

In this model, it is assumed that the bottom of the lower layer is an air-sea surface. Furthermore, the temperature of the sea surface is laterally prescribed and it is with this fixed sea surface-temper-

ature that the lower layer of air interacts. Since the period of time during which the model runs is only on the order of days and not of seasons, variations in sea surface temperatures are not an important part of the problem. The diurnal variation of sea surface temperatures is small and on the order of magnitude of $.2 \text{ } ^\circ\text{C day}^{-1}$ (Defant, 1961) and which furthermore decreases with latitude in the middle latitudes.

Evaporation from the sea surface will be assumed to be proportional to the difference between the saturation vapor pressure at the surface of the water and the vapor pressure of the moisture in the air over the water and proportional as well to the wind speed. The constant of proportionality is computed from Richards (1970). The relation is given in this manner by

$$\frac{dq_E}{dt} = 0.00055 (e_s - e) V \quad (2.23)$$

where e_s and e are in mb and $V^2 = \left[\frac{\partial}{\partial x} (\psi - \tau) \right]^2 + \left[\frac{\partial}{\partial y} (\psi - \tau) \right]^2$.

The vapor pressure of the water vapor in the air, e is calculated by assuming that the relative humidity of the lower layer is a fixed quantity at each grid point and by extrapolating the potential temperature down to the surface linearly by means of the two variables

θ and σ :

$$T_{\text{surf}} = \theta - 2\sigma \quad \text{in } ^\circ\text{K}$$

Thus $e = e_s (T_{\text{surf}}) \times \frac{q_1}{q_1 \text{ sat}}$

2.6 Lateral boundary conditions

The conditions placed upon the lateral boundaries are as follows. The domain is a rectangular set of $M \times N$ grid points which is periodic in the x -direction. The point (x_1, y_j) is considered to be the next point to the east of (x_M, y_j) for each y_j .

At the northern and southern boundaries there are walls. Since there is to be no flow permitted across these walls for either vertical level, the streamfunctions ψ and τ must be fixed and constant for the north and south set of grid points. Furthermore, there is an imposed temperature boundary condition on the two walls, the northern on the order of 5 degrees colder than the southern. In this manner, a somewhat realistic north-south temperature gradient is achieved.

Whenever any point outside the domain is needed for computation purposes, the value of a quantity at that point is extrapolated from its values at the two nearest points of the same x -component. This is necessary for evaluation of the Jacobian and Laplacian functions near the boundary. Thus for a field η ,

$$\eta(x_i, y_0) = 2\eta(x_i, y_1) - \eta(x_i, y_2)$$

and

$$\eta(x_i, y_{N+1}) = 2\eta(x_i, y_N) - \eta(x_i, y_{N-1}).$$

2.7 Numerical scheme

After the initial values for the model at a time step have been determined, the field for θ is computed from equation (2.12). Afterwards, the fields $\nabla^2\psi$ and $\nabla^2\tau$ are computed from the values of ψ and τ , using the five-point finite difference formula which approximates the Laplacian function

$$\nabla^2\psi_{i,j} = \psi_{i,j+1} + \psi_{i,j-1} + \psi_{i+1,j} + \psi_{i-1,j} - 4\psi_{i,j} \quad (2.24)$$

The next step in the procedure is to use equation (2.13) in the dry case and equation (2.21) in the moist case to evaluate the field $\nabla^2\chi$, but prior to this, the values of σ_m must be determined at each grid point in the moist model. In order to do this, it must be determined whether the conditions for the occurrence of condensation at each model grid point have been satisfied, that is, whether the appropriate fraction of saturation has been exceeded and whether there was ascending motion. When this has been determined, equation (2.21) can be written in the form

$$\mathcal{L}(\nabla^2\chi) = RHS$$

where \mathcal{L} is an operator which varies at each time step due to the changes in σ_m . $\mathcal{L}(\eta)$ is defined to be

$$\mathcal{L}(\eta) = -\frac{f^2}{bc_p}\eta + \nabla^2\left\{[\sigma - (k_3 F_3 \delta_3 + k_1 F_1 \delta_1)]\eta\right\}$$

Because σ_m varies horizontally, standard procedures of matrix inversion for evaluating a Helmholtz equation will not work exactly but they can be used in order to obtain a first approximation for an iterative scheme. A modified Gauss-Seidel iterative scheme is employed to find the solution to this equation (Hildebrand, 1956).

For the first iterative guess, in the Gauss-Seidel scheme, the average value of σ_m is computed from all the M x N grid points and is referred to as $\bar{\sigma}_m$. If σ_m is approximated by $\bar{\sigma}_m$, the equation then reduces to the form

$$\bar{\sigma}_m \nabla^2 (\nabla^2 \chi) - c_1 (\nabla^2 \chi) = g(x, y) \quad (2.25)$$

The Helmholtz equation

$$\nabla^2 \chi - c_1^* \chi = g^* \quad (2.26)$$

is solved where $c_1^* = c_1 / \bar{\sigma}_m$ and $g^* = g / \bar{\sigma}_m$, by means of the NCAR routine PWSCRT, which is an algorithm by R. Sweet (1974), and which uses a means of cyclic reduction.

This solution is used as a first iterative guess for the Gauss-Seidel iteration which is described below. If N, W, S, and E refer to the surrounding points, and 0 refers to the center point, the following equation must hold for each grid point

$$\sigma_N \chi_N + \sigma_W \chi_W + \sigma_S \chi_S + \sigma_E \chi_E - (4\sigma_0 + c_1) \chi_0 = g_0$$

where $\mathcal{D} = \nabla^2 \chi$. The set of M x N equations can be conveniently placed in the following form for each equation

$$\mathcal{D}_o = \frac{1}{4\sigma_o r c_1} [\sigma_N \mathcal{D}'_N + \sigma_W \mathcal{D}'_W + \sigma_S \mathcal{D}'_S + \mathcal{D}'_E \mathcal{D}'_E - g_o]$$

In this manner a value for \mathcal{D}' at the central point is determined from its current values at the surrounding set of points and then the value for \mathcal{D}_o is modified as soon as it is calculated. This type of method is a sequential relaxation scheme. The order of choosing the central points is preselected in this case to be that of "reading order" from upper left to lower right if the grid points were placed in a physical array. The N+1 st approximation is obtained by using the values of the \mathcal{D}' 's on the right hand side in either the N th or N+1 st approximation depending upon whether or not that grid point has been "relaxed" yet. The process continues until the right and left hand side of equation (2.27) are within a preselected ϵ of each other for each \mathcal{D}_o . The question of determining a suitable value for ϵ which is small enough to be used in order to look at error growths is treated in a later chapter.

When the \mathcal{D}' values have been determined, it is then necessary to find χ up to an additive constant and this is obtained from inversion of the $\nabla^2 \chi$ by means of PWSCRT, as discussed above. Then the values for ω_1 and ω_3 at each grid point are obtained from the relation $\omega_1 \approx \omega_3 = \frac{1}{4} \nabla^2 \chi$.

The next step in the running of the model is the integration of equations (2.10), (2.16), (2.17), (2.19), and (2.20). This is

accomplished by the use of the method of N-cycles as proposed by Lorenz (1971). This method is of higher order than the standard uncentered difference integration scheme.

A 4-cycle is used in this model. The method is a second-order integration scheme for non-linear terms. It breaks up a large step into four smaller time steps and repeats a procedure four times in order to be of higher order.

In the case $N = 4$, where $\delta t = \frac{\Delta t}{4}$, an algorithm derived by Lorenz is used in order to solve the set of linear equations

$$\frac{dx_i}{dt} = F_i(x) \quad i=1, \dots, M$$

where $F_i(x)$ is a set of functions of x which can be computed.

After the values for $\nabla^2 \psi$ and $\nabla^2 \tau$ are determined, the quantities ψ and τ are obtained by means of matrix inversion using PWSCRT, as described above. After this takes place, the other variables must be found again for the next time step, and the process continues.

All Jacobians are evaluated by the method proposed by Arakawa (1966). This scheme involves values of the two fields at the central point and eight surrounding points. Since the Jacobian is a formulation of the advection term in the equations, it is desirable to use this form of the Jacobian which maintains the integral constraints of conservation of mean square vorticity and mean kinetic energy.

Chapter 3. Results of error growth in representative model runs.

Runs of the model described in Chapter 2 were made on grids of various sizes on a domain which is 3200 km x 3200 km. Initial test runs of the model on a small grid (8 x 9 points) with grid point spacing of 400 km were made with satisfactory results; however, this preliminary model was used only as a basis for the development of larger grid point models.

Two finer grids of 16 x 17 and 32 x 33 grid points and spacings of 200 km and 100 km respectively were employed for further study and they are referred to as the L and G grids respectively.

In order to determine the magnitude of difference between the two simultaneously running models in phase space, a measure of error was needed. This measure is called the "error kinetic energy" which is defined in the following form

$$\vec{V}_{e_1} \cdot \vec{V}_{e_1} + \vec{V}_{e_3} \cdot \vec{V}_{e_3}$$

The vectors \vec{V} are wind error vectors, with the subscripts 1 and 3 referring to the 750 mb and 250 mb levels respectively. The error winds are the difference winds between those of model A and those of model B

$$\vec{V}_e = \vec{V}_a - \vec{V}_b \quad (3.1)$$

Since $\vec{V}_1 = k \times \nabla \psi_1$ and $\vec{V}_3 = k \times \nabla \psi_3$ and also $\psi = \frac{1}{2} (\psi_3 + \psi_1)$ and $\tau = \frac{1}{2} (\psi_3 - \psi_1)$, one can obtain the following expression for error kinetic energy (to be abbreviated EKE henceforth) for each grid point

$$EKE = \nabla(\psi_a - \psi_b) \cdot \nabla(\psi_a - \psi_b) + \nabla(\tau_a - \tau_b) \cdot \nabla(\tau_a - \tau_b) \quad (3.2)$$

The individual grid point values of the error kinetic energies are summed together to obtain a total measure of error kinetic energy.

The model is a dry model of 16 x 17 grid points where the grid point spacing in both directions is 200 km. Thus, the total area covered is $10.24 \times 10^6 \text{ km}^2$, or an area of the magnitude of the size of the United States.

Originally, initial data were placed to simulate one large scale wave pattern in the ψ field and a θ field was chosen to be warmer in the southern region than in the northern region by 5°C , and τ was taken to be a constant (10°C). The model was permitted to be run to a time equivalent of $1000 \times 10^3 \text{ sec}$, after which its final conditions were taken to be used as a new set of initial conditions.

The initial state is pictured in Figures 3-1 to 3-4, which represent the four quantities ψ , θ , σ , and ω . ψ is measured in units of $1 \text{ km}^2 \text{ sec}^{-1}$, θ and σ are in units of 1°K , and the value for ω , which is obtained from the quasi-geostrophic set of equations, is in units of $10^{-3} \text{ mb sec}^{-1}$. It can be seen that the ψ field still retains the wave-like nature which moves across the domain. The characteristic velocity of wave motions, which is approximately 10 m sec^{-1} , can be noted by observing the position of the ridges which move across the domain in approximately $300 \times 10^3 \text{ sec}$.

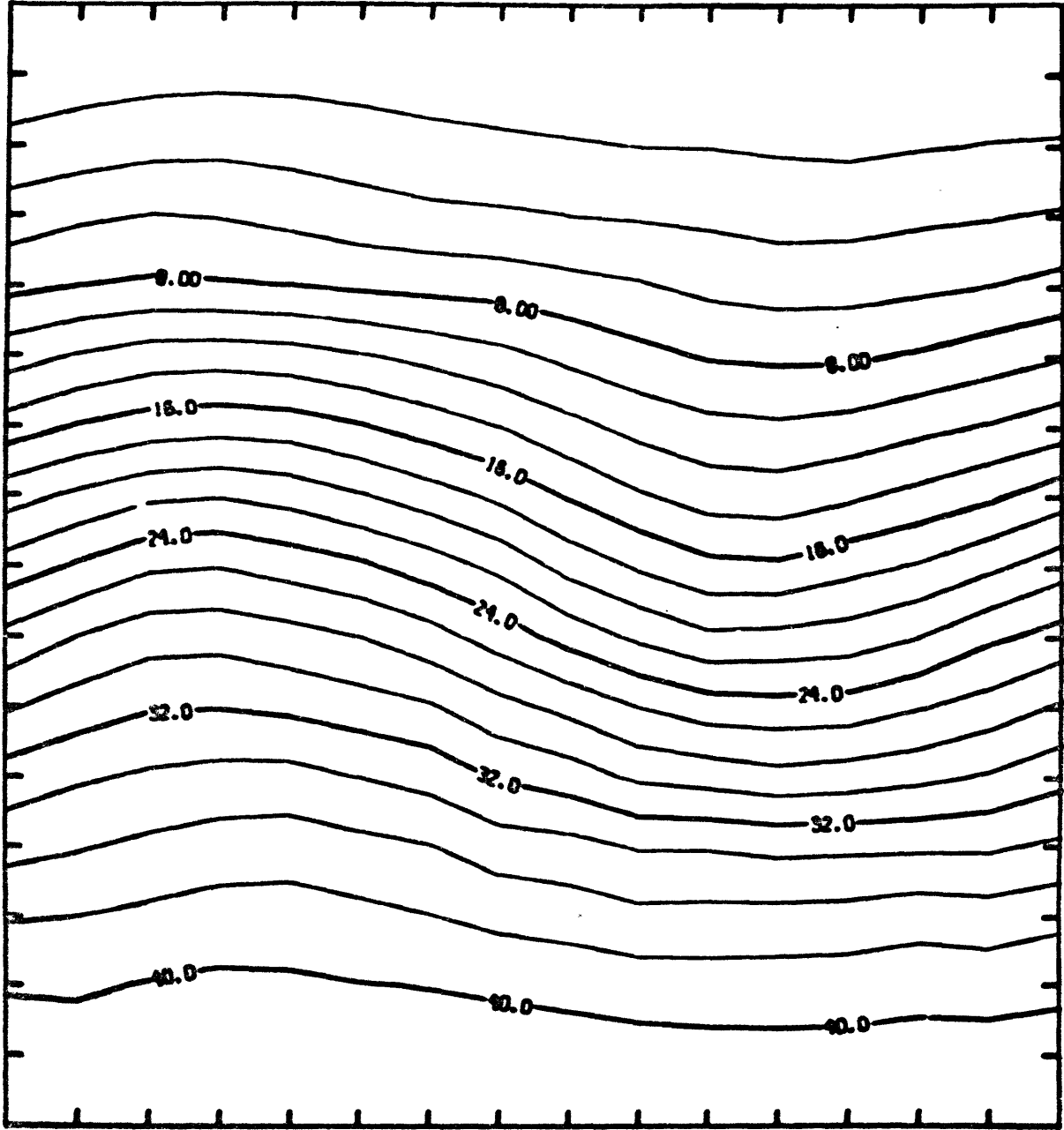


Figure 3-1. Initial state of ψ field. Values are in $\text{km}^2 \text{sec}^{-1}$.

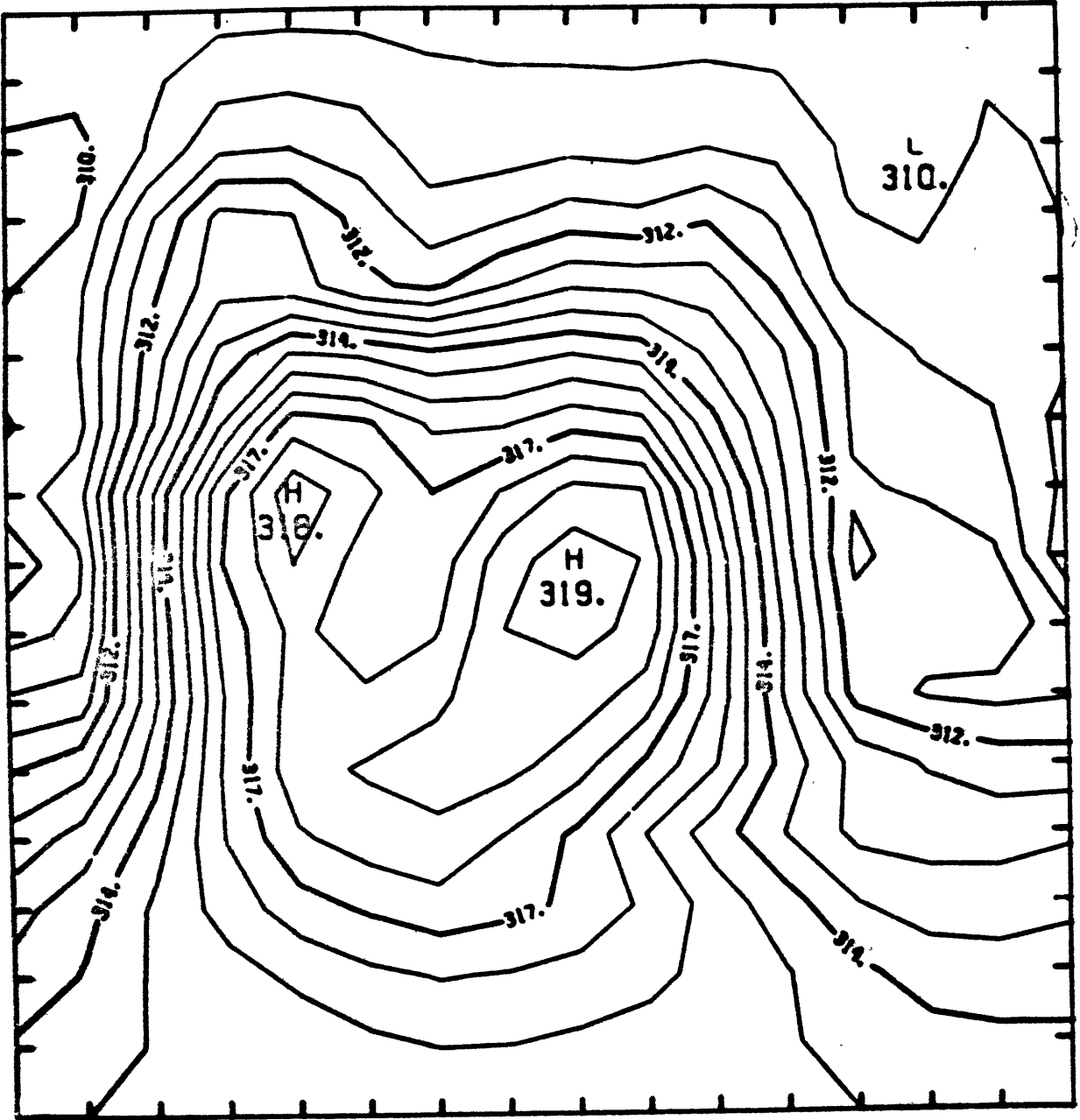


Figure 3-2. Initial state of θ field. Values are in $^{\circ}\text{K}$.

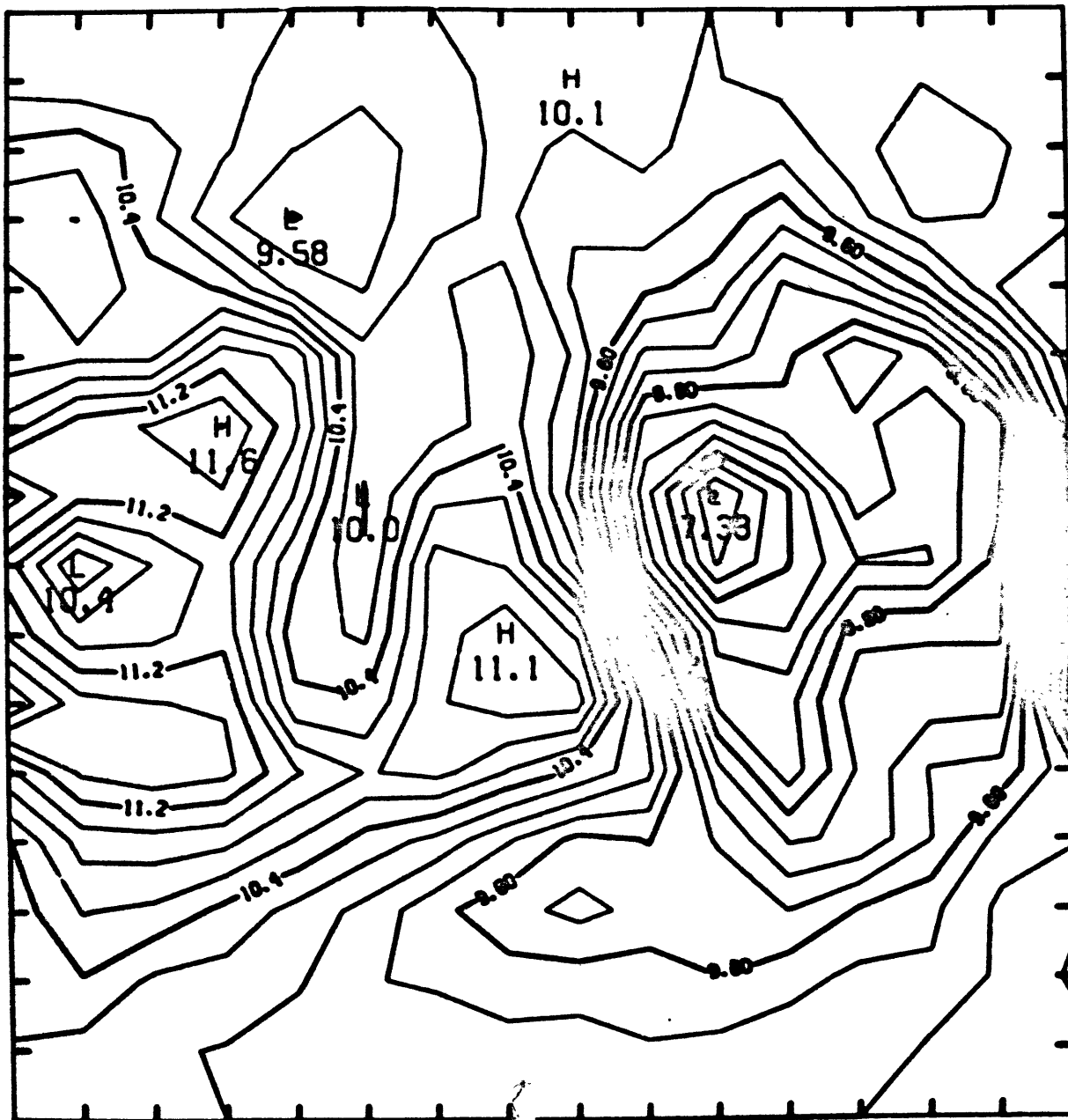


Figure 3-3. Initial state of σ field. Values are in $^{\circ}\text{K}$.

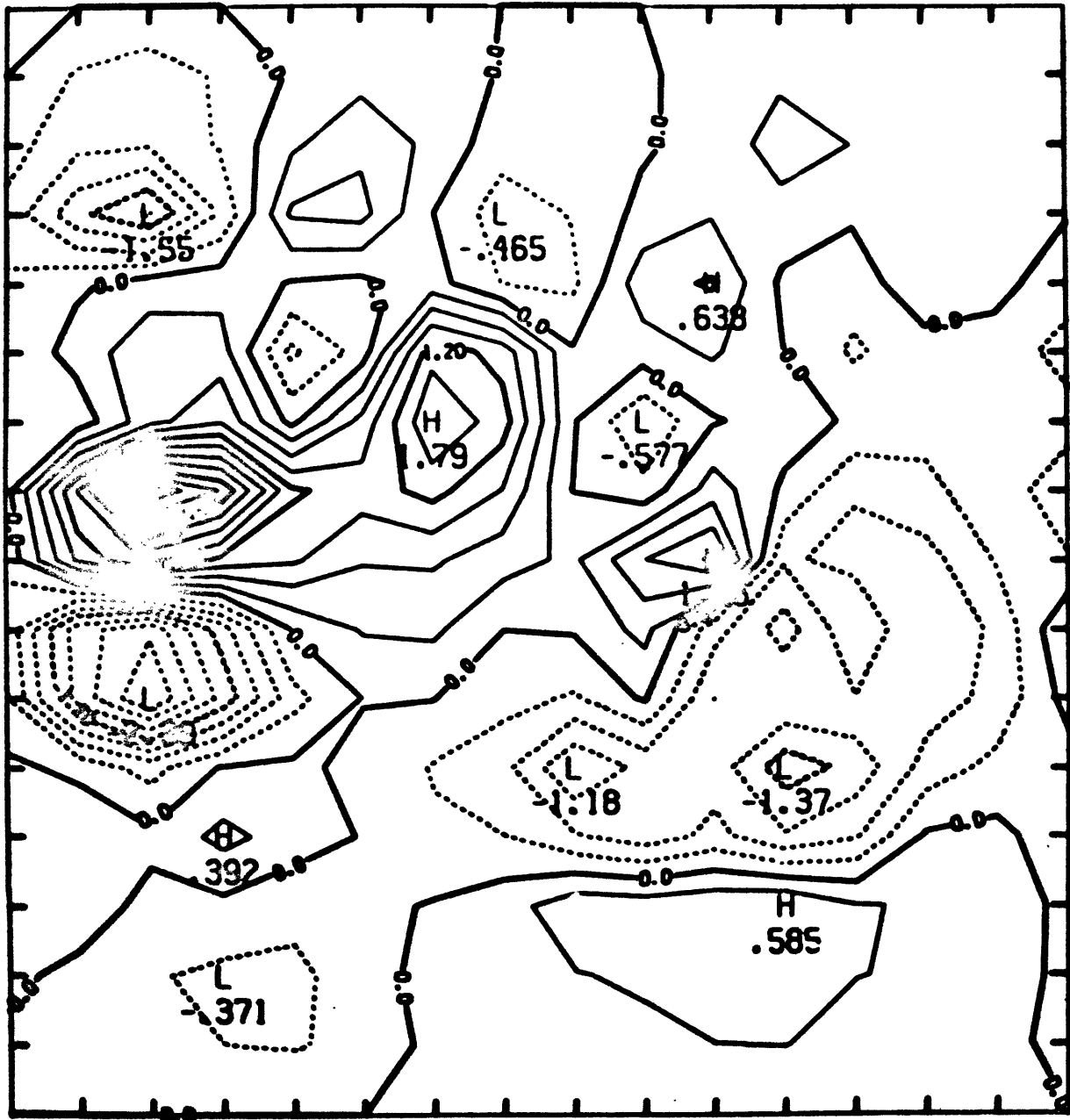


Figure 3-4. Initial state of ω field. Values are in $10^{-3} \text{ mb sec}^{-1}$.

The fields for θ , σ , and ω are all rather complex at the new initial state because they evolved as a result of the set of equations in 1000×10^3 sec. Because of the constant Coriolis parameter in the model, the ζ field is linearly related to the θ field.

3.1 Determination of a relaxation constant for examination of error kinetic energy growth.

In the Gauss-Seidel iteration scheme which is employed in order to solve the χ equation (Equation 2.21) the values of the right and left hand side of the equation must agree to within a certain quantity ϵ . This maximum allowable ϵ must be determined for stability of the model and so that it is sufficient for the determination of error kinetic energies. With this in mind, several experiments were performed by running the 16 x 17 model with various values for ϵ , and the resultant EKE values were noted. The EKE values which are generated by the model corresponding to $\epsilon = .0002$, $.0001$, $.00005$, and $.000025$ are in Table 3-1 for time steps between 0 and 600×10^3 sec.

If an additionally smaller value of ϵ causes no change in the value of EKE for a desired accuracy, it is reasonable to assume that this ϵ is sufficiently small enough to be used as a sensitivity constant in this study. It can be seen from Table 3-1 for $\epsilon = .0002$ to $\epsilon = .000025$, the EKE values are the same to 3 decimal places until $t = 200 \times 10^3$ sec, that they are the same to 2 decimal places until $t = 550$, and that until $t = 600 \times 10^3$ sec, they agree to one decimal place. Thus $\epsilon = .0002$ appears to be small enough for a sensitivity constant so that there is agreement of both sides of the χ -equation for the purpose of measuring the resultant EKE value to within .1

In addition, the computer time in seconds required to run the

model to $t = 600 \times 10^3$ sec real time on NCAR's Control Data Corporation 7600 is shown for the various values of ϵ . It can be seen that the difference between the smallest and largest ϵ is a factor of 7% greater. This additional fraction might not seem like significantly greater computer time for an order of magnitude improvement, and its smallness can be explained for the following reasons: (a) the solution to this one equation is only a small part of the total computer time required, (b) the first guess of the iteration scheme is relatively close to the solution, and (c) the number of iterations varies with the logarithm of the desired accuracy.

In order to look more closely at the convergence of this Gauss-Seidel solution, succeeding approximations of the values for in the iteration scheme can be observed. For a particular run of the 16×17 grid point model, at a particular time step ($t = 300 \times 10^3$ sec), the sequential guesses which are derived from the first 50 iterations are displayed in Table 3-2 for five representative points of the domain. They are calculated to six decimal places. First, it can be seen that the initial guess (iteration 0), which forms the solution to equation (2.25) is close to the solution to which the iterations converge, and agrees with it generally to one decimal place. Furthermore, after only 10 iterations, the guess agrees with the final solution with an accuracy of three decimal places.

An extension of the Gauss-Seidel method which is called "successive overrelaxation" can be used in order to speed the conver-

Table 3-2. (Next page) Successive approximations of $\gamma = \nabla^2 \chi$ at five representative grid points in a Gauss-Seidel iteration scheme.

GRID POINTS

<u>ITE-</u> <u>RATION</u>	(1,3)	(5,5)	(2,6)	(7,4)	(4,5)
0	-5.648512	-.289005	-.151360	4.840213	-4.135060
1	-5.561310	-.297183	-.143804	4.910203	-4.155047
2	-5.559991	-.296860	-.165521	4.937216	-4.167580
3	-5.554533	-.302332	-.164012	4.944949	-4.170573
4	-5.566178	-.302506	-.156500	4.950691	-4.173897
5	-5.566791	-.301857	-.155162	4.954068	-4.175550
6	-5.567169	-.301482	-.154831	4.956013	-4.176361
7	-5.567412	-.301066	-.154906	4.957398	-4.176855
8	-5.567554	-.300648	-.155104	4.958250	-4.177091
9	-5.567626	-.300268	-.155299	4.958827	-4.177157
10	-5.567652	-.299933	-.155457	4.959228	-4.177123
11	-5.567647	-.299646	-.155565	4.959515	-4.177036
12	-5.567624	-.299402	-.155625	4.959727	-4.176924
13	-5.567591	-.299198	-.155645	4.959888	-4.176805
14	-5.567552	-.299028	-.155636	4.960015	-4.176689
15	-5.567511	-.298885	-.155607	4.960117	-4.176581
16	-5.567471	-.298766	-.155565	4.960201	-4.176483
17	-5.567431	-.298666	-.155518	4.960272	-4.176395
18	-5.567394	-.298581	-.155468	4.960333	-4.176317
19	-5.567360	-.298509	-.155418	4.960386	-4.176249
20	-5.567328	-.298447	-.155371	4.960432	-4.176189
21	-5.567299	-.298393	-.155326	4.960473	-4.176137
22	-5.569272	-.298347	-.155285	4.960509	-4.176091
23	-5.567248	-.298306	-.155248	4.960541	-4.176050
24	-5.567227	-.298271	-.155214	4.960569	-4.176015
25	-5.567208	-.298239	-.155184	4.960595	-4.175983
26	-5.567191	-.298212	-.155157	4.960617	-4.175956
27	-5.567176	-.298188	-.155133	4.960637	-4.175931
28	-5.567162	-.298166	-.155111	4.960655	-4.175910
29	-5.567150	-.298147	-.155092	4.960671	-4.175891
30	-5.567139	-.298130	-.155075	4.960685	-4.175874
31	-5.567130	-.298115	-.155060	4.960698	-4.175859
32	-5.567121	-.298102	-.155046	4.960709	-4.175845
33	-5.567114	-.298090	-.155034	4.960719	-4.175833
34	-5.567107	-.298079	-.155024	4.960728	-4.175823
35	-5.567101	-.298070	-.155014	4.960735	-4.175814
36	-5.567096	-.298062	-.155006	4.960742	-4.175805
37	-5.567091	-.298054	-.154998	4.960749	-4.175798
38	-5.567087	-.298048	-.154992	4.960754	-4.175791
39	-5.567083	-.298042	-.154986	4.960759	-4.175786
40	-5.567080	-.298037	-.154980	4.960763	-4.175780
41	-5.567077	-.298032	-.154976	4.960767	-4.175776
42	-5.567074	-.298028	-.154972	4.960771	-4.175772
43	-5.567072	-.298024	-.154968	4.960774	-4.175768
44	-5.567070	-.298021	-.154965	4.960777	-4.175765
45	-5.567068	-.298018	-.154962	4.960779	-4.175762
46	-5.567066	-.298016	-.154959	4.960781	-4.175759
47	-5.567065	-.298014	-.154957	4.960783	-4.175757
48	-5.567063	-.298012	-.154955	4.960785	-4.175755
49	-5.567062	-.298010	-.154953	4.960786	-4.175753

gence of the scheme (see Walsh, 1967). The n+1 st and n th guesses are γ^{n+1} and γ^n respectively, and their difference, which is determined from equation (2.21) is termed the residual R^n :

$$\gamma^{n+1} = \gamma^n + R^n$$

where

$$R^n = \frac{1}{4\sigma_0 + c_1} [\sigma_N \gamma_N^n + \sigma_W \gamma_W^n + \sigma_S \gamma_S^n + \sigma_E \gamma_E^n - g_0] - \gamma_0^n \quad (3.3)$$

A more rapid iterative scheme involves an additional multiplicative factor of the residual, usually between 1 and 2

$$\gamma^{n+1} = \gamma^n + \omega R^n \quad (3.4)$$

In this manner the n+1 st guess would be more in the direction of the solution. Further study would warrant the use of such an improved solution.

3.2 Error growth rates from initial random errors.

A set of normal random numbers which are multiplied by an amplitude factor of .05 was added to each grid point value of the field in model A in order to determine the initial conditions in model B, thereby creating an initial quantity of error kinetic energy (EKE). The set of normal random numbers was generated by the computer routine known as GGNOF which is resident in the IMSL (International Mathematical and Statistical Libraries).

The results of the representative runs using this particular set of random numbers as initial errors in both the coarse (16 x 17) and fine (32 x 33) models and in the dry and moist cases is the subject of this chapter. It is instrumental to observe the type of behavior of error growth in particular cases as well as in statistics of a set of cases, as will be discussed in a later chapter.

3.3 Error growth in the coarse mesh model

In this case of 16 x 17 grid points, the initial EKE value was 0.1167 units. During the course of the running of the models, the value for EKE was observed. By $t = 300 \times 10^3$ sec, the EKE grew to 1.2596 units, which is a growth factor of 10.8, and by $t = 600 \times 10^3$ sec, the EKE amplified to 38.6227 units, or a factor of 331.0 over the initial value.

In the moist case, with equations taken from section 2.3, the identical set of initial conditions were used except for the addition of a lower-level (750 mb) moisture field. A typical moisture field is represented in Figure 3-5. The same initial perturbation of the ψ field as was placed in the B model in the dry case was placed in the B model in the moist case.

For the moist case, it is important to specify other conditions in addition to those of the dry case, and an important one is the underlying sea-surface temperature. It was found that higher values of sea-surface temperature led to greater magnitudes of EKE growth. For each of the moist values, though, the initial EKE was the same as that in the dry case (0.1167 units).

For the underlying sea-surface temperature for the whole domain at $T = 292 \text{ }^\circ\text{K}$, for example, the value for EKE grew to 1.4173 units at $t = 300 \times 10^3$ sec, and 40.3344 units at $t = 600 \times 10^3$ sec, or factors of 12.1 and 345.6 respectively over the

initial state. At a higher sea surface temperature, $T = 297$ °K, the quantities were 1.4916 and 47.5675 or factors of 12.8 and 407.6 at $t = 300 \times 10^3$ sec and 600×10^3 sec, respectively.

The growth of EKE for the above dry and moist models is plotted on a logarithmic plot in Figure 3-6. The solid line represents error levels in the dry case, the broken line in the moist $T = 297$ case, and the circles are EKE values of the moist $T = 292$ case. It can be seen that the growth rates are very close to exponential after $t = 100 \times 10^3$ sec, or about one day, and appear almost as straight lines in this logarithmic plot. After about $t = 200 \times 10^3$ sec, the dry and moist values for EKE begin to diverge. The fractional difference of the moist (297K) EKE value over that of the dry KE value is plotted in Figure 3-7. It can be seen that at the outset, the fractional difference is negligible but grows to 19% by $t = 300 \times 10^3$ sec, and by 550×10^3 sec, it is up to 27%, although it drops back down to 23% by $t = 600 \times 10^3$ sec.

Very long integrations of this model (to $t = 1800 \times 10^3$ sec) were carried out in both dry and moist(292) cases in order to observe the long term behavior of the error growth rate, and the results are represented in Figure 3-8. From this figure, it can be seen that the EKE value exhibits a leveling-off behavior at approximately $t = 1400 \times 10^3$ sec in the dry case, and at $t = 1200 \times 10^3$ sec in the moist case. Thus the dry model reaches its maximum level of error growth at 16.3 days and the moist model at 13.8 days.

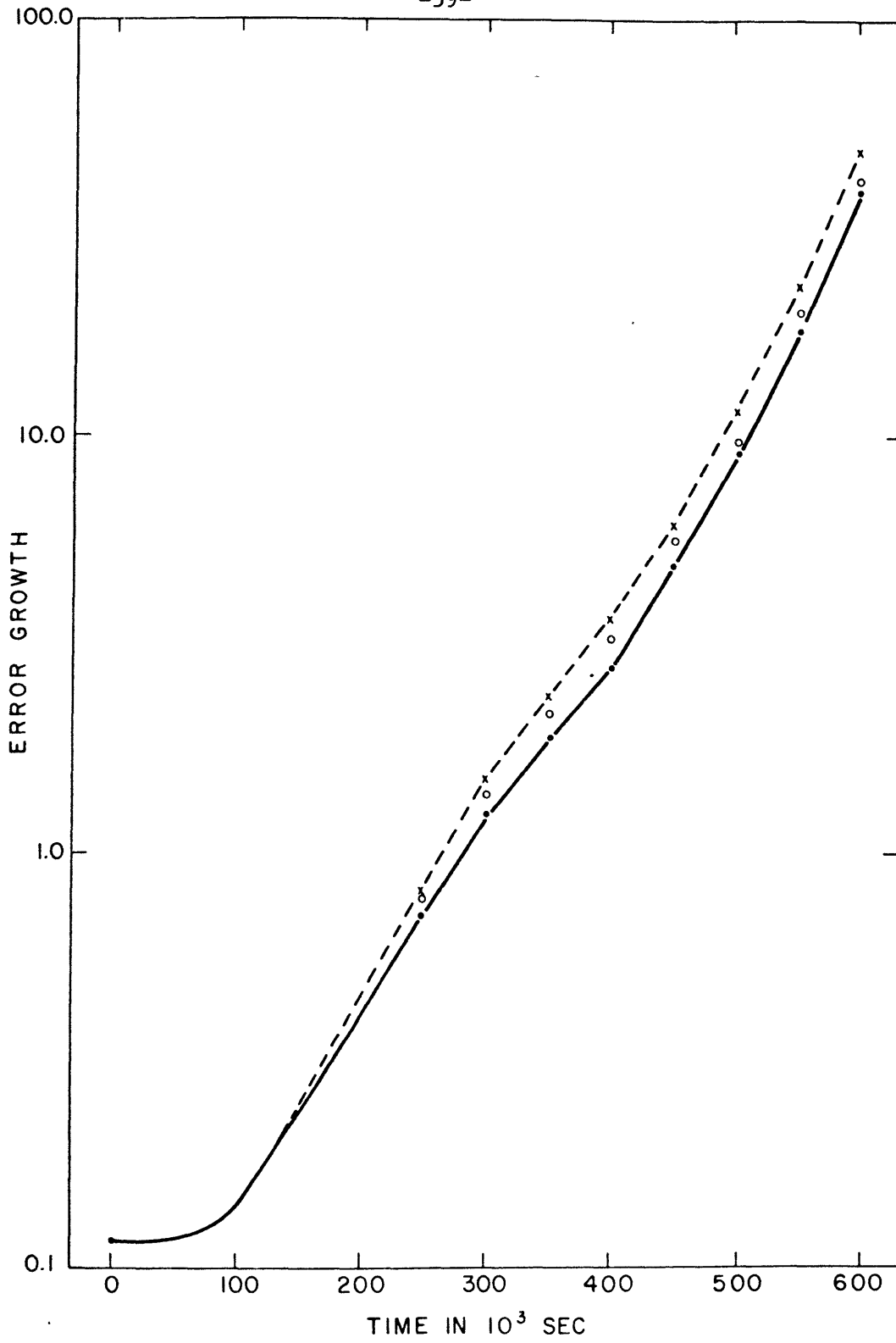


Figure 3-6. Growth rates of error kinetic energy in the 16 x 17 grid for dry case (solid), moist T=297 case (broken) and T=292 (circles).

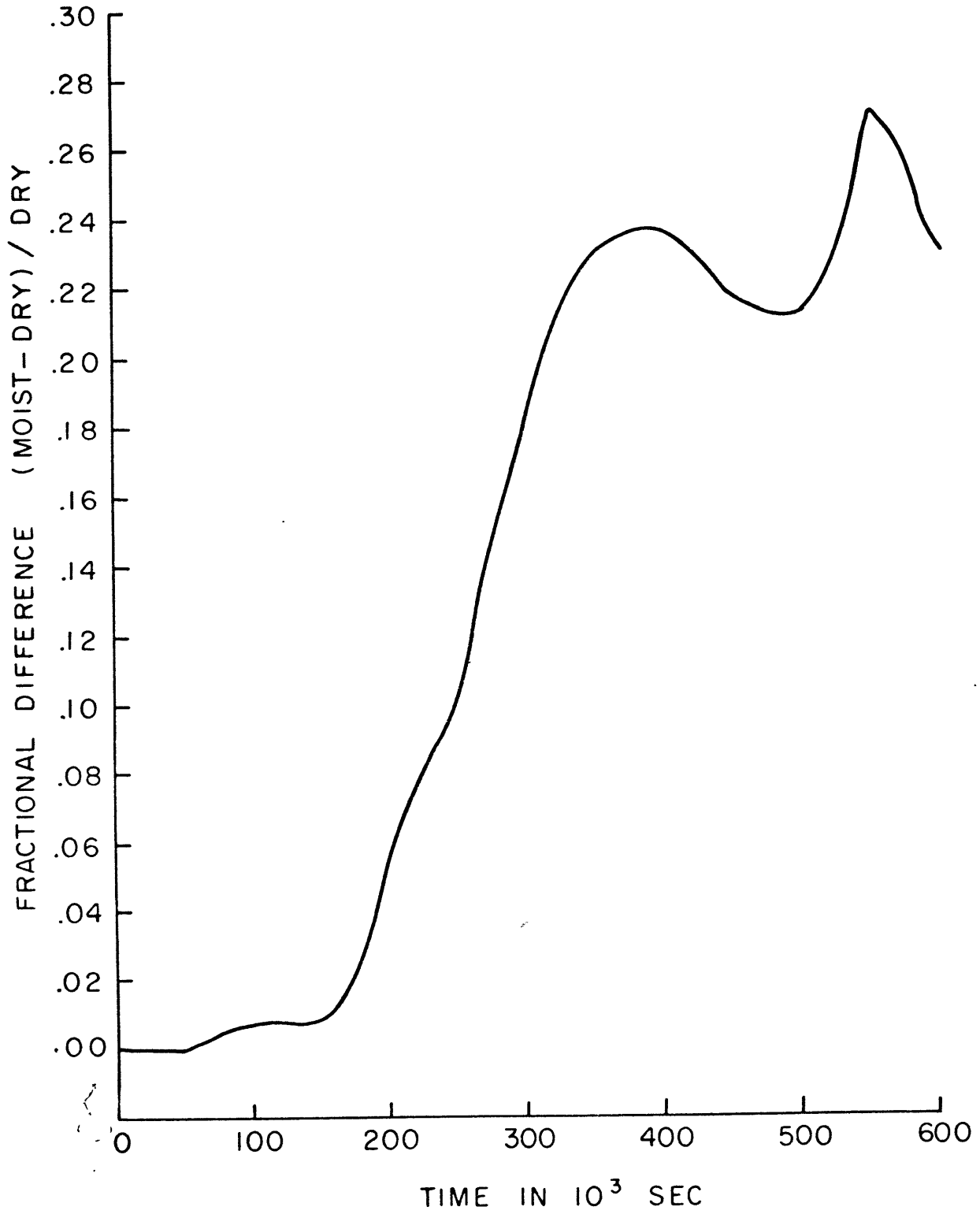


Figure 3-7. Fractional difference in error kinetic energy of the moist case over the dry case (16 x 17 grid).

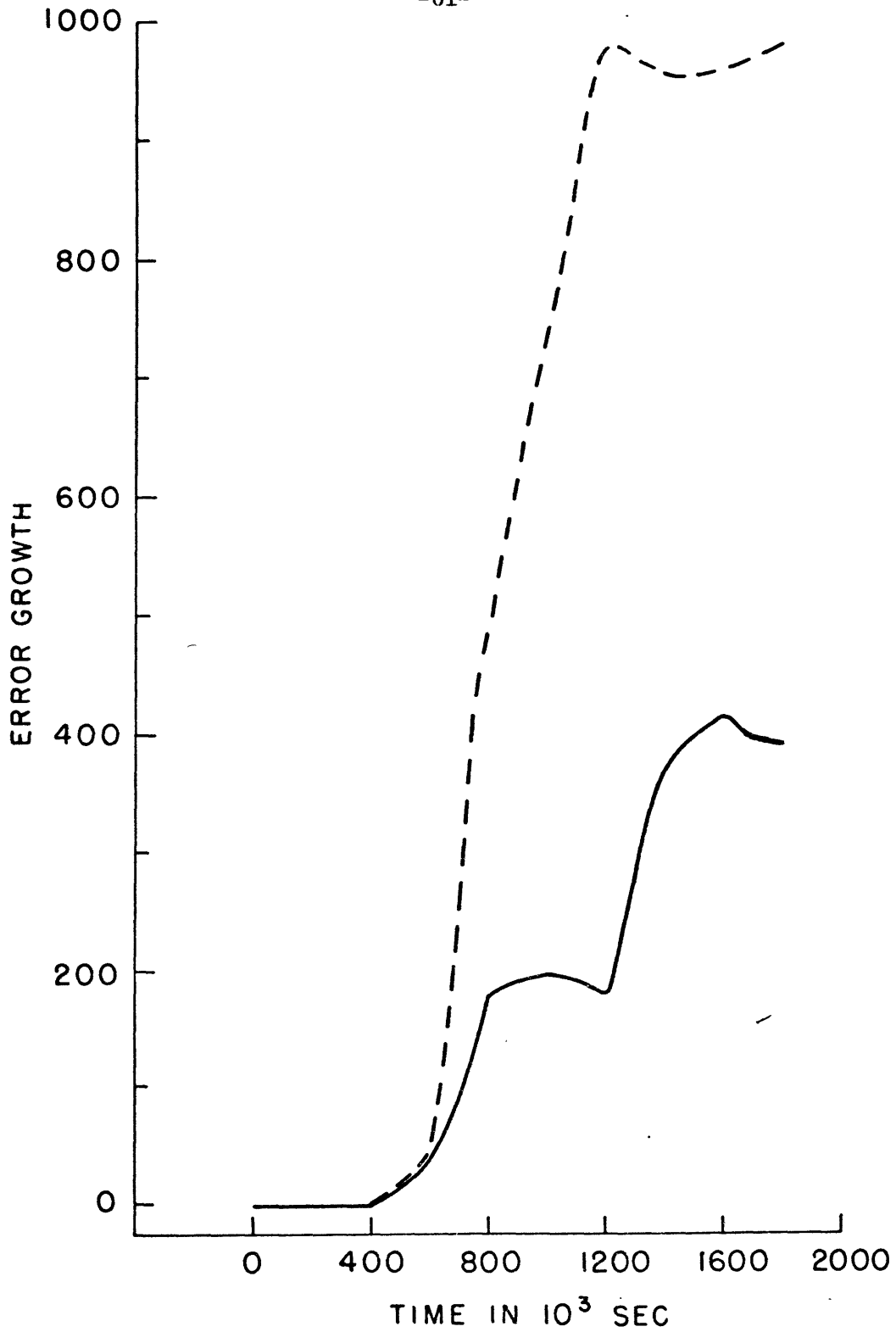


Figure 3-8. Long term levels of error kinetic energy in the dry case (solid line) and moist case (broken line).

It can be assumed that the level-off point of EKE growth is related to the time limit of predictability, because statistically, the errors reach 100% of their ultimate value at the level-off (quasi-stationary) point. The values obtained as a result of the models described here are in general agreement with those estimates of atmospheric error growth rate, which find that there is a two-week limit of predictability. Lorenz (1969b) found that the predictability of the largest (and most predictable for the longest period of time) scale he considered in his experiments was limited to 16.8 days when a very small error was placed initially in the smallest scale of motion in the dry model. This is close to the estimate of 16.3 days in the dry model considered here.

Furthermore, the time at which the two models reach a stationary level of error energy growth differs by 2.5 days, implying that this is the difference between the time limits of predictability of the dry and moist cases.

3.4 Error growth in the fine mesh model.

In numerical prediction of fluid motions, one can make the grid points close together in order to create a finer grid. There have been studies investigating the optimum grid length (Knighting, 1959), and the grid lengths in both the quasi-geostrophic set of equations (Howcraft, 1966) and the primitive equation models of general circulation models (Wellck, et. at., 1971 for the NCAR model and Manabe, et. al., 1970 and Miyakoda et. al., 1971 for the GFDL.)

Some results of increased resolution are as follows: The NCAR model finds a 10° latitude and longitude mesh (1100 km at the equator) too coarse. A 5° mesh was acceptable but did not treat transports of momentum, heat and water vapor accurately, and a $2 \frac{1}{2}^{\circ}$ mesh (equivalent to 270 km at the equator and 200 km in middle latitudes) more accurately treated these transports.

Similarly in the GFDL model, a finer grid resolution (500 to 250 km grid point model improved the features, especially being more successful in the simulation of the evolution of fronts.

With the above in mind, a finer mesh model was developed in this study. This finer mesh model (which is referred to in this work as (G)), covers the same domain as the L model, however, with 32×33 grid points spaced on the domain at 100 km apart, instead of 200 km apart as in the 16×17 grid. The number of grid points is thus increased by close to a factor of 4.

Phillips (1973) states the criterion necessary for convergence

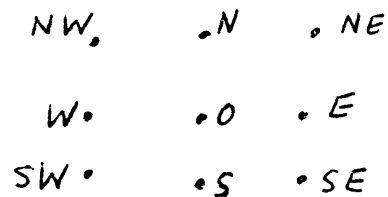
of a numerical equation

$$\frac{U \Delta t}{\Delta x} = \sigma < 1 \quad (3.5)$$

where U is a representative velocity and Δt and Δx are the time and space differences. Since the G grid halves the grid spacings, in order to maintain the same value for σ , a halving of the time step is required as well. Thus the amount of computation for the time integration increases by a factor of 8 in the finer G model.

Additionally, a finer mesh increases the number of successive iterations required for convergence of the Gauss-Seidel scheme which is used to solve the Helmholtz equation (2.26). Young (1954) has analyzed the effect of decreased mesh size and has determined that if the grid size is reduced by a factor of h , then the number of iterations is increased on the average by a factor of h^2 , and that the time required for computations is increased by a factor of h^4 because the number of grid points is increased as well by h^2 .

The initial conditions for the finer grid are identical to those of the coarser grid with the exception of interpolations between the grid points of each of the fields involved.



If NW, NE, SW, and SE are the points in the 16 x 17 model, then the value of a field at the other points are taken as

$$\psi_s = \frac{1}{2} (\psi_{sw} + \psi_{se}) \quad , \quad \psi_n = \frac{1}{2} (\psi_{nw} + \psi_{ne})$$

$$\psi_w = \frac{1}{2} (\psi_{nw} + \psi_{sw}) \quad , \quad \psi_e = \frac{1}{2} (\psi_{ne} + \psi_{se})$$

$$\psi_o = \frac{1}{4} (\psi_{nw} + \psi_{ne} + \psi_{sw} + \psi_{se})$$

Using the finer G model, the total EKE growth can be examined. If an initial normal random error with amplitude .05 is applied to the ψ field of model A and used as initial ψ in model B, then the initial value for the EKE in this case is 2.2334 units. The growth of EKE in both the dry and moist model cases is plotted in Figure 3-9 on a logarithmic scale. Since these curves are also approximately straight lines, it can be seen that the error growth is close to exponential after $t = 100 \times 10^3$ sec. Within 300×10^3 sec, the value for EKE of the dry model reached 19.01 units or a growth factor of 8.51 and that of the moist model (sea surface temperature 292°K) reached 20.9120 units or a factor of 9.36. By $t = 500 \times 10^3$ sec, the EKE of the dry and moist cases had grown by factors of 52.8 and 36.4 respectively.

If one compares the finer and coarser grids, one can determine a similar relationship in the dry and moist cases. Table 3-3 shows the growth of EKE over its initial value for both the G and L grids. One can see for example that the EKE growth in the 16×17 coarse mesh model does not exceed that in the fine mesh model until $t = 250 \times 10^3$, in both the dry and moist cases, and by $t = 500 \times 10^3$ sec, the EKE growth of the coarse mesh is a factor of two greater

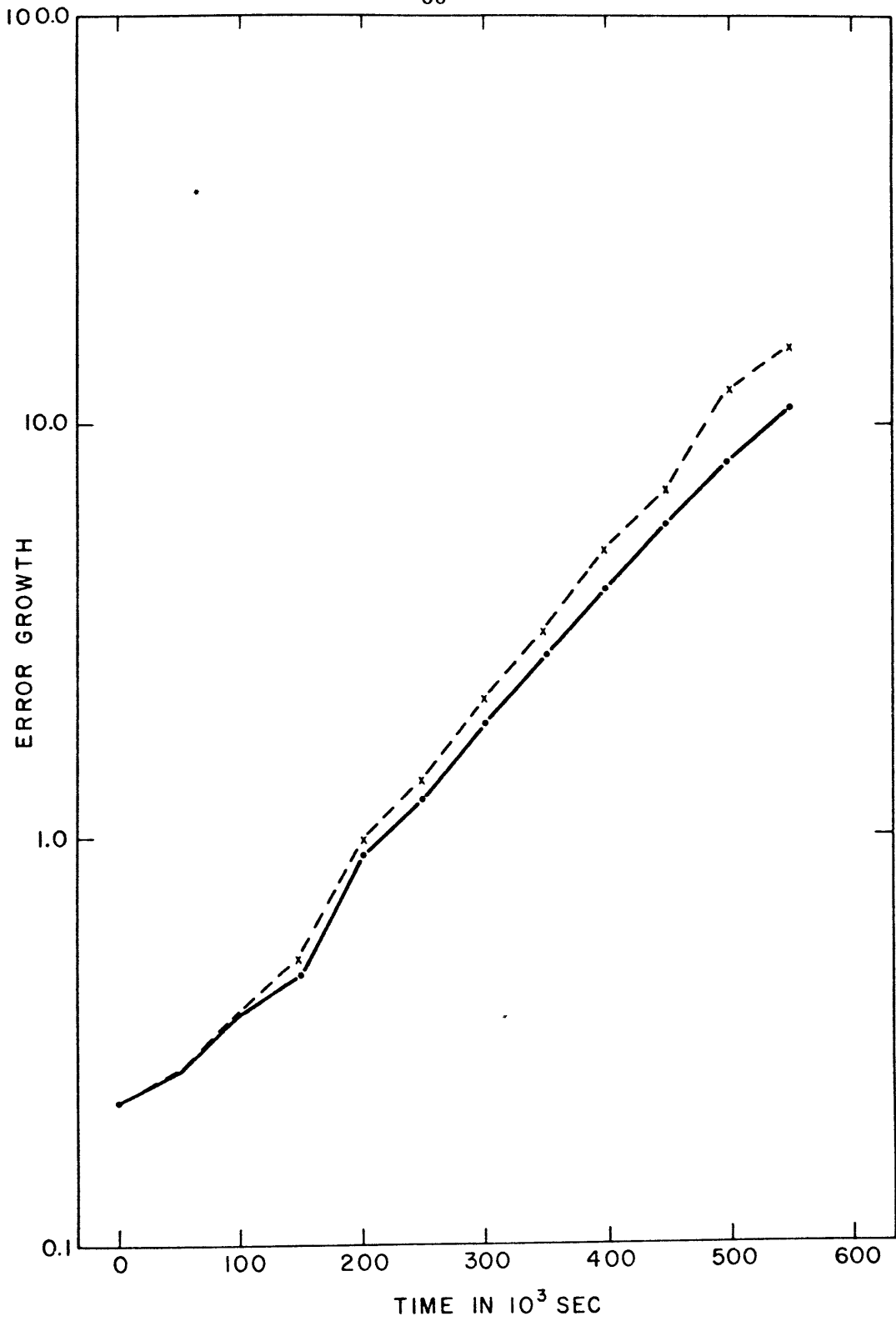


Figure 3-9. Growth rates of error kinetic energy in the fine (32 x 33) grid for the dry case (solid line) and the moist case (broken line).

Table 3-3. Growth of error kinetic energy over its initial value.

<u>time (10³ sec)</u>	<u>32 x 33 dry</u>	<u>16 x 17 dry</u>	<u>32 x 33 moist</u>	<u>16 x 17 moist</u>
0	1.000	1.000	1.000	1.000
50	1.205	1.118	1.206	1.118
100	1.660	1.225	1.666	1.234
150	2.601	1.996	2.671	1.983
200	4.114	3.619	4.451	3.820
250	5.519	6.252	6.005	6.902
300	8.513	10.793	9.364	12.781
350	12.747	16.297	13.410	20.059
400	18.513	23.553	22.742	29.415
450	25.761	42.264	35.878	51.408
500	36.371	78.812	52.819	100.30

than in the fine mesh case for both the dry and moist models.

If h is the distance between grid points and if $E_d(h,t)$ and $E_m(h,t)$ are the dry and moist factors of EKE growth from an initial state, the values from the table suggest that the same relationship holds for both the moist and dry cases

$$\frac{E_d(h_{100}, t)}{E_d(h_{200}, t)} \approx \frac{E_m(h_{100}, t)}{E_m(h_{200}, t)} = \bar{E}(t) \quad (3.6)$$

and the function $\bar{E}(t)$ is represented in Figure 3-10.

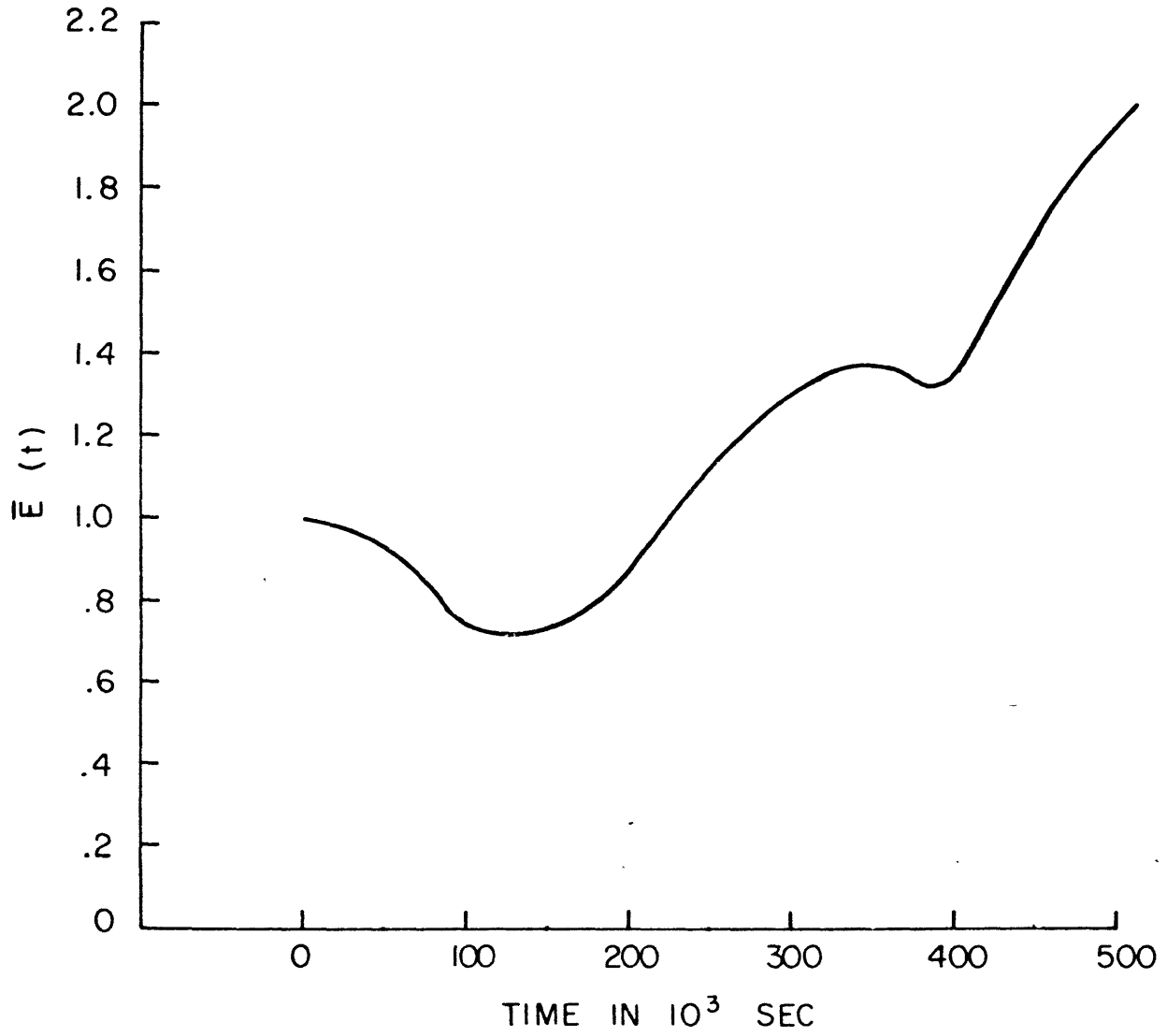


Figure 3-10. The average function $E(t)$, the error growth of the moist case over the dry case, averaged for both the coarse and fine grids.

3.5 Initial errors in the τ field.

As one additional type of error which can be inserted into the system, initial errors in the τ field are applied in the 16 x 17 grid point model in the same magnitude as those in the ψ field, which were discussed earlier (with amplitude .05). The results of EKE growths are presented in Figure 3-11 for the dry and moist cases.

It can be seen that the moist and dry EKE values are very close until $t = 150 \times 10^3$ sec, and after that they diverge. By 400×10^3 sec, that of the moist case is 23% higher than that of the dry case, and by 600×10^3 sec, the moist case has 49% higher errors than the dry case. This is a more significant source of additional error due to moisture than was observed when initial errors were placed into the ψ field, although the total level of errors were lower. It is understandable because initial errors in τ lead more directly to errors in the θ field. Afterwards, the interaction with the moisture field comes into play with the release of latent heat. At this point, disagreements in condensation lead to further errors in the temperature field which are transferred to the wind field through the vorticity equations. A schematic diagram of this process appears in Figure 3-12.

Initial errors were also placed in the humidity field at different levels. The results of this study will be discussed in Chapter 4 after the analysis of condensation regions is examined.

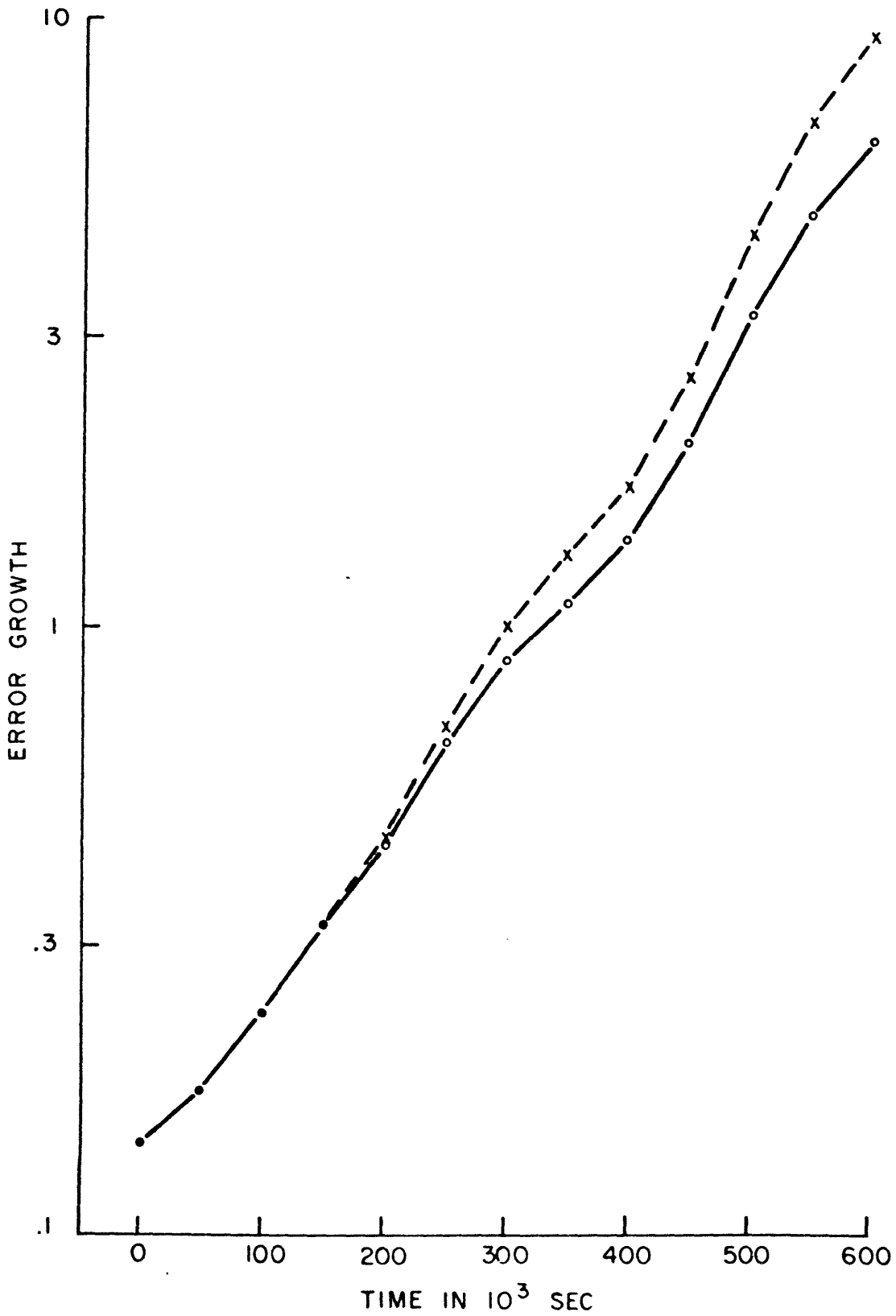


Figure 3-11. Growth of error kinetic energy for initial errors in the τ field for the dry case (solid line) and moist case (broken line).

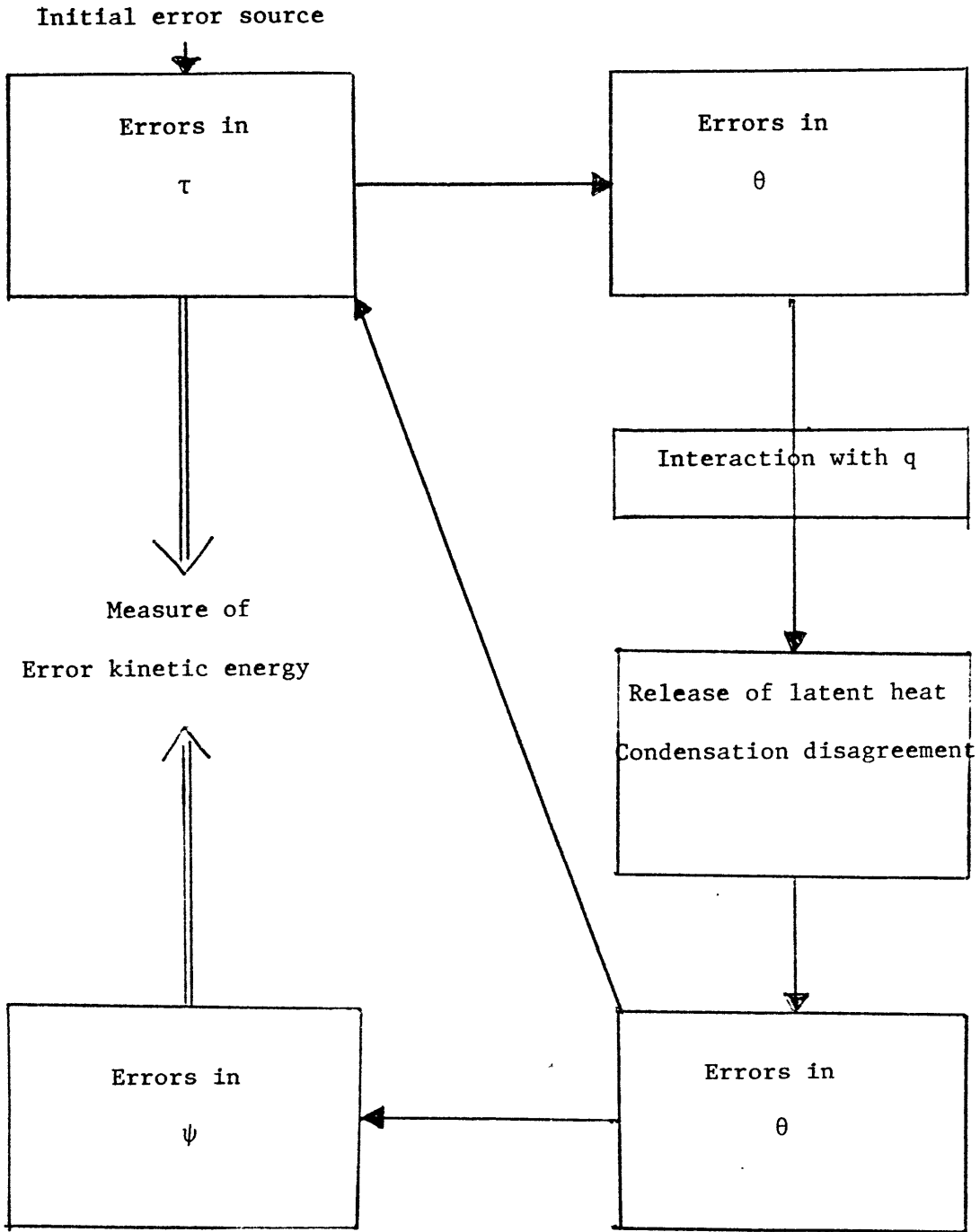


Figure 3-12. Schematic diagram of transfers of error energy.

3.6 Ekman layer effect.

Furthermore, an additional investigation was carried out in order to determine whether the omission of bottom vertical velocities would be considered a significant factor in additional error growth. To achieve this end, a vertical velocity was added to the bottom boundary of the model which would come from an Ekman layer, that is, which is proportional to the geostrophic vorticity at the top of the bottom boundary (see equation 2.22). The resultant error kinetic energy growth in both the dry and moist cases was almost identical to the growth without the Ekman term. In each case, the difference of the EKE level was only a factor of 1-2% greater.

Admittedly, an Ekman layer is not a completely realistic bottom boundary condition, especially for small scale patterns of vertical velocity. However, since this study is trying to relate the effects of large-scale moisture patterns and the effect is small on the scales treated here, it appears satisfactory for it to be eliminated from the model equations.

3.7 Dependence of EKE growth upon initial error magnitude.

The initial error perturbation placed upon the system of equations must naturally be of finite size, and so its growth might be considered dependent upon the magnitude of the error. Since the error kinetic energy can at a maximum be the total average kinetic energy of the system, there is definitely a limit to the size of the errors themselves. If the errors are considered small enough, their self-interacting terms are small compared with all the other terms in the equations and the error growth remains linear.

For example, Lorenz (1969b) considered the simple barotropic vorticity equation for a streamfunction ψ with and without time dependent error ε (that is to say, for ψ and $\psi + \varepsilon$).

$$\frac{\partial}{\partial t} (\nabla^2 \psi) = -J(\psi, \nabla^2 \psi) \quad (3.7)$$

The difference of the two solutions is then governed by the equation

$$\frac{\partial}{\partial t} (\nabla^2 \varepsilon) = -J(\psi, \nabla^2 \varepsilon) - J(\varepsilon, \nabla^2 \psi) - J(\varepsilon, \nabla^2 \varepsilon) \quad (3.8)$$

So long as $|\varepsilon| \ll |\psi|$, the growth of the errors is linear because the last Jacobian term can be disregarded. In the present, more complicated system, the same linear approximation is valid for small errors.

This is borne out by experiments using the 16 x 17 grid point model. Several sets of initial errors were chosen from random number sets of differing magnitudes and were added to the ψ field.

At this point, it is important to determine the type of error in the initial wind field which results from random errors in the streamfunction field. An error ε is chosen from a unit normal probability distribution with amplitude A:

$$p(\varepsilon) = \frac{1}{\sqrt{2\pi}} A e^{-\varepsilon^2} \quad (3.9)$$

Since the wind error is dependent upon the difference between two neighboring streamfunction values:

$$u_e = k \times \nabla \varepsilon$$

one can determine the standard deviation of wind errors from this equation. Let ε_1 and ε_2 be two adjacent values for the error ε and D the distance between the grid points. Also let the expected value of a quantity q, denoted by $\langle q \rangle$ be $\int_{-\infty}^{\infty} q p(q) dq$.

The standard deviation of wind magnitudes becomes

$$\frac{1}{D} \left[\langle (\varepsilon_1 - \varepsilon_2)^2 \rangle \right]^{1/2}$$

Since the probability distribution of ε_1 and ε_2 are independent of one another, and their expected values

$$\langle \varepsilon_1 \rangle = \langle \varepsilon_2 \rangle = 0 \quad \text{and} \quad \langle 1 \rangle = 1 \quad \text{and} \quad \langle \varepsilon_1^2 \rangle = \frac{\sqrt{\pi}}{2}$$

we obtain

$$\langle u_e \rangle = \frac{1}{D} \left[\int_{-\infty}^{\infty} \int_{-\infty}^{\infty} (\varepsilon_1 - \varepsilon_2)^2 p(\varepsilon_1) p(\varepsilon_2) d\varepsilon_1 d\varepsilon_2 \right]^{1/2} \quad (3.10)$$

Equation (3.10) reduces to

$$\begin{aligned} \langle u_e \rangle &= \left[\frac{1}{\sqrt{2\pi}} \int_{-\infty}^{\infty} \varepsilon_1^2 e^{-\varepsilon_1^2} d\varepsilon_1 + \frac{1}{\sqrt{2\pi}} \int_{-\infty}^{\infty} \varepsilon_2^2 e^{-\varepsilon_2^2} d\varepsilon_2 \right]^{1/2} \\ &= \frac{A}{D} [2 \langle \varepsilon^2 \rangle]^{1/2} = \frac{A}{D} (2)^{-1/4} \end{aligned}$$

For an amplitude $A = .05 \times 1 \text{ km}^2 \text{ sec}^{-1}$, and $D = 100 \text{ km}$, the standard deviation of initial wind errors is $.42 \text{ m sec}^{-1}$. Since the average winds are on the order of 10 m sec^{-1} , then

$$\frac{|\nabla \varepsilon|}{|\nabla \psi|} \approx .04$$

Runs were made with probability distributions of three different amplitudes

$$A_1 = .025 \quad A_2 = .05 \quad A_3 = 1 \quad (\text{in } \text{km}^2 \text{ sec}^{-1})$$

and their resultant EKE growths are shown in Table 3-5.

A comparison of two runs with amplitudes A_1 and A_2 shows that the EKE growth in case 2 remains a constant multiple of that in case 1. Since the initial errors were chosen from amplitudes differing by a factor of 2, the EKE remains linear and grows by a factor of 4, the square of 2.

However, when the third case is compared with either of the two others, it can be seen that the error growth is linear so long as the total errors do not exceed a critical factor. The quantities $\text{EKE}(A_3) / \text{EKE}(A_1)$ remains near the value 1600 or the square of $A_3 / A_1 = 40$, for quite some time, (until $t = 250 \times 10^3$ sec), at which point the error growth becomes non-linear for $\text{EKE} \gtrsim 300$. The error growth of the third case slows down as soon

Table 3-4. Error growths for initial errors of varying magnitudes.

t	EKE(A ₁)	EKE(A ₂)	EKE(A ₃)	EKE(A ₂)/EKE(A ₁)	EKE(A ₃)/EKE(A ₁)
0	.0292	.1167	46.69	3.996	1598
50	.0296	.1182	47.37	3.993	1600
100	.0357	.1430	59.82	4.006	1675
150	.0557	.2330	91.83	4.183	1648
200	.1050	.4223	178.99	4.022	1704
250	.1797	.7296	309.26	4.060	1720
300	.3096	1.2596	375.83	4.068	1213
350	.4637	1.9019	421.80	4.102	909
400	.6777	2.7487	485.22	4.056	715
450	1.2376	4.9323	512.83	3.985	414
500	2.3276	9.1974	527.62	3.951	226
550	4.4775	17.8212	589.60	3.980	131
600	9.5575	38.6227	635.06	4.041	66

as it approaches a maximum.

If N is the number of grid points, E the error kinetic energy value, and U is the dimensional quantity 10 m sec^{-1} , then the average wind deviation is

$$u_e = \left(\frac{E}{2N} \right)^{1/2} \times U \quad (3.11)$$

and in this case, for $E = 300$, $N = 272$, then

$$u_e = 7.4 \text{ m sec}^{-1}$$

and so the non-linear phase of growth can be said to begin at the point where the average error velocity is near this critical value.

3.8 Dependence of error kinetic energy growth rate on sea surface temperatures.

As was mentioned previously, the error growth in the moist model investigated here is strongly dependent upon the underlying sea surface temperatures (SST). This is partially because of the controlling factor that the sea surface temperature has upon the amount of water vapor in the moist system. A greater quantity of moisture which evaporates from the sea surface will in turn condense at a greater rate. It is the uncertainty of condensation which causes additional EKE growth, and more opportunities for condensation will cause greater uncertainty.

It has been found that additional growth in the large scale moist case is most apparent with higher sea surface temperatures ($T > 287$), below which the error growths have only a small difference from the dry model.

Several experiments were performed using the model equations. Earlier in this chapter details of EKE growth were presented representing the differences between $T = 292$ and $T = 297$. In these cases, the entire bottom boundary was an isothermal surface. However, the question of a non-isothermal distribution of sea surface temperatures becomes an important consideration.

Regions of high sea surface temperature were placed as bottom boundaries in two different forms. At first, a small region consisting of 9 grid point was set at 297 K. This was placed in the domain, the rest of which was at 292 K. This is referred to as experiment S1.

The error growth remained at a level entirely between the EKE levels of the two isothermal cases 292 and 297 throughout most of the integration. However, the error growth level for most of the integration time was much nearer that of the isothermal 297 K case than would be expected since only 3% of the surface was at 297 K while 97% was at 292 K. Table 3-6 shows the EKE growths in the $T = 292$ and $T = 297$ isothermal cases as well as experiment S1. If 100% is the total difference between the two isothermal cases EKE values, column 5 shows how much of this 100% is achieved in the EKE growth of experiment S1 above the $T = 292$ value.

time	T=292	T=297	-80- Exp. S1	(S1-292)/(297-292)
0	.1167	.1167	.1167	-
50	.1182	.1182	.1182	-
100	.1447	.1440	.1448	-
150	.2315	.2314	.2315	-
200	.4451	.4458	.4565	1.628
250	.7874	.8055	.8148	1.5138
300	1.4173	1.4916	1.4600	.3055
350	2.1865	2.3409	2.2588	.4682
400	3.2565	3.4327	3.4177	.9149
450	5.6224	5.9994	5.9065	.7536
500	9.6163	11.1495	9.9677	.2292
550	18.8517	22.6468	19.6753	.2170
600	40.3344	47.5675	42.7850	.3388

Table 3-5 Error kinetic energy (EKE) growths for sea surface temperatures T=292,T=297, and experiment S1 (see text).

This might indicate that the highest value of temperature in the domain is an important factor in error growth rather than the average value of the surface temperature.

In a further experiment, S2, the sea surface temperature was distributed so that a high spot of temperature, $S_H = 298$ was at the center and that the temperature gradually tapered off to the sides proportionally to its distance away from the center. This proportion was at an appropriate amount so that the temperature at the furthest edge was a desired low value of temperature, $S_L = 290$. This was achieved using the formula

$$S = S_H - c [(\Delta x)^2 + (\Delta y)^2]^{1/2} \quad (3.12)$$

It was found that the resultant EKE growth of experiment S2, as well as its disagreement fraction of condensation points, was similar to the values in S1.

As a further investigation, it was decided to see what would happen if the temperature of the bottom boundary were not fixed as in the previous cases, but were allowed to adjust to the air temperature above. Several different adjustment parameters γ were used. At each time step of 2×10^3 sec, the value of surface temperature was adjusted according to the formula

$$S' = (1 - \gamma) S + \gamma T_0 \quad (3.13)$$

where T_0 is the temperature of the air extrapolated to the ground, and S is the sea surface temperature.

Three values of γ were investigated, namely 10^{-4} , 10^{-3} , and 10^{-2} . To each of these corresponds a time constant T_γ , which is defined as the length of time it takes for the difference between the sea surface temperature and the air temperature to be halved, and this is calculated from

$$(1 - \gamma)^{T_\gamma / 10^3 \text{ sec}} = 1/2 \quad (3.14)$$

The following table shows time constants corresponding to different values for the quantity γ .

<u>γ</u>	<u>T_γ</u>
.1	1.8 hours
.01	19.9 hours
.001	8.0 days
.0001	80.2 days

From the values for T_γ , it would appear that the adjustment parameter is somewhere within the range .01-.001. Error kinetic energy values were observed using the adjustment parameters and it was seen that for $T = 292$ K, initially the EKE value grew to 40.3344 without adjustment, to 38.8140 corresponding to $\gamma = .001$, and to 42.0167 corresponding to $\gamma = .01$. It can be seen that the moist error growth is damped with a small adjustment but grows even greater with the larger adjustment process than without it. This is understand-

able because the larger adjustment might be thought of as an additional feedback to the system which leads to error growths.

It is possible that all the runs of the models could have been made using a temperature adjustment similar to the one here. Seemingly, this is a type of computational procedure which is an approximation. So, as a class of parameters which is inexact, this adjustment parameter is eliminated in the general case.

Chapter 4. Condensation regions.

The exact physical nature of the condensation regions is of interest in this study of the predictability of a moist atmosphere. Although one might not determine an exact cause and effect relationship, the fact that general levels of additional unpredictability due to moisture processes, as measured by error kinetic energies, are associated with the less precise location of the condensation regions is an observation which is important to investigate.

In order to begin this discussion, it is important to remind the reader that in the moist case, two simultaneous models, which are referred to as the A and B models, are running and they start out with a small initial departure from each other in the fields of the stream-function. Each time condensation occurs in the lower level at a grid point in either model at any time step, the fact is noted. The condensation regions are then analyzed with respect to what is occurring in the other model.

In order to illustrate the methods used, the fine model of 32 x 33 grid points is studied. For the particular run with random numbers as initial errors, which was discussed in Chapter 3, the spatial fields of condensation are represented in Figures 4-1 to 4-6 for time steps $T = 8 \times 10^3$ sec, 108, 208, 308, 408, and 500×10^3 sec. At a given time step and grid point, the values 0,1,2, and 3 denote the following:

- 0 condensation not occurring in either model
- 1 condensation occurring in first model (A) only
- 2 condensation occurring in second model (B) only
- 3 condensation occurring in both first and second models

In this manner, it is possible to observe the large-scale patterns of condensation for both the simultaneously running models.

Of interest is the determination of how patterns of condensation of the two models spread apart from each other in time. Near the start of the model run, the prevailing type of condensation is the 3 pattern. At $t = 8 \times 10^3$ sec, several large regions of condensation are seen distributed throughout the whole domain. There are small patches of 1 and 2 types of condensation primarily adjacent to the larger patches of type 3. This means that the condensation regions of the two models closely coincide initially. For example, the region in the upper left corner of the domain has condensation in both models, but that in model A also occurs slightly to the west of the regions of 2's and 3's, and that of B also occurs slightly to the east of 1's and 3's.

In time, the condensation of the two models tends not to agree quite as well as it did in the earlier times, although, generally speaking, regions of 1 and 2 condensation tend to be associated with condensation in the other model.

At $t = 108 \times 10^3$ sec, a general break-up of large regions of condensation that occurred at former times is seen. In general, the streamfunctions are associated with westerly winds, and regions of

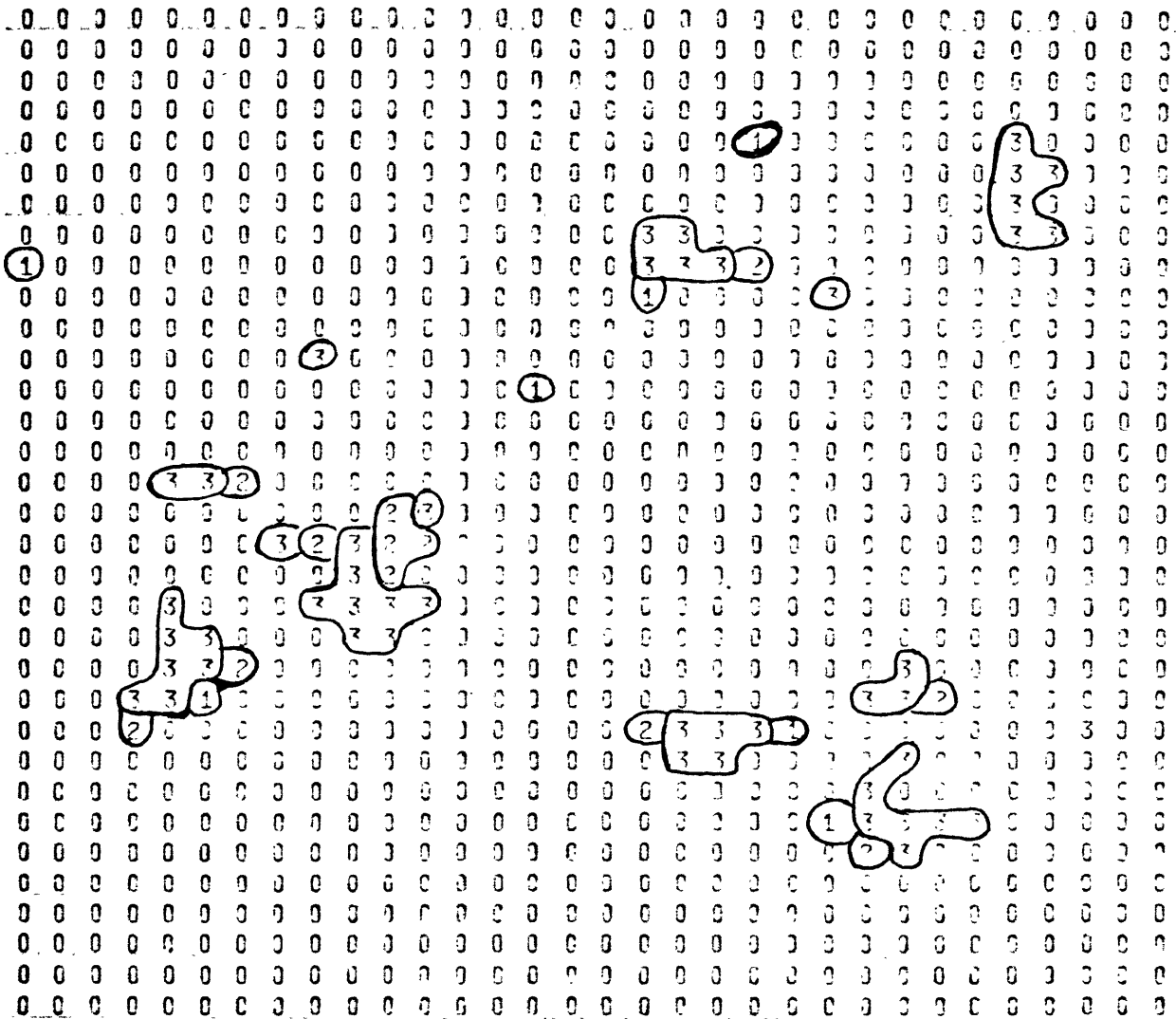


Figure 4-2. Condensation regions for particular run at $t = 108 \times 10^3$ sec.

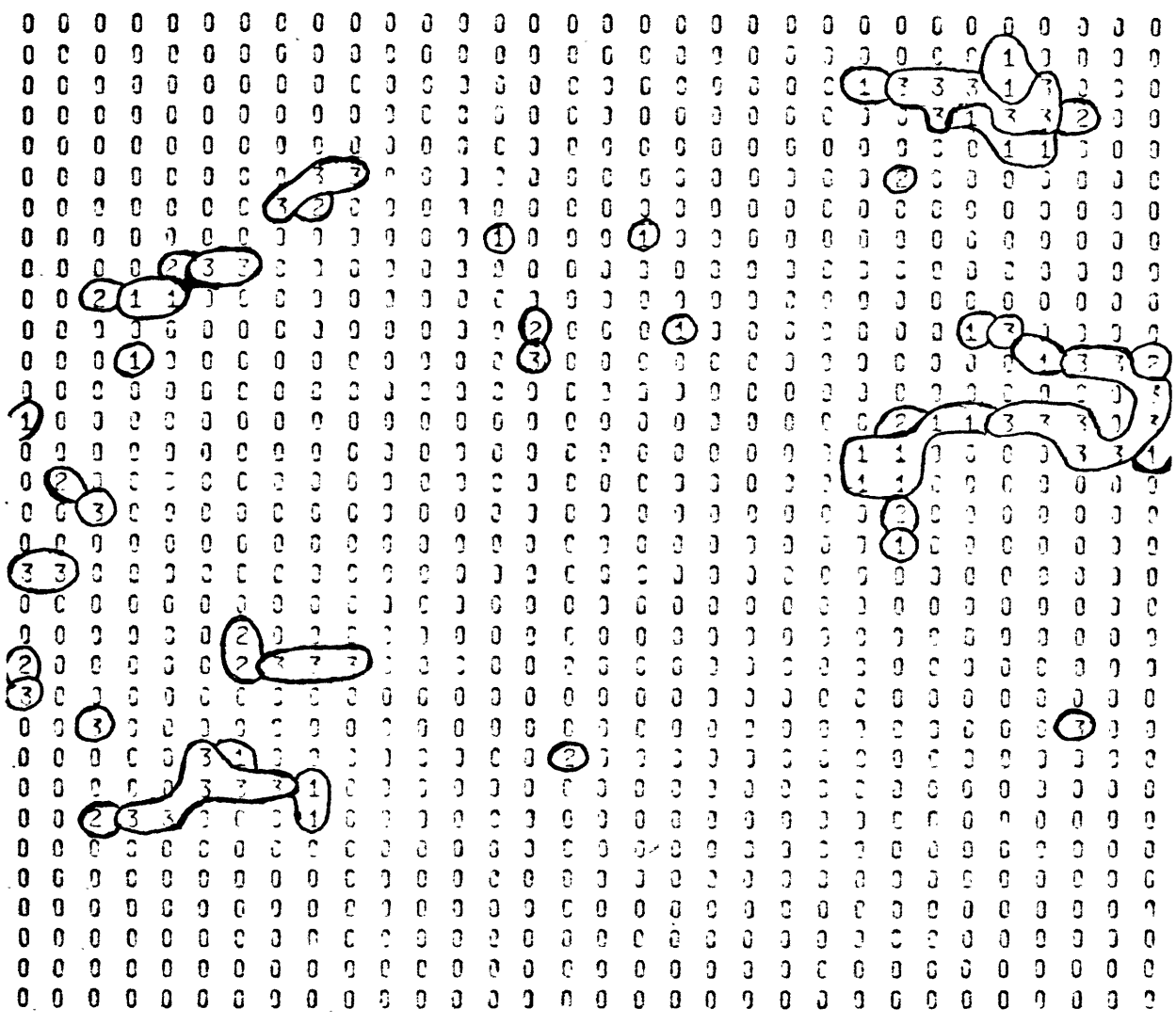


Figure 4-3. Condensation regions for particular run at $t = 208 \times 10^3$ sec.

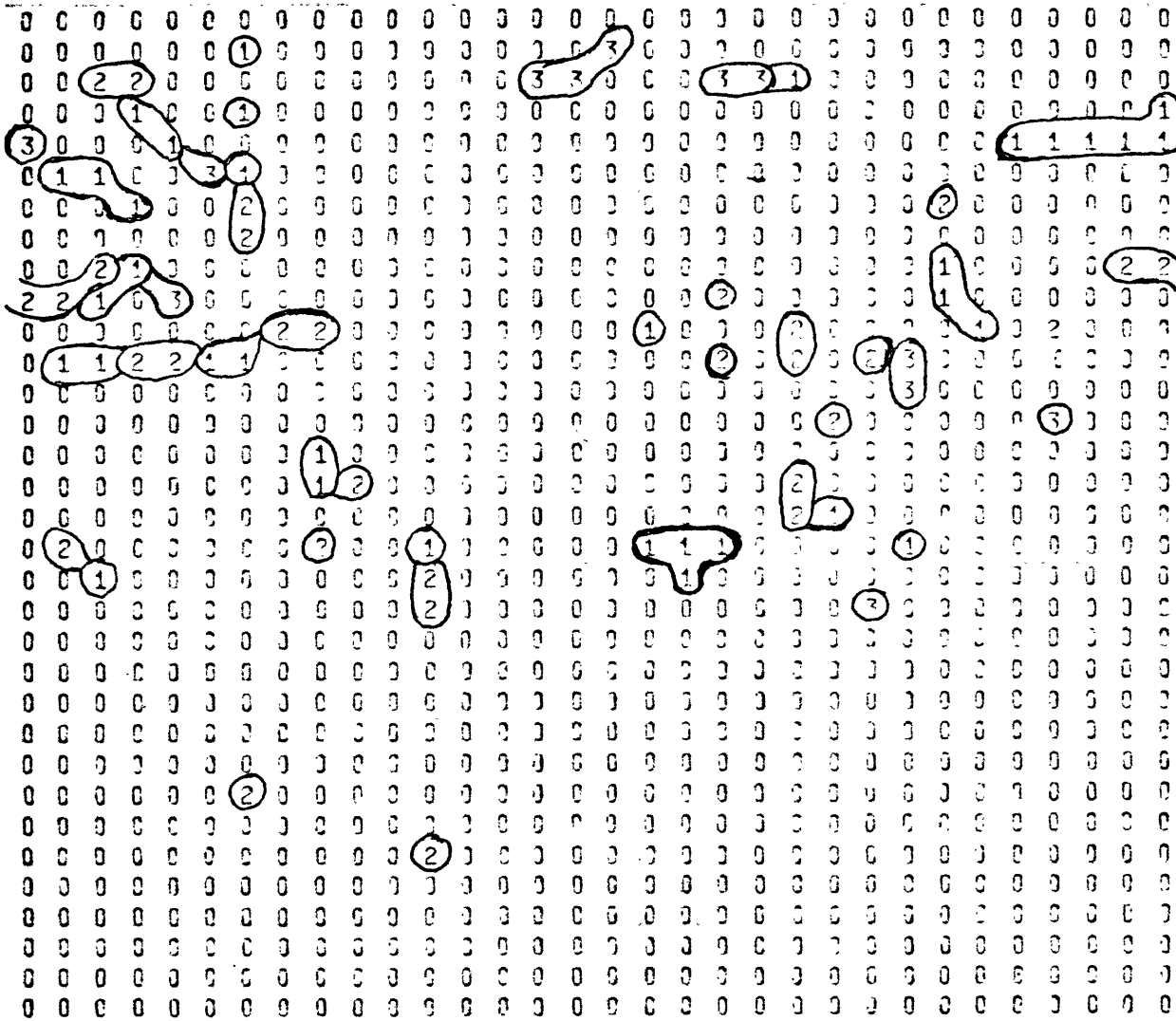


Figure 4-6. Condensation regions for particular run at $t = 500 \times 10^3$ sec.

condensation tend to stay in the same latitude belt in the model. The two regions of largely 3 type of condensation in the northern part of the domain are associated with the past 3 region in the northwesterly part of the domain at $t = 8 \times 10^3$ sec. It can be seen that there are more 1's and 2's in the patterns and that they again fall adjacent to the other model's type of condensation.

By $t = 208 \times 10^3$ sec, some of the condensation regions are changing their shape more radically. It should be remembered that, according to the model, condensation is occurring only in the cases where 80% of the saturation water vapor levels is reached as well as where the vertical velocities are upwards. Thus condensation reflects the interaction of several fields, that is the streamfunction, temperature and absolute humidity fields, which then determine the relative humidity and vertical motion fields.

At this time step, the interactions of the above mentioned fields lead to more convoluted condensation regions with a higher proportion of "disagreement" condensation regions. Additionally, there are some isolated patches of 1 and 2 type of condensation, which are spreading away from the main regions. This type of structure is seen as well at $t = 308 \times 10^3$ sec.

By $t = 408 \times 10^3$ sec, whole regions of 1 and 2 type of condensation have been generated. For example, the 1 region marked P is adjacent to the 2 region denoted Q. There is as well a separate 1 region denoted by R and a predominantly 2 region marked S near each other. However, there is still one large region of 3 type of condensation which practically disappears by $t = 500 \times 10^3$ sec. At that time,

there are several isolated patches throughout the domain of 1 and 2 type of condensation, and the type of condensation regions in models A and B are considerably different in form from each other.

The proportion of disagreements in condensation points to the total number of condensation grid points is kept account of. This fraction is seen in Table 4-1 and Figure 4-7. In the figure, average fractions of disagreements over the time steps 4-48, 28-72, 52-100, 76-124, 104-148, 128-172, etc., (curve a) are plotted at the center of the above time intervals. They are averaged in this manner because of the rapid variations in time about the general trend. Near the start of the runs, the average fraction of disagreements is small, about .15. This quantity rises to .21 by $t = 100$, and then begins a more rapid growth during the interval $t = 100-200$. Then the disagreement fraction begins a more gradual growth from .48 until it reaches .85 at $t = 500$.

The 50% level is obtained at approximately $t = 270$, or a period of 3.1 days. If average initial errors are not smaller than the ones applied here, which are about $.5 \text{ m sec}^{-1}$ in the wind field, one can make the implication that after 3 days, a prediction of condensation using a model such as this one, will not be correct more than 50% of the time due to the growth of small initial errors. The fraction will be reduced additionally due to the other faults of the model itself.

Table 4-1. Average fractional number of disagreement condensation grid points to total condensation grid points and dispersion distances D_1 and D_2 .

<u>Interval</u>	<u>Average fraction</u>	<u>D_1</u>	<u>D_2</u>
4-24	.1556	1.1436	.1822
4-48	.1737	1.3722	.2434
28-72	.1860	1.5195	.2763
52-100	.1882	1.3440	.2521
76-124	.2091	1.3383	.2891
104-148	.2494	1.2985	.3359
128-172	.2959	1.4155	.4252
152-200	.3796	1.7271	.6481
176-224	.4752	1.6994	.7790
204-248	.4818	1.5828	.7686
228-272	.5093	1.5814	.7958
252-300	.5735	1.5049	.8554
276-324	.5774	1.5522	.8942
304-348	.6007	1.6561	.9969
328-372	.6497	1.7345	1.1255
352-400	.6891	1.8118	1.2604
376-424	.7205	1.9151	1.3918
404-448	.7312	1.9293	1.4128
428-472	.7614	1.8614	1.4180
452-500	.8146	1.9623	1.6006
476-500	.8435	2.0205	1.7030

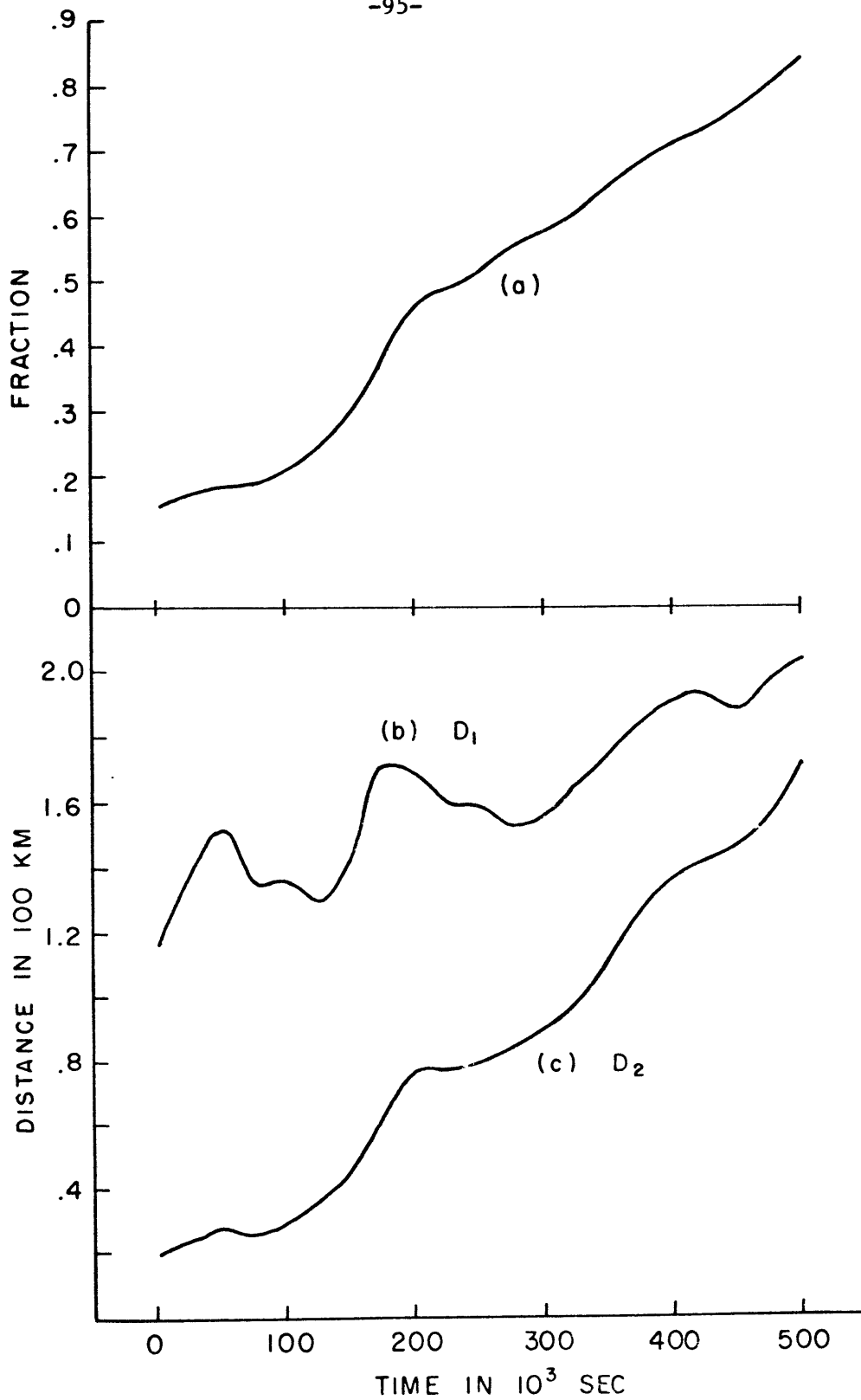


Figure 4-7. (a) Average fractional condensation disagreement points, (b) dispersion distance D_1 (disagreement points only), and (c) dispersion distance D_2 (all condensation points).

4.1 Dispersion of condensation regions.

The dispersion between the condensation regions of the two simultaneous models is measured in the following manner. If condensation occurs at a grid point in one model, then it is of interest to determine the distance to the nearest grid point in the other model at which condensation occurs. It can be assumed that when condensation does not occur at the exact location in the other model, then the nearest location where it does occur is associated with the condensation point in this model.

The points at which condensation occurs can be described as a set $\{P_i\}$, which can be ordered so that the distance to the nearest condensation point in the other model is increasing with increasing i . The minimum distance for each point P_i is termed d_i . At a particular time step t , there are $L(t)$ condensation points, $K_0(t)$ being the number of agreement points and $K(t)$ being the number of disagreement points. Therefore, $L(t) = K_0(t) + K(t)$. For each of the K_0 points, $i = (1, K_0)$, $d_i = 0$, and for each of the K points, $i = (K_0 + 1, L)$, $d_i > 0$.

The average quantities for d_i and their behavior in time are interesting to analyze and are done so in Table 4-1 and Figure 4-7. The third column in the table and curve (b) in the figure refer to the average distance to the nearest condensation point in the other model but only for the "disagreement" points, $\{P_i\}$, $i = (K_0 + 1, L)$. This is $\bar{D}_1 = \frac{1}{K} \sum_{i=K_0+1}^L d_i$. The minimum possible

value for this average is 1.0 because the minimum possible distance to another grid point is 1.0 units.

The average distance away including all condensation points, for both agreement and disagreement grid points, which is

$$\bar{D}_2 = \frac{1}{L} \sum_{i=1}^L d_i$$

, is seen as column 4 in Table 4-1 and curve (c) in Figure 4-7. The minimum possible value for \bar{D}_2 is 0.0, which would occur if there were only agreement condensation points and no disagreement ones. In the above table and figure, the value of \bar{D}_1 and \bar{D}_2 are averaged over several time steps, those being the ones described for the average fraction of condensation disagreements.

The quantities \bar{D}_1 and \bar{D}_2 are, generally speaking, two increasing functions of time and this indicates that the average associated distance is increasing with time. The reason that \bar{D}_2 is increasing more steadily than \bar{D}_1 is that in \bar{D}_1 , a larger fraction of condensation points are being included in the average.

By $t = 500$, the quantity \bar{D}_2 has grown by a factor of 9.3. In prediction of condensation by this model, the average error distance in predicting condensation regions will grow by a factor of 4 in 3 days and by about a factor of 10 in 6 days, due to growth of small initial errors alone.

The dispersion of condensation regions can be seen even more so when one observes the distribution in time of d_i for $i = 1, L$. For each time step, the fraction of values for d_i which fall in

the interval $J-1 < d_i < J$ for $J \geq 1$ can be denoted by $D(J)$. In this manner

$$\sum_{J=1}^{\infty} D(J) = 1.0$$

Furthermore, this process can be done for all the condensation points within an interval of time steps. Table 4-2 has the distribution of $D(J)$ for the time steps 4-48, 52-100, 104-148, 152-200, etc.

The values of this distribution are plotted in Figure 4-8 for every other time interval of Table 4-2. It can be seen that the fraction of minimum distances which occur in the interval $0 \leq d < 1$ is a monotonically decreasing function of time. However, the fraction whose minimum distance is within a certain space interval is a constantly increasing function of time for each space interval other than $0 \leq d < 1$. Again, this shows how the condensation regions are spreading out in time.

The part of each individual curve which is greater than $J=1$ during each time interval can be approximated with some accuracy by both a decaying exponential curve (be^{-cx}) and by a decaying square-exponential curve (Gaussian) (be^{-cx^2}). The procedure for determining the parameters b and c in each case to best fit the data with a least-square fit is described in detail in Appendix 2. Table 4-3 represents the parameters which create the best fitting curves for both be^{-cx} and be^{-cx^2} , as well as the standard deviation value $c^{-1/2}$ for the Gaussian fit.

The fact that the total area under the curves is not equal to 1 is explained by the fact that they do not include the first point,

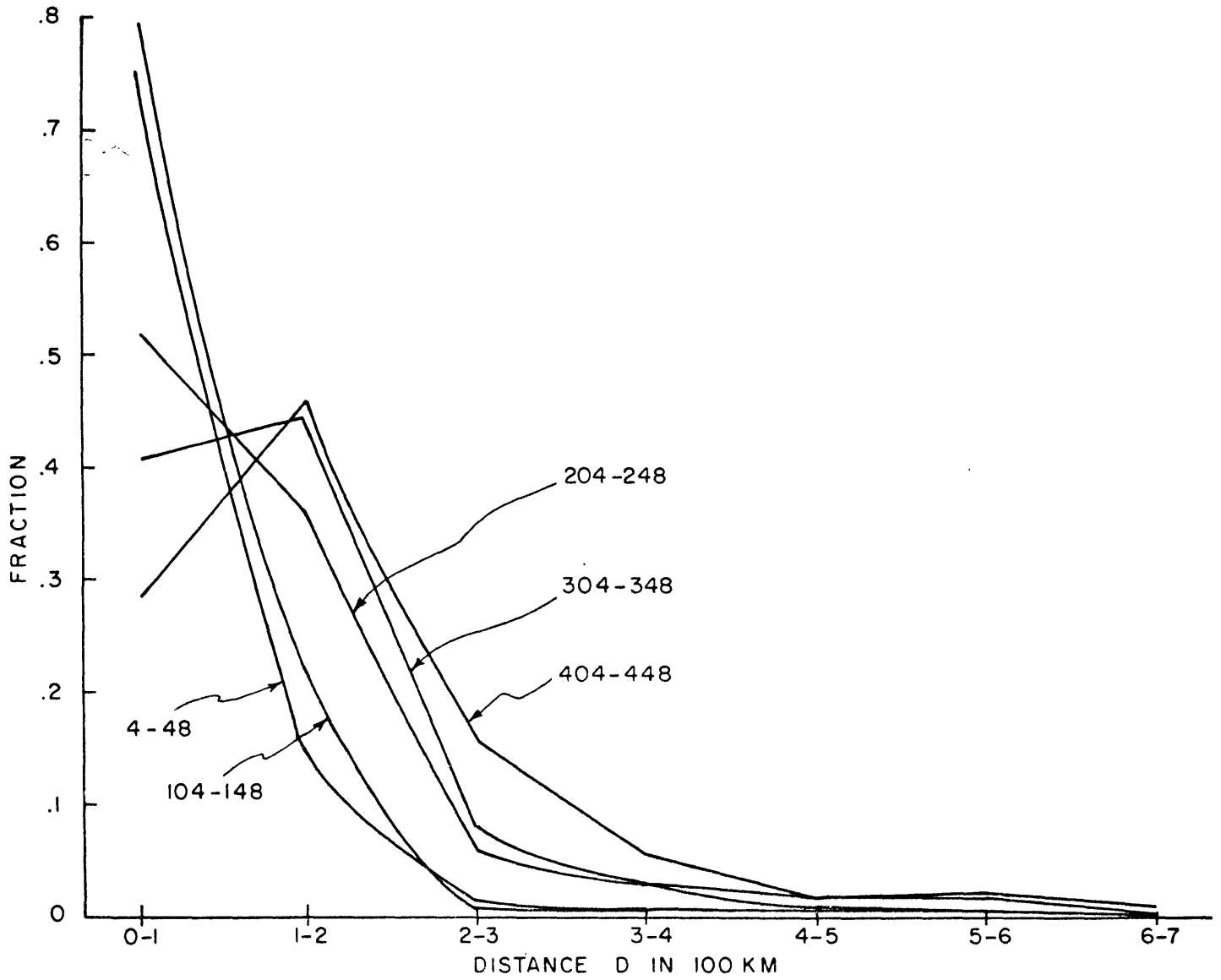


Figure 4-8. Fraction of condensation occurring at dispersion distances for selected time steps.

Table 4-2. Distribution of condensation dispersion distances for time intervals

time	Distances in 100 km								
	0-1	1-2	2-3	3-4	4-5	5-6	6-7	7-8	8-9
4-48	.8262	.1457	.0145	.0096	.0039	.0000	.0000	.0000	.0000
52-100	.8127	.1567	.0189	.0071	.0035	.0012	.0000	.0000	.0000
104-148	.7519	.2201	.0097	.0108	.0032	.0033	.0011	.0000	.0000
152-200	.6203	.2733	.0520	.0217	.0145	.0021	.0048	.0012	.0000
204-248	.5197	.3630	.0627	.0303	.0131	.0081	.0010	.0000	.0010
252-300	.4756	.3811	.0945	.0256	.0112	.0056	.0032	.0016	.0016
304-348	.4053	.4443	.0797	.0303	.0151	.0175	.0031	.0039	.0007
352-400	.3112	.4669	.1022	.0256	.0276	.0184	.0073	.0027	.0009
404-448	.2824	.4524	.1463	.0542	.0256	.0205	.0091	.0061	.0020
452-500	.1898	.4938	.2148	.0719	.0220	.0163	.0068	.0038	.0029

Table 4-3. Best fit curves for decaying exponential, square exponential, and standard deviation (in units of 100 km)

<u>Time</u>	<u>b₁</u>	<u>c₁</u>	<u>b₂</u>	<u>c₂</u>	<u>c₂^{-1/2}</u>
4-48	1.2983	2.188	.3102	.7560	1.150
52-100	1.2154	2.049	.3139	.6950	1.200
104-148	4.6240	3.045	.6215	1.038	.982
152-200	1.2804	1.547	.4640	.5310	1.372
204-248	1.8616	1.637	.6365	.5630	1.332
252-300	1.5046	1.374	.5952	.4480	1.494
304-348	2.2683	1.632	.7731	.5550	1.342
352-400	1.7432	1.324	.7366	.4610	1.473
404-448	1.3261	1.079	.6328	.3430	1.707
452-500	1.2216	.900	.6354	.2590	1.965

that is, all distances greater than or equal to zero and less than one (that is, only zero distance.) For the total magnitude to be equivalent for all the time intervals, the value for b should be divided by the total fraction of non-zero distances.

It is clear that whenever condensation occurs in model A the distance to the nearest condensation point in B (and vice versa) is a distribution which changes in time and becomes a flatter distribution as time t increases. This distribution would contribute to a spectrum of error impulses, which is the subject of a later section.

4.2 Theoretical spectrum of imparted error impulses.

In the situation where two simultaneous models, with a small initial departure from each other are running with time, each case of condensation at a grid point represents an impulse of energy into the system because of the release of latent heat. If condensation occurs at the same grid point during the same time step, it will be assumed that equal quantities of energy are being imparted to the A and B models and so no error energy is added to the system. If, however, a condensation impulse occurs in one model and not at the simultaneous grid point in the other, error energy is then imparted into the system.

The probability of condensation occurrence is dependent upon a number of factors. First, it can be assumed that as one of them, the probability of condensation at a grid point in one model is dependent upon the distance away from the grid points which are condensing in the other, simultaneous model. Furthermore, it is dependent upon a certain non-negative field which multiplies the first distribution. This field is positive when condensation can occur (that is, with upward motion and relative humidity above a necessary threshold) and zero when condensation cannot occur. Its magnitude when positive is proportional to the value for $\omega = \frac{dp}{dt}$

As one reasonable assumption the probability distribution

with respect to the distance can be thought of as a Gaussian whose standard deviation is a distance away which varies with the model type and time. This assumption is related to the statistical dispersion of condensation regions and their distribution with time, as described earlier in this chapter.

Appendix 3 describes a procedure to determine how the error impulses imparted to the system are decomposed to their spectral components. In both one-dimensional cyclic and two-dimensionally singly cyclic domains, the resulting spectral components are determined from various values of standard deviation distance of the Gaussian distribution and also for various sets of fields which form the multiplicative factor as described above.

The study of an imparted error energy impulse spectrum is important so that one can determine in which scales errors appear first. This can be tied in to other theoretical studies which describe fluid motions using observed atmospheric energy spectra. With the addition of an error energy impulse spectrum, a future study might yield better estimates of predictability times at different atmospheric scales.

The form of G_n , the one dimensional spectral component of wavenumber n and that of G_{n_x, n_y} , the two dimensional spectral component of wavenumber (n_x, n_y) from a grand ensemble of condensation points have expected values (see Appendix 3)

$$\langle G_n \rangle = \frac{1}{N} \sum_{m_0=0}^{N-1} \left[e^{2\pi i m_0 n / N} - \sum_{m=0}^{N-1} \frac{\rho}{a\sqrt{2\pi}} \int_{x_m - \frac{\Delta x}{2}}^{x_m + \frac{\Delta x}{2}} dx e^{-\left(\frac{|x-x_0|}{a}\right)^2} e^{2\pi i m n / N} \cdot [-\omega_m] \right]$$

(1-D case)

where $x_m = m \cdot \Delta x$ and

$$\langle G_{n_x, n_y} \rangle = \frac{1}{N^2} \sum_{m_y=0}^{N-1} \sum_{m_x=0}^{N-1} \left[e^{2\pi i \vec{m}_0 \cdot \vec{n} / N} - \sum_{m_y=0}^{N-1} \sum_{m_x=0}^{N-1} \frac{\rho}{a^2 2\pi} \int_{y_m - \frac{\Delta y}{2}}^{y_m + \frac{\Delta y}{2}} dy \int_{x_m - \frac{\Delta x}{2}}^{x_m + \frac{\Delta x}{2}} dx e^{-\left[\left(\frac{x-x_0}{a}\right)^2 + \left(\frac{y-y_0}{a}\right)^2\right]} \cdot e^{2\pi i \vec{m} \cdot \vec{n} / N} [-\omega_{m_x, m_y}] \right]$$

(2-D case)

where $x_m = m_x \Delta x$ and $y_m = m_y \Delta y$. The quantities $[-\omega]$ are the multiplicative factor fields and are dependent upon the vertical velocity.

In the one dimensional case, the factor fields tested are

$$(1) \quad [-\omega_{m_x}] = 1 \quad m_x = (0, N-1)$$

$$(2) \quad [-\omega_{m_x}] = \begin{cases} 1 \\ 0 \end{cases} \quad \begin{aligned} m_x &= (0, \frac{N}{2} - 1) \\ m_x &= (\frac{N}{2} + 1, N - 1) \end{aligned}$$

The second set of conditions represents cell motion of half rising, half sinking fluid.

Figures 4-9 and 4-10 reveal the spectrum of error impulses for wavenumbers 1-16 per wavenumber, imparted for each of the above two cases for $N = 32$. Wavenumber k represents that scale whose wavelength is $\frac{N}{k}$ x grid point spacing. In the case where the grid point spacing is 100 km, wavenumber 16 has a scale of 200 km and wavenumber 2 has a scale of 1600 km.

All values of error impulses are in units of $-\frac{LF}{p}\omega$ (see Chapter 2), which is the amount of heat released at condensation for a value $\omega = -10^{-3}$ mb sec⁻¹. Since $L = 2520$ erg/gm, $F \approx .012$, and $p = 750$ mb, the error impulses are in units of 4×10^{-5} erg/gm sec⁻¹.

The standard deviation refers to that of the Gaussian probability distribution. It can be seen that the highest levels of error energy are imparted to the highest wavenumbers. Though that is the case, the differences with respect to wavenumber at the higher wavenumbers (smaller scale) are not quite as great because of almost horizontal lines in constant error energy levels in the figure. In Figure 4-9, for example, a standard deviation of 1.0 (100 km) for disagreement condensation, wavenumber 8 has .025

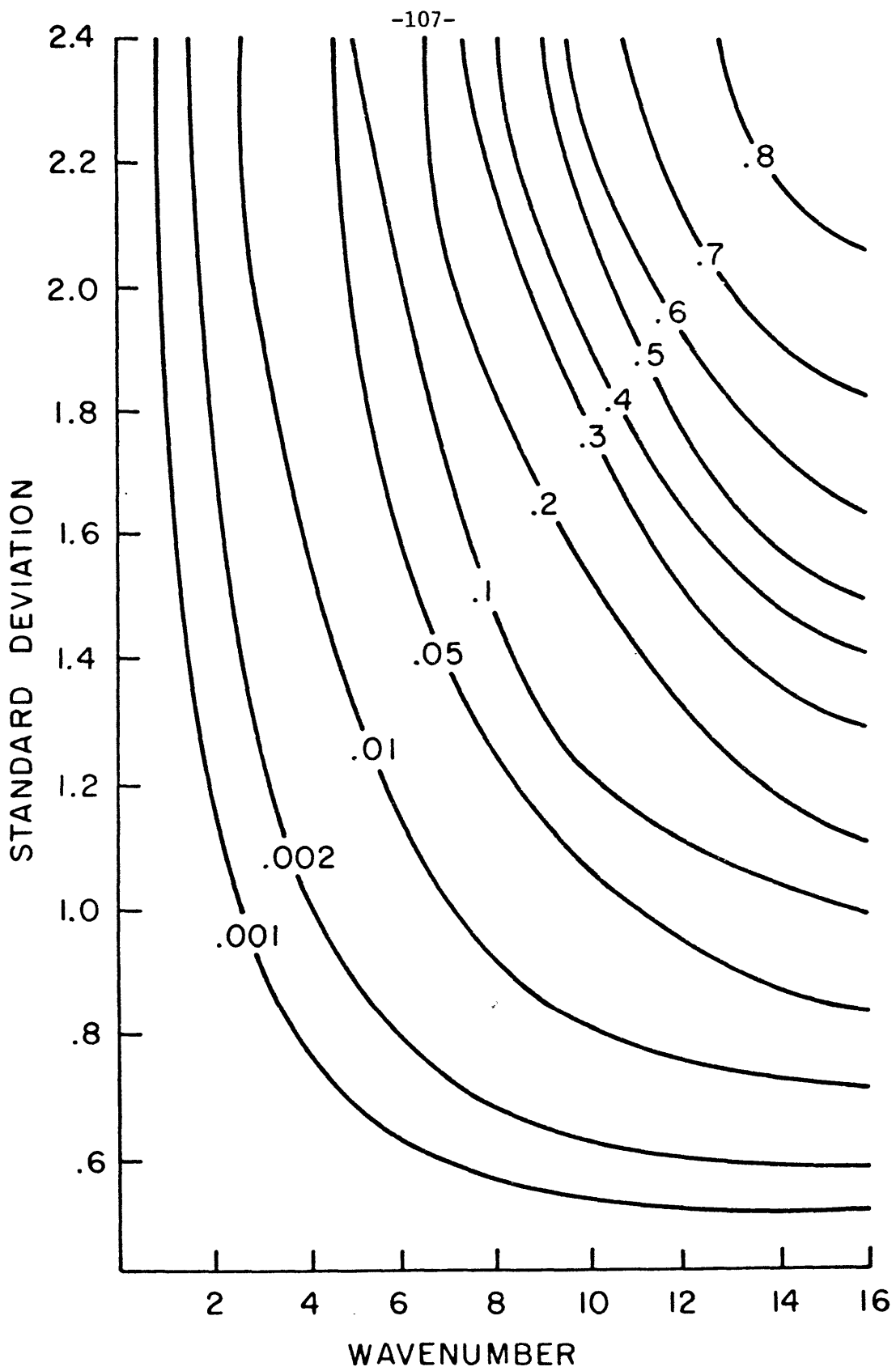


Figure 4-9. Error impulses as a function of wavenumber and standard deviation of Gaussian fit (one-dimensional case) See text.

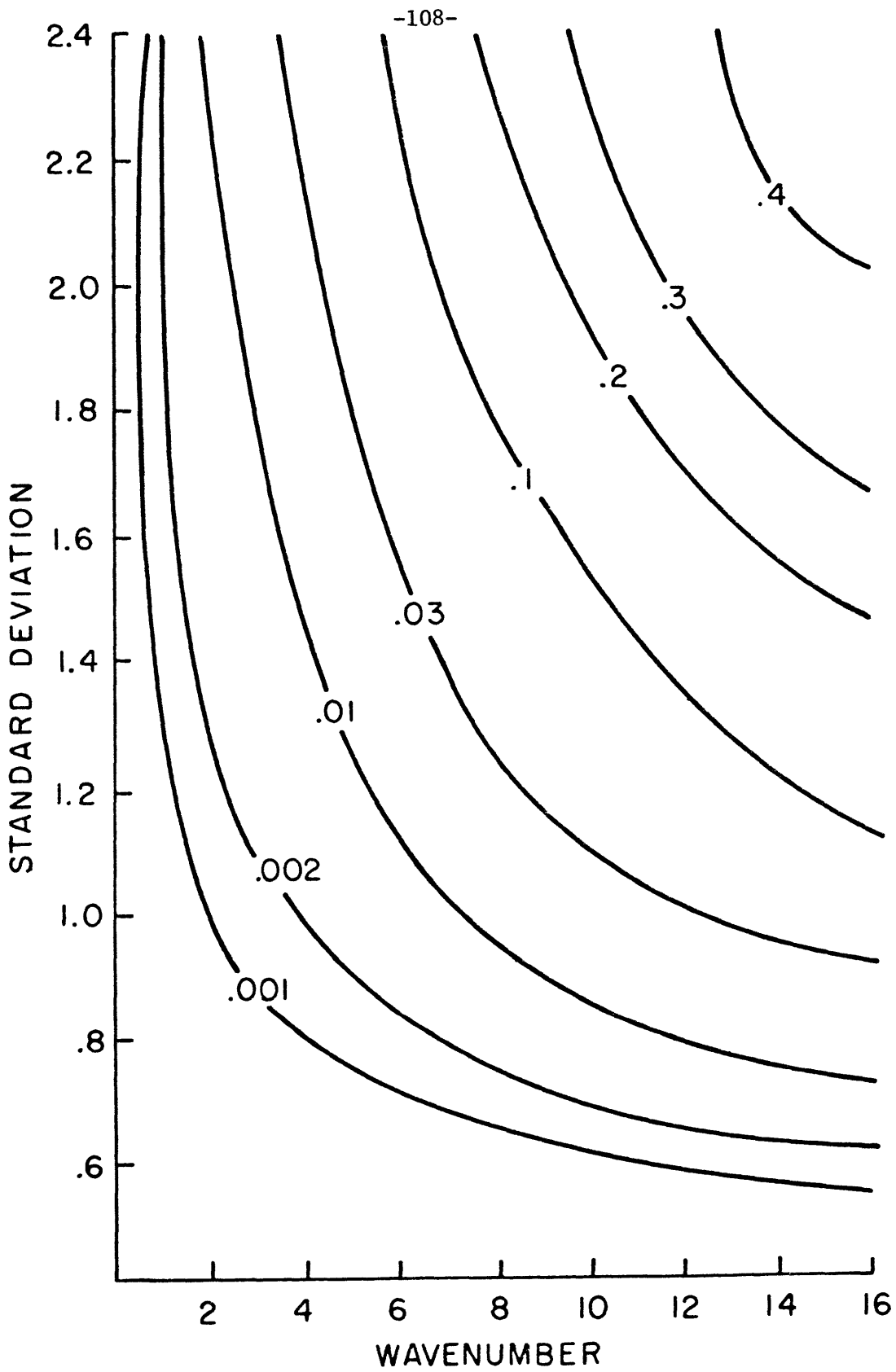


Figure 4-10. Error impulses as a function of wavenumber and standard deviation of Gaussian fit (one-dimensional case, half rising, half sinking)

units of error energy imparted to it. For a standard deviation double that, 2.0, the same wavenumber has an error energy of .263 imparted to it, or an additional factor of 10.5.

In the second case (half ones, half zeros), the distribution of error energy imparted is similar in structure to that of the first case, but is approximately half the error energy for corresponding wavenumbers and standard deviation levels, because on the average, only half of the condensation can occur.

For the two-dimensional case, error energy impulses per scalar wavenumber were imparted as a distribution of wavenumber and standard deviation of the Gaussian fit. These were computed for (1) a multiplicative factor $[-\omega]$ which are all ones and (2) for a multiplicative factor which is representative of one of the $[-\omega]$ fields occurring in the model. These are presented in Figures 4-11 and 4-12. The two-dimensional error impulse distributions were computed however, for a 16 x 16 grid point domain where the length was 3200 km. The scalar wavenumbers from 1 to 12 are computed as in the appendix.

As in the one-dimensional case, the error imparted per wavenumber increases with scalar wavenumber for each value of standard deviation. In Figure 4-11, for example, at wavenumber 8, the increase from standard deviation 1.0 to 2.0 involves increase in impulse from 1.3 to 8.6 units, and for the representative $[-\omega]$ case, (Figure 4-12) from 1.15 to 7.25, or factors of 6.5 and 6.3 respectively.

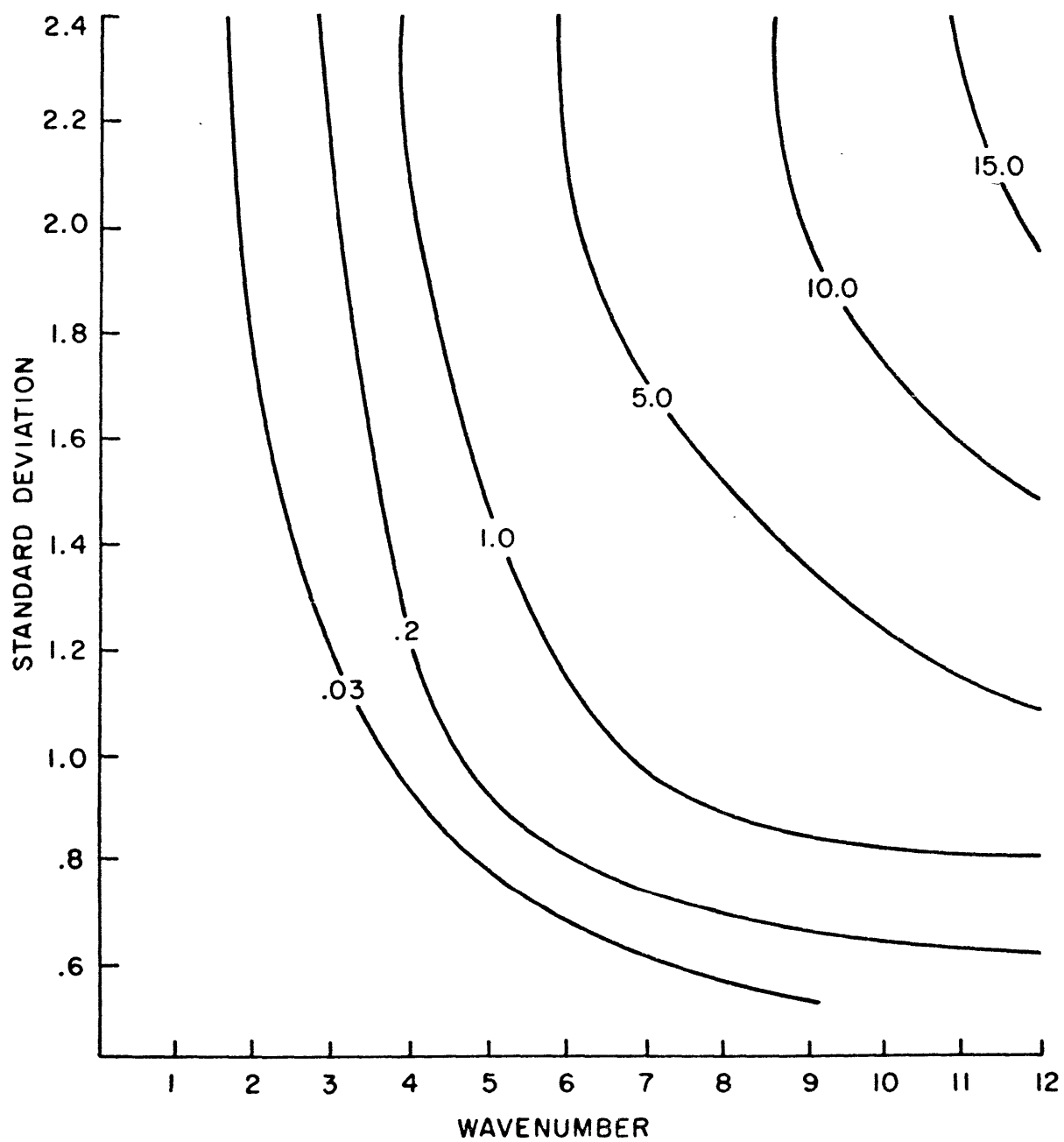


Figure 4-11. Error impulses as a function of wavenumber and standard deviation of Gaussian fit (two-dimensional case).

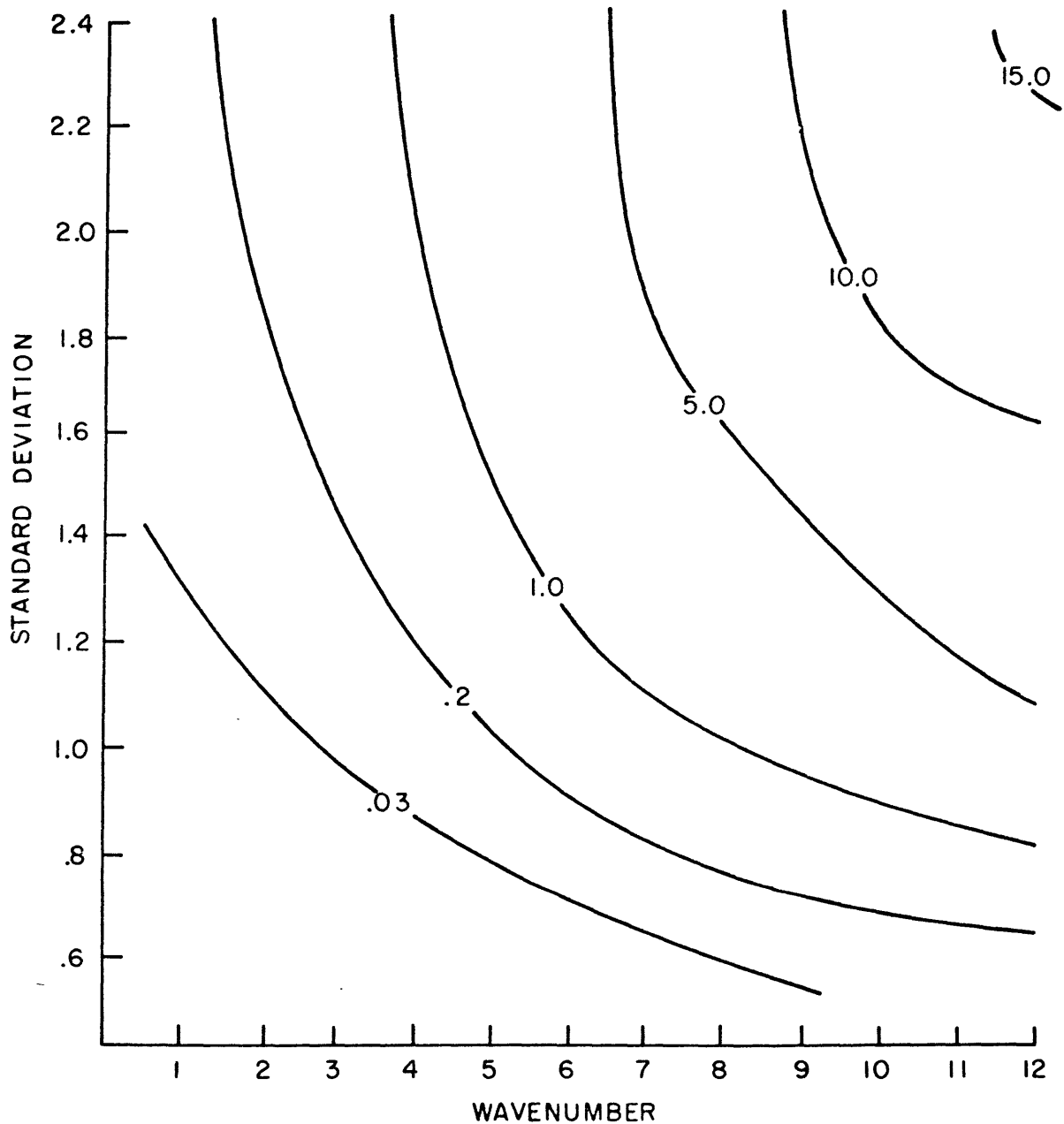


Figure 4-12. Error impulses as a function of wavenumber and standard deviation of Gaussian fit (two-dimensional case, for a typical ω field.)

It is not clear whether the representative multiplicative factor should be included, or whether its influence is actually already included when the standard deviation distance for the Gaussian is obtained. In any case, from the start of the model run to $t = 500 \times 10^3$ sec, the standard deviation distance increases from approximately 1.0 to 2.0 units, and so the error impulse is actually an additional factor of about 6.4.

As a further study, it was decided to use the probability distribution from Table 4-2 for each time interval for the specific run cited in the earlier part of this chapter as a factor for determining $p(x, x_0)$ (see Appendix 3) instead of the Gaussian method. The error impulses for each time interval as a function of wavenumber from one to 12 are shown in Figure 4-13 from the start of the model run to $t = 500 \times 10^3$ sec. It can be seen that at the start of the run, for example, during the time interval $4-48 \times 10^3$ sec, the error impulses are indeed similar to those of the Gaussian fit of Figure 4-12. However, one chief difference is that for advanced values of time, the error energy impulses at the smallest wavenumbers are greater than in the Gaussian case.

Total amounts of error energy which are imparted to the system can be approximated by the integral

$$E_{err} = \iint E(k) dk dt$$

where $E(k)$ is the energy per scalar wavenumber per time. As an

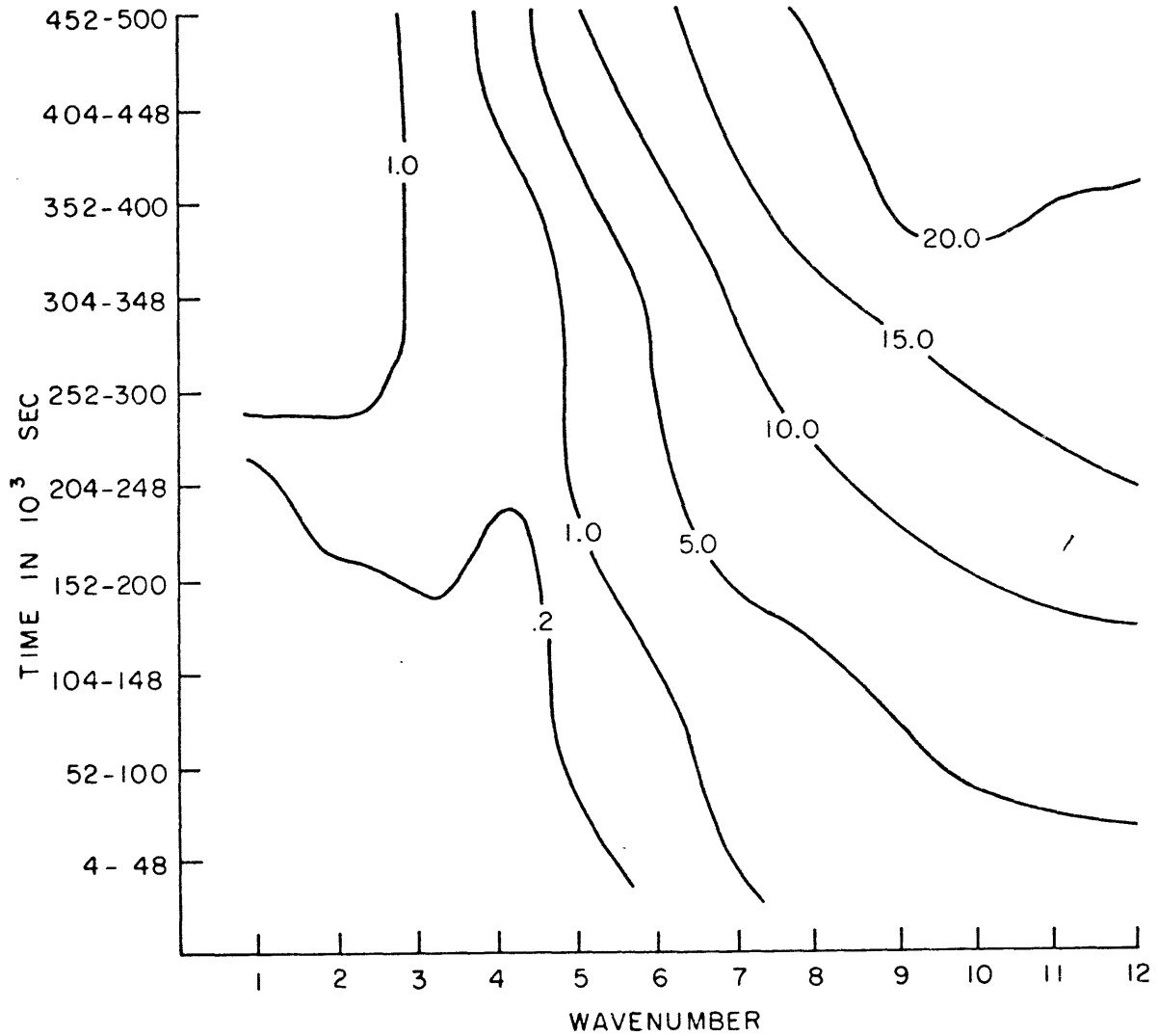


Figure 4-13. Error impulse as a function of wavenumber and time interval for a typical run with condensation dispersion. (Two-dimensional case)

example, in the 32 x 33 grid point model, the value for the run with E (k) as in Figure 4-13 is equivalent to

$$1852 \times 50 \times 10^3 \text{ sec} \times 4 \times 10^{-5} \text{ erg gm}^{-1} \text{ sec}^{-1}$$

which, by $t = 500 \times 10^3 \text{ sec}$, is applied directly to error energy, and would be equivalent to a root-mean-square error wind of $.61 \text{ m sec}^{-1}$. The difference in error kinetic energies between the dry and moist cases of the model of 36.6 units is equivalent to 1.86 m sec^{-1} , or close to 3 times the imparted equivalent error wind value. So the error introduced directly from condensation disagreement is only about 1/6 of the eventual error kinetic energy. The balance of the error kinetic energy comes from interactions themselves between the temperature and streamfunction fields.

4.3 Effect of initial errors in the humidity field.

Several runs of the 16 x 17 model were made in order to determine how errors will grow from a case in which initial errors are placed in the humidity field. As the only initial perturbation, normal random numbers were added to the q_1 field at several amplitudes. (Amplitudes denote the factor multiplying numbers in a normal (0,1) distribution.) The level of error kinetic energy is shown in Figure 4-14 for three average perturbation amplitudes: (a) 1 gm kg^{-1} , (b) 2.5 gm kg^{-1} and (c) 5 gm kg^{-1} .

Since initially there is not error kinetic energy, (no initial ψ and τ errors), the only EKE is generated by means of interaction of the humidity and motion fields, which occurs indirectly only as a result of condensation, and more specifically, "disagreement" condensation.

The fractional growth rate of EKE in all amplitude cases is similar. Between $t = 100 \times 10^3 \text{ sec}$ and $600 \times 10^3 \text{ sec}$, EKE grows from .0009 units to 1.3548 units in the $\Delta q \approx 1 \text{ gm kg}^{-1}$ case, from .0026 to 5.7751 in the $\Delta q \approx 2.5 \text{ gm kg}^{-1}$ case, and in the $\Delta q \approx 5 \text{ gm kg}^{-1}$ case, or by factors of 1505, 2221 and 1577 respectively.

For the various runs, the average fraction of the number of disagreements in condensation averaged sequentially over each $50 \times 10^3 \text{ sec}$ are plotted in Figure 4-15. In both cases the disagreement fractions exhibit similar behavior except in the order of magnitude, which differs by a factor of approximately 2.6 between cases (a) and

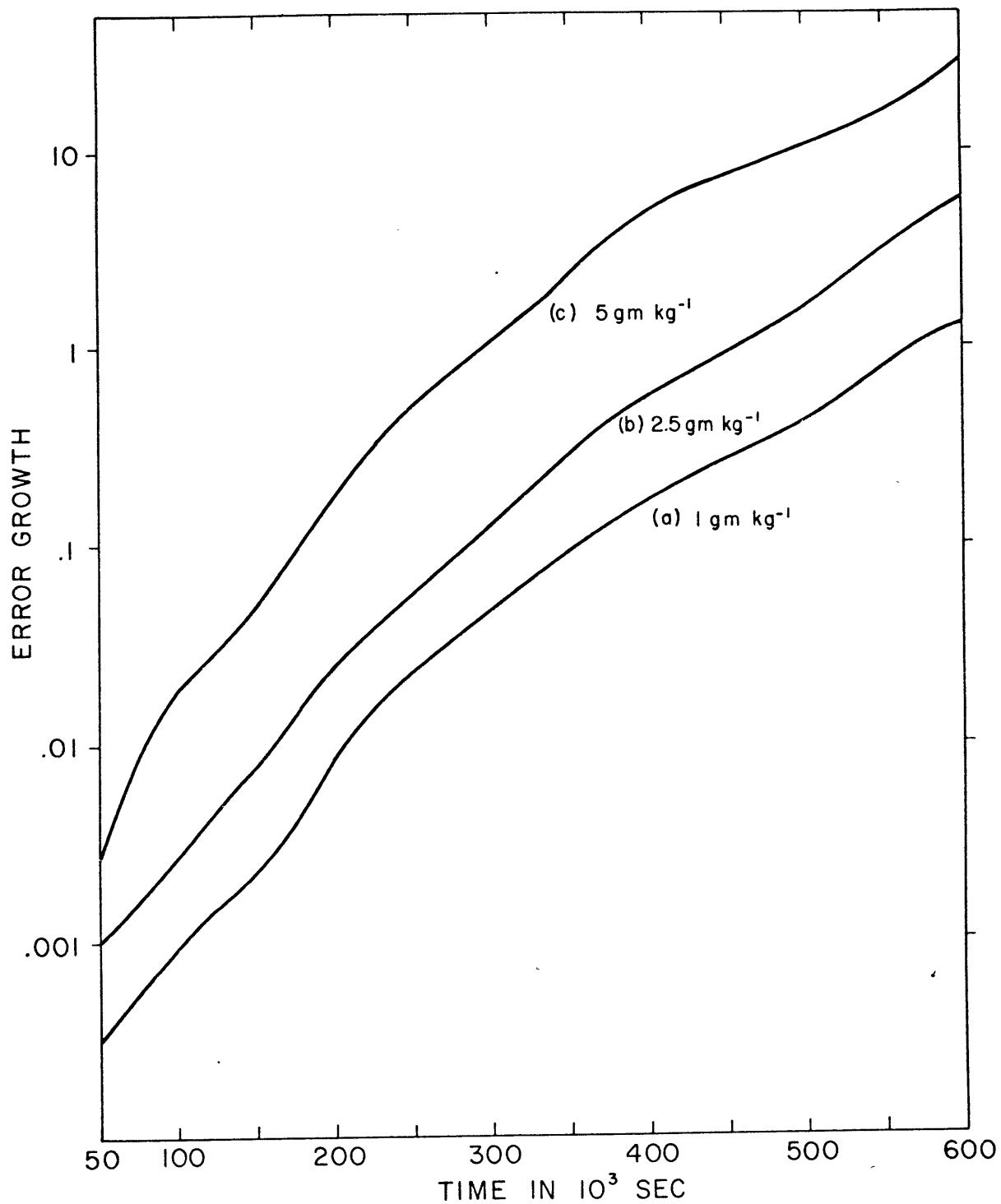


Figure 4-14. Error kinetic energy for runs with initial error in the absolute humidity fields for three different amplitudes.

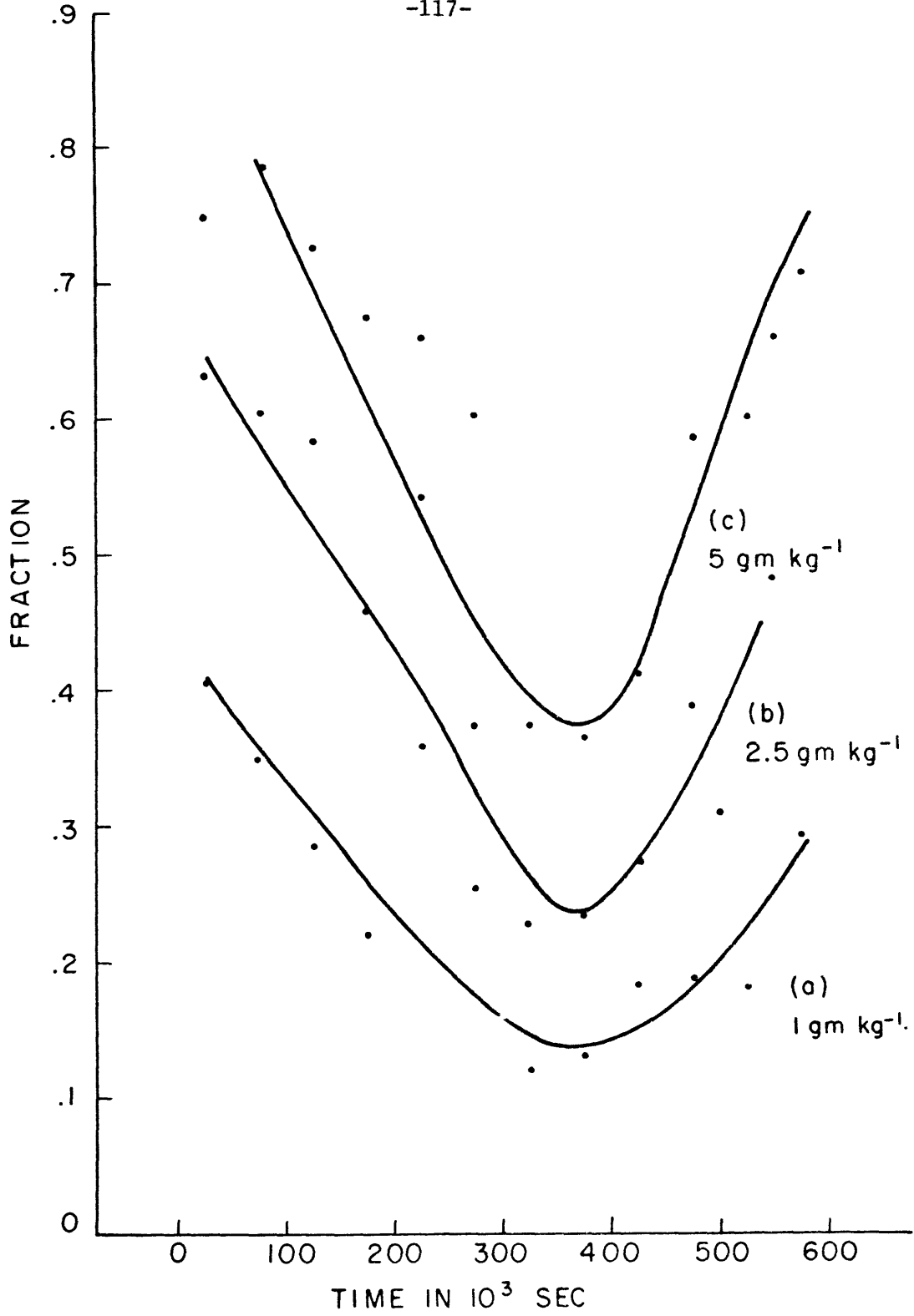


Figure 4-15. Fractional condensation disagreements for runs with initial error in the absolute humidity fields for three different amplitudes.

(c). All cases have decreasing fractional condensation disagreements until $t = 350 \times 10^3$ sec and thereafter increasing levels of disagreements.

Initially, since the fields of relative humidity have the error, the disagreement is high until enough condensation has occurred to bring the humidity pattern of the two simultaneous runs more nearly similar. A higher rate of fractional EKE growth occurs initially (from all to 350×10^3 sec) than occurs later ($350 \times 600 \times 10^3$ sec) in all three models (see Table 4-4 below), and this can be identified with the higher level of fractional disagreements and the condensation which is occurring in order to reduce the disagreement level.

Table 4-4 . Relative EKE values for $100-350 \times 10^3$ sec, and $350-600 \times 10^3$ sec.

<u>Amplitude of Δq</u>	<u>100-350</u>	<u>350-600</u>
1 gm kg ⁻¹	100.2	15.0
2.5 gm kg ⁻¹	110.2	20.2
5 gm kg ⁻¹	122.1	12.9

Although the fractional growth rate for EKE is greater in the case with initial errors in the humidity field compared with initial errors in the wind field, the size of the independent errors in the humidity field case remains smaller--a maximum factor of .05 for 1 gm kg^{-1} in the 16 x 17 case; however, the error levels of the initial humidity errors case becomes comparable to the error in the wind field at an initial error nearer to amplitude $\Delta q \approx 5 \text{ gm kg}^{-1}$.

Chapter 5. Statistics of error growths.

In order to generalize results about error growths in the dry and moist model cases, it was decided to run a larger number of simultaneous pairs in both the dry and moist states. The purpose of this was to demonstrate that the experiments described earlier were indeed "representative", and that no unusual behavior occurred by happenstance.

Because computer resources and time were limited, it was not possible to repeat each type of experiment many times in order to obtain statistics of error growths for each of the many studies done in earlier chapters. It is thus done as one experiment here, in order to observe error growth in general.

For the present study, 15 simultaneous pairs of runs were attempted in both the dry and moist cases, making 30 pairs in all. The pairs have initial states differing by a small amount in the wind field, and the identical state pairs are used as initial states in both the dry and moist cases. The models used were the 32 x 33 grid point (G) model without dissipation, and the bottom boundary temperature was set at $T = 297$ K. The initial states and their departures from each other were chosen from the unit normal random number generator (see Chapter 3). For this study, the following indices were computed:

- (1) Error kinetic energies (EKE) as defined in Chapter 2

$$\sum_{\substack{\text{grid} \\ \text{points}}} [\nabla(\psi_a - \psi_b) \cdot \nabla(\psi_a - \psi_b) + \nabla(\tau_a - \tau_b) \cdot \nabla(\tau_a - \tau_b)]$$

(2) Square errors in potential temperature (labeled STE) for both the dry and moist states

$$\sum_{\substack{\text{grid} \\ \text{points}}} [(\theta_{1a} - \theta_{1b})^2 + (\theta_{3a} - \theta_{3b})^2] / 2.$$

and (3) in the moist model, square errors in the absolute humidity field value of the lower level (labeled SHE)

$$\sum_{\substack{\text{grid} \\ \text{points}}} (q_{1a} - q_{1b})^2$$

Table 5-1 shows, for $t = 0$ to 600×10^3 sec in 100×10^3 sec time steps, the 15-pair root mean square wind error, measured in m sec^{-1} , derived from EKE, for the dry run in column 1, and that of the moist run in column 2. The root mean square temperature error in ($^{\circ}\text{K}$), derived from STE, of the dry run is in column 3, and that of the moist case is tabulated in column 4. The final column shows the root mean square error in absolute humidity in (gm kg^{-1}) . In this way, the average root-mean square wind error is $.43 \text{ m sec}^{-1}$ at $t = 0$ for both the dry and moist cases, and 4.69 and 5.17 m sec^{-1} at 600×10^3 sec for the dry and moist cases, respectively. Likewise, the root-mean square temperature error grows from 0 to 1.14 and $1.29 \text{ }^{\circ}\text{K}$ respectively for the dry and moist cases at 600×10^3 sec. The root-mean square humidity error is computed to be $.57 \text{ gm kg}^{-1}$ at 600×10^3 sec in the moist model, and it has started from zero.

The relative errors for both the EKE and STE in the moist and dry cases are pictured in Figures 5-1 and 5-2. For each of 15 pairs

Table 5-1. Average errors from sample of 15 pairs of runs.

Time (10 ³ sec)	RMS wind error dry (m sec ⁻¹)	RMS wind error moist (m sec ⁻¹)	RMS temp. error dry (°K)	RMS temp. error moist (°K)	RMS humidity error (gm kg ⁻¹)
0	.430	.430	.000	.000	.000
100	.528	.529	.071	.074	.058
200	.855	.870	.203	.219	.165
300	1.468	1.496	.414	.441	.288
400	2.413	2.524	.706	.783	.416
500	3.493	3.831	.960	1.062	.512
600	4.698	5.170	1.144	1.292	.571

Growth factors between 100 and 600 x 10³ sec in the value of

EKE-dry	EKE-moist	STE-dry	STE-moist	SHE-moist
79.0	95.5	263.5	304.8	96.6

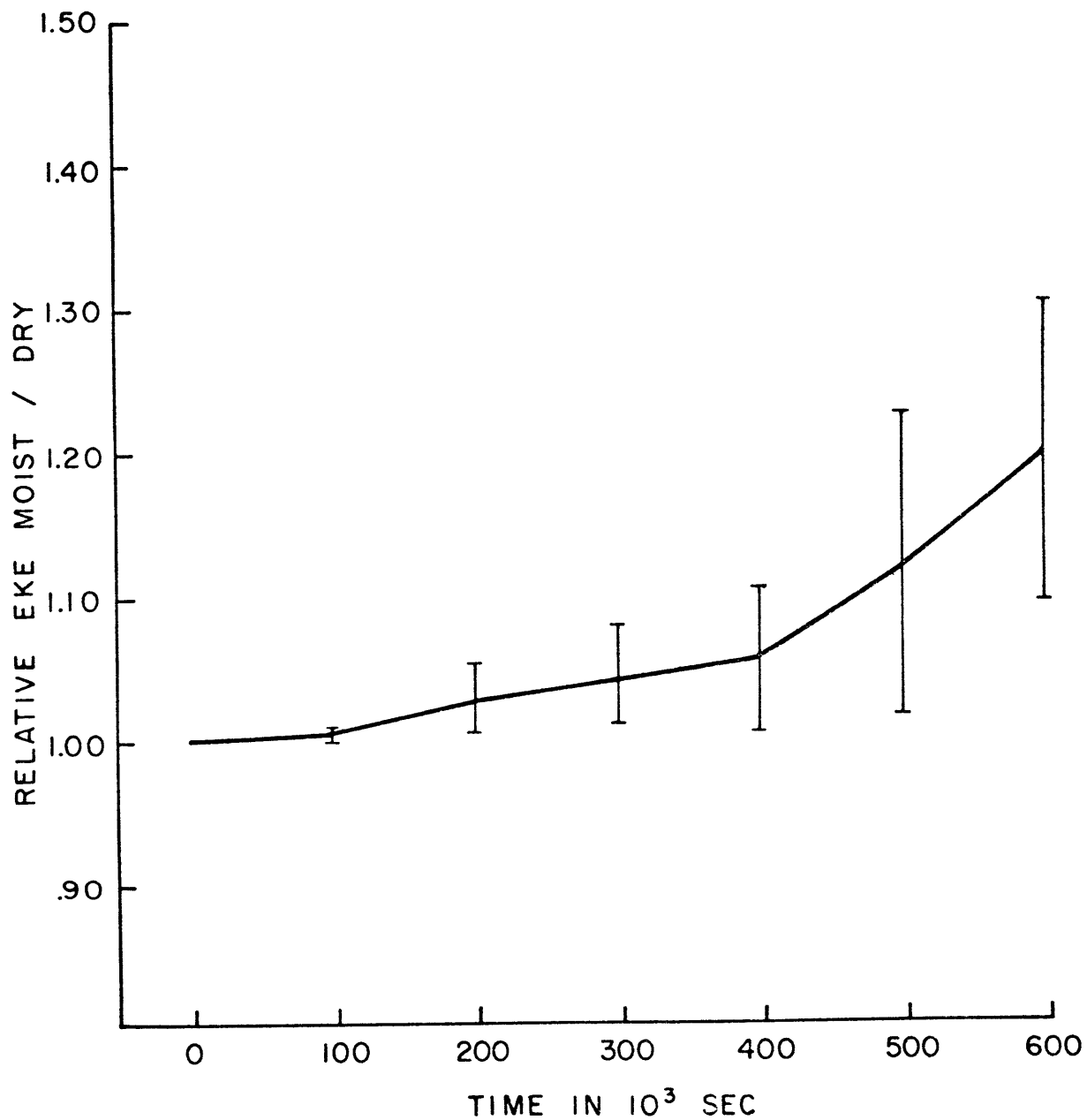


Figure 5-1. Relative error kinetic energies of the moist and dry cases for 15 pairs of runs.

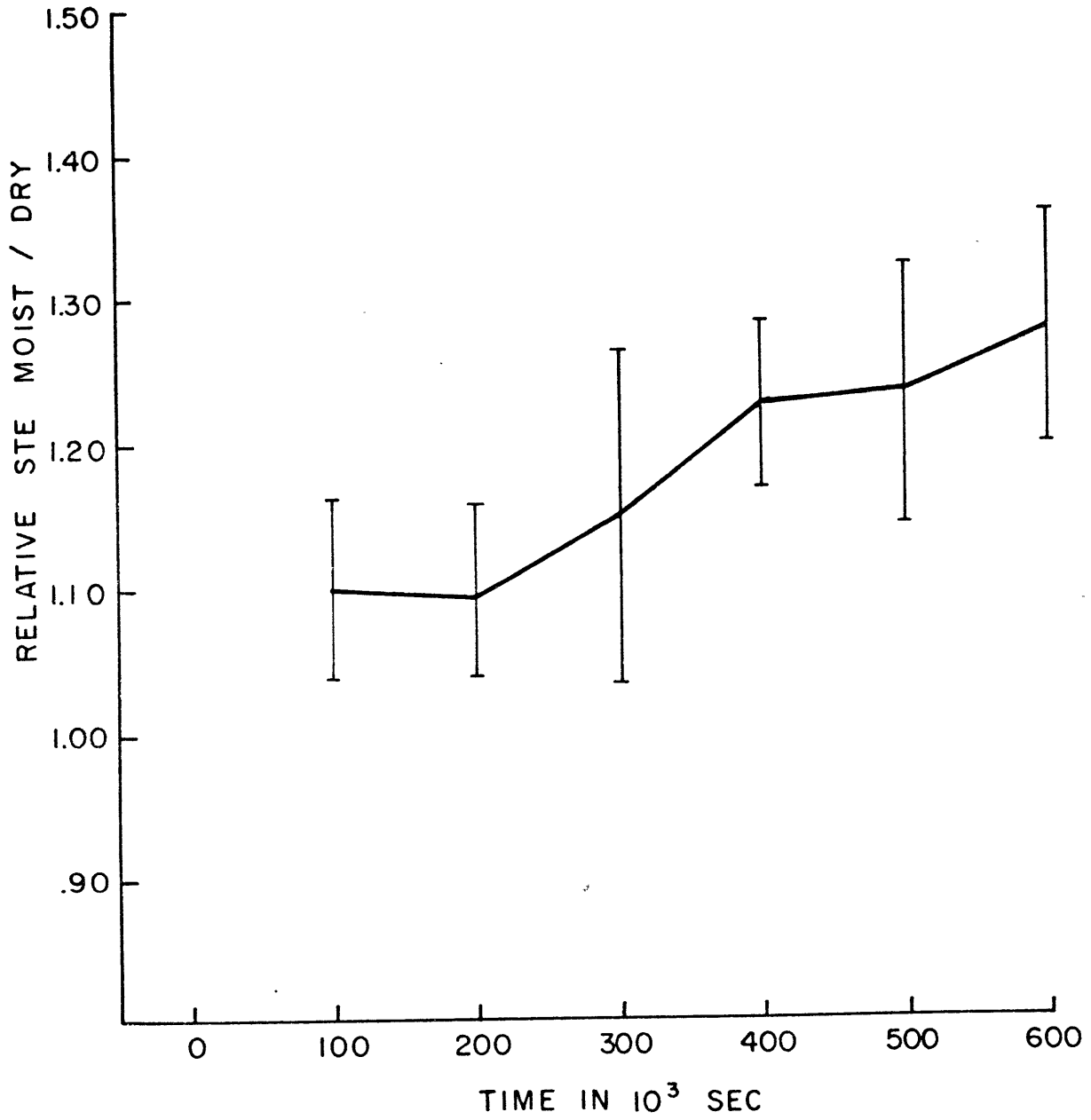


Figure 5-2. Relative square temperature errors of the moist and dry cases for 15 pairs of runs.

of cases the error fraction MOIST/DRY level are plotted for EKE and STE, and their mean values are connected and are the curves in the figures. Furthermore, a bar is used to denote the standard deviation values at each particular time step.

It can be seen that the MOIST/DRY fraction of EKE starts near 1 and grows to 1.20 by 600×10^3 sec. Although the standard deviation might appear to be large, the error in kinetic energy remains between 10% and 30% greater in the moist case over the dry case.

The average temperature error starts near 10% larger and grows to 28% larger in the moist compared with the dry case. At this point the standard deviation reveals the fact that $1 - \frac{1}{2e}$ or about 82% of the values would fall between 20% and 36% higher.

The results of the statistical study shown in this chapter would demonstrate that the earlier model state and the corresponding studies which were executed first, are indeed representative of the general types of error growths.

One can observe from this study that errors in temperatures seem to behave in similar fashion as errors in error kinetic energies in that they both grow to an order of 20% greater in the moist case over the dry case in the time period examined.

It is interesting to note the overall growth factors of error types, which are on the bottom line of Table 5-1. While EKE values are initially non-zero, those of STE and SHE are initially

zero, because error is inserted in the wind field only in this experiment. The entire STE and SHE errors are generated from the model itself, which between 100 and 600×10^3 sec grow in the factors shown.

The overall level of both temperature and humidity errors seem small, in comparison to acceptable levels in forecasts, although even a level of $.57 \text{ gm kg}^{-1}$ in error could make a critical difference between condensation occurring and not occurring.

The reason that this level does not grow too large is that when the absolute humidity of the two simultaneous runs diverge greatly, the higher one is bound to approach saturation value and at this point its growth would be terminated. The error growth would be transferred to STE and then into EKE growth, first from interactions between the temperature and humidity fields (release of latent heat), and then from interactions between the wind and temperature fields.

Chapter 6. Summary and conclusions.

A study of atmospheric predictability, which is an attempt to discover the maximum length of time it is possible to predict the physical properties and dynamics of a fluid, requires an understanding of the processes chiefly responsible for predictive error growths. Past investigations have usually set upper bounds on the order of two weeks for predictability times.

Most of these past theoretical and numerical studies have either treated the fluid as idealized and dry and subjected it to analysis of error growth of different scales, or have been experiments with complete versions of the large general circulation models, which use huge computer resources, and which attempt to be as complex as the atmosphere itself. Only a more direct and pointed investigation can lead to a better understanding of the generation of errors in atmospheric prediction.

Since it has often been concluded from these studies that there is an inherent limit to the predictability of the atmosphere due to small perturbations (or errors), and furthermore, that a reduction in error size, no matter how small, would still lead to the maximum error level within the same limiting time, one might just consider the problem solved. However, various physical processes can affect the growth of errors in different ways, in that the motions of a fluid might be more sensitive to the in-

correct prescription of certain of the physical processes than to others. After isolating the most sensitive parameters, then the future modeling work could be pointed in directions more in need of improvement, so that predictions might approach the maximum time possible.

It is hoped here to isolate the additional effects due to large scale moisture patterns in the equations of motion and thermodynamics of the atmosphere. A comparison with other studies might yield the relative importance of large scale moisture with other factors in the prediction problem.

The chief results of the study is that, while moisture creates additional error growth, and this is apparent after about 2 days, it is not quite as strong as had been earlier anticipated, being limited to an additional growth on the order of 20% more in both error kinetic energies and mean square temperature errors upon introduction of errors in the wind field.

The conclusions of this investigation were of course dependent upon the model used—a quasi-geostrophic grid point model of limited domain (Lorenz, 1960). Unfortunately, the domain limitation was a factor which it was hoped could be avoided, but the resolution desired (100 km) made a hemispheric size grid point model too costly in terms of computer time.

The chief asset of this model is the accurate description of the temperature and wind field in two layers in a model which was designed for the purpose of conserving energy. It has a static

stability which can change in location and time, and furthermore, it can be adapted easily to incorporate effects of latent heat release.

While many other studies treat models in the spectral form, it was decided here to use the grid-point form because of the moisture and the criterion for the process of condensation. While it is meaningful to describe winds and temperature processes in spectral form, it is questionable what the meaning of a condensation process would be in such a model type. The significance of the questions: (1) Is there rising motion? and (2) Is $q \geq .8 \times q_{sat}$? would be impossible to answer in spectral form because then condensation would end up occurring in regions where the atmospheric conditions are not at all appropriate.

In general, it was found that both the error kinetic energy and temperature errors behave in a similar fashion, and so it would not seem to be that critical which index was used as a measure of error growth.

In addition, various types of initial errors were inserted into the model in order to determine those which might cause greater and lesser growth of errors.

Initial errors which correspond to about $.5 \text{ m sec}^{-1}$ were placed in both the (1) average streamfunction field of the two levels, ψ , and (2) the field of the streamfunction difference of the two levels, τ , (which is related to the average temperature in the quasi-geostrophic model), and errors were placed in (3) the absolute humid-

ity field, q , of 1 gm kg^{-1} . The average errors generated into case (1) was a factor of 4 greater than those of case (2), and about a factor of 20 greater than those of case (3).

It has been shown that, on the basis of extended model runs using initial error values as stated in the previous paragraph, there is a level-off point in errors in the models, which are 16.3 days and 13.8 days respectively in the dry and moist models. This difference of 2.5 days represents the additional period of time which a dry atmosphere is predictable past that of a moist atmosphere, based upon the veracity of this model. Both values are near the two-week limit for predictability, though, which has often been cited in the literature.

Next, the question of whether the atmospheric model included enough factors within the context of the desire to determine predictability, without including ones which might mask error growths was considered. For example, it was concluded that the addition of Ekman pumping yielded small but similar additional error kinetic energies to both the dry and moist cases, and it is this type of process which might be eliminated.

In order to question the accuracy that the representative pairs of runs described in Chapter 3 had, it was decided to test 15 identical pairs of runs, with each differing by small sets of random numbers. The additional moist over dry effect was noted, but again, not in the magnitude which would lead one to believe that

large-scale moisture has an overwhelming effect on predictability.

It would probably be useful, in a further study, to try to include the effects of smaller scale moisture either by decreasing grid size more dramatically, or by actually parameterizing the moisture. Although it was found that in two different resolution models, the additional fraction of error growths were similar, the case might occur that even finer resolutions would lead to a different type of error growth. It is believed that this model does include all the important thermodynamic and dynamic effects which give an idea of how large-scale moisture influences error growths. No attempt, however, was made to include the radiative effects of water vapor and clouds in this study.

The actual condensation regions were studied, and it was determined that small initial errors in the wind field lead very rapidly to an incorrect prescription of the locations of condensation occurrence. Within 5 days, based upon small initial errors near $.5 \text{ m sec}^{-1}$ in the wind field, the regions of condensation in this particular study can be predicted to only within at least 200 km; however, this error is due only to the growth of small initial errors in the model itself, and it does not include the additional uncertainty which would be added if the errors from other factors were included such as those derived from the approximate nature of the physics and the simplification arising from a 2-level effect.

The spatial prediction of condensation grid points was examined by determining the agreement or disagreement of condensation at a grid point, and also the distance of a condensation point away from

the nearest predicted condensation point is studied. The distribution of this distance was examined and it was concluded that it can be approximated reasonably by a Gaussian form with standard deviation in distance which increases in time.

A general theory has been developed to calculate the additional uncertain energy which is transmitted to the system due to the release of latent heat, and it was noted that error energy is primarily added to the smallest scales of the spectrum. Since the highest wavenumber which is resolvable is that whose wavelength is twice the grid point distance (200 km), errors in still smaller scales can not be included in this method.

It is hoped that a more general theory can be developed which treats the generation of error energy in all scales more accurately. One suggestion for future work in the field is to adapt turbulence models in order to incorporate a phase-change variable simulating an inert and conservative quantity (carried along with the flow) during certain conditions, and its diminution with the release of heat when a certain threshold is reached. Furthermore, it is important to compare predictability studies with all types of additional factors present.

Although the inherent limits to prediction of atmospheric motions and thermodynamics do seem to exist due to the inevitable growth of small errors, a full understanding of the type of error growths is essential. When one is aware of what the best conditions

are, and the largest sources of predictive errors, then one can use that knowledge in order to predict with the maximum potential skill.

Appendix 1.

Approximation in the χ -equation.

The approximation $\nabla^2 \nabla \sigma \cdot \nabla \chi \ll \nabla^2 \sigma \cdot \nabla^2 \chi$ is justified

by an analysis of the error energy introduced by its use. If it

is assumed, one should look at Equation (2.1) to determine the

neglected difference in $\frac{\partial \theta}{\partial t}$ if the term $\nabla^2 \nabla \sigma \cdot \nabla \chi$

is omitted. This difference is

$$\Delta \theta = \frac{\partial \theta}{\partial t} = \nabla \sigma \cdot \nabla \chi$$

The equivalent difference in kinetic energy in a time step is

$$\Delta KE = \Delta \nabla \tau \cdot \nabla \tau = 2 \nabla \tau \cdot \Delta \nabla \tau$$

and with the help of equation (2.5) reduces to

$$\Delta KE = 2 \nabla \tau \cdot \frac{b_{cp}}{f} \nabla \theta = \frac{2 b_{cp}}{f} \nabla \tau \cdot \nabla (\nabla \sigma \cdot \Delta \nabla \chi) \quad (A1.1)$$

In order to determine ΔKE assume that the true solution to the χ -equation is $\chi_T = \chi_{APPROX} + \Delta \chi$ where

χ_{APPROX} is the solution to the χ -equation without the term $\nabla^2 \nabla \sigma \cdot \nabla \chi$. The χ -equation is as follows

$$\nabla^2 \nabla \cdot \sigma \nabla \chi - \frac{f^2}{b_{cp}} \nabla^2 \chi \quad (A1.2)$$

$$= \nabla^2 [J(\psi, \theta) + J(\tau, \sigma)] - \frac{f}{b_{cp}} [J(\psi, \nabla^2 \tau) + J(\tau, \nabla^2 \psi)]$$

Substituting χ_T and χ_{APPROX} into appropriate equations and

setting the results equal to each other, the following is obtained

$$\nabla^2 \sigma \nabla^2 \chi_{\text{APPROX}} - \frac{f^2}{bc_p} \nabla^2 \chi_{\text{APPROX}} = \nabla^2 \sigma \nabla \chi_T - \frac{f^2}{bc_p} \nabla^2 \chi_T \quad (\text{A1.3})$$

which, after noting that $\chi_T = \chi_{\text{APPROX}} + \Delta\chi$, it is found that

$$\nabla^2 \sigma \nabla^2 (\Delta\chi) - \frac{f^2}{bc_p} \nabla^2 (\Delta\chi) = - \nabla^2 \sigma \cdot \nabla \chi_T \quad (\text{A1.4})$$

Now it is desirable to estimate $\Delta\chi$. Since the second term on the right hand side of (A1.4) is smaller in magnitude than the first, it will be neglected.

Since σ is the static stability, it is close to a constant value for the region and departures from its mean are small, i.e. $\sigma = \bar{\sigma} + \sigma'$, where $\frac{\sigma'}{\bar{\sigma}} = O(0.1)$. But values for χ vary comparably to its mean and so $\chi = \bar{\chi} + \chi'$ where $\frac{\chi'}{\bar{\chi}} = O(1)$. Relation (A1.4) when used to approximate $\Delta\chi$ yields

$$\Delta\chi \approx \frac{\sigma'}{\bar{\sigma}} \chi$$

because if σ is after a ∇ sign, it lowers the order of magnitude, but if χ is after a ∇ sign, its order of magnitude remains the same.

Thus relation (A1.1), when evaluated yields

$$\begin{aligned} \Delta KE &= 2 \frac{bc_p}{f} \nabla \tau \cdot \nabla \left(\nabla \sigma \cdot \frac{\sigma'}{\bar{\sigma}} \nabla \chi \right) \\ &= 2 \times 10^{-6} \frac{\text{joule}}{\text{kg sec}} \end{aligned} \quad (\text{A1.5})$$

when typical values of the parameters are inserted.

If the typical flow is represented by $\psi + \psi_{pert}$ for a perturbation error, the kinetic energy of perturbation is $\Delta \nabla \psi \cdot \nabla \psi = 2 \nabla \psi \cdot \nabla \psi_{pert}$; for the perturbation .1 of the flow values, for typical values an estimation of the kinetic energy of perturbation is

$$\Delta KE_{pert} = 20 \frac{\text{joule}}{\text{kg}} \quad (\text{A1.6})$$

Comparing values (A1.5) and (A1.6), it would take on the order of 10^7 sec for errors due to the neglect of the second term in the equation to be comparable to the perturbation kinetic energy. Since the model will be run only to 10^6 sec at the maximum, the above approximation can be made.

Appendix 2.

The best exponential and square exponential fit for a data set.

It is desired to determine a best least-square fit for a certain two-parameter function $y(x) = h(b, c, x)$ for a set of points $(x_i, y_i) \quad i=1, N$. The general least-square condition is that

$$\sum_{i=1}^N (y_i - h(b, c, x_i))^2 = m = \text{minimum} \quad (\text{A2.1})$$

(see, for example, Hamming, pp. 244-248.)

This minimum condition is satisfied if

$$0 = \frac{\partial}{\partial b} \sum_{i=1}^N (y_i - h(b, c, x_i))^2 = \sum_{i=1}^N 2(y_i - h(b, c, x_i)) \left(-\frac{\partial h}{\partial b}\right) \quad (\text{A2.2})$$

and
$$0 = \frac{\partial}{\partial c} \sum_{i=1}^N (y_i - h(b, c, x_i))^2 = \sum_{i=1}^N 2(y_i - h(b, c, x_i)) \left(-\frac{\partial h}{\partial c}\right) \quad (\text{A2.3})$$

Thus this problem reduces to the case of two equations in the two unknowns b and c. In the case where $h(b, c, x)$ is not a linear function of b and c, the two associated equations are non-linear and might possibly require numerical techniques to solve.

If it is desired to fit $h(x) = be^{-cx}$, the two associated equations become

$$0 = \sum_{i=1}^N (y_i - be^{-cx_i}) e^{-cx_i} \quad (\text{A2.4})$$

$$0 = \sum_{i=1}^N (y_i - be^{-cx_i}) be^{-cx_i} x_i \quad (\text{A2.5})$$

Both Equation (A2.4) and (A2.5) can be solved for b:

$$b = \frac{\overline{y_i e^{-cx_i}}}{\overline{e^{-2cx_i}}} \quad (A2.6)$$

$$b = \frac{\overline{y_i x_i e^{-cx_i}}}{\overline{x_i e^{-2cx_i}}} \quad (A2.7)$$

where the overbar $\overline{\quad}$ refers to a summation of i from 1 to N . A table can be produced for successively incremented values of c within a proscribed range. In this manner, b can be computed from both Equations (A2.6) and (A2.7). When the two values for b are equal, the corresponding value for c and that value for b are used in the two parameter fit.

In order to fit the data to the function $h(x) = b e^{-cx^2}$ a similar procedure as the above is followed, but using the two equations

$$0 = \sum_{i=1}^N (y_i - b e^{-cx_i^2}) e^{-cx_i^2} \quad (A2.8)$$

$$0 = \sum_{i=1}^N (y_i - b e^{-cx_i^2}) b x_i^2 e^{-cx_i^2} \quad (A2.9)$$

which lead to two relations for b , similar to (A2.6) and (A2.7)

$$b = \frac{\overline{y_i e^{-cx_i^2}}}{\overline{e^{-2cx_i^2}}} \quad (A2.10)$$

$$b = \frac{\overline{y_i x_i^2 e^{-cx_i^2}}}{\overline{x_i^2 e^{-2cx_i^2}}} \quad (A2.11)$$

Spectral decomposition of error impulses.

For two simultaneous models, A and B, each case of condensation at a grid point represents an impulse of energy into the system for either model. If an impulse occurs in one model and not in the other, error energy is being imparted into the system. The assumption is made that the condensation occurrence is a function of distance in model B from a condensing grid point in model A. The method of determining the decomposition into spectral components is the subject of this appendix. First, it is instructive to specify the method if the domain were a one-dimensional set of grid points, before discussing the analagous two-dimensional case.

I. One-dimensional cyclic case.

Assume that the domain is of one dimension in the x-direction, cyclic, and of length $N\Delta x$ and that a grid point m_0 occurs at a distance $x_0 = m_0 \Delta x$. If condensation occurs in model A at the point m_0 , then there is a probability of condensation occurrence in model B at the same time at a grid point m which is related to its distance away from m_0 . The probability of condensation occurring in model B at a grid point m (or at x) where $x = m \Delta x$ is $p(x, x_0)$. In the case where the distribution is represented as a Gaussian function of distance away from m_0 , the probability $p(x, x_0)$ can be written as

$$P(x, x_0) = \frac{1}{a\sqrt{2\pi}} \int_{x - \frac{\Delta x}{2}}^{x + \frac{\Delta x}{2}} e^{-\left(\frac{|x-x_0|}{a}\right)^2} dx$$

Here $|x-x_0|$ refers to the smallest distance from x to x_0 taking into account the cyclic nature of the domain.

If an impulse (condensation) occurs in model A at m_0 , firstly it will be considered to be of magnitude one, and thus $F_{m_0} = 1$. The contribution of this impulse to the n th component of the spectrum of model A is

$$G_{nA} = F_{m_0} e^{2\pi i m_0 n / N} = e^{2\pi i m_0 n / N}$$

where G_n is the spectral component of wavenumber n , $G_n = \sum_{m=0}^{N-1} F_m e^{2\pi i m n / N}$.

The corresponding impulse to the n th spectral component in model B is determined in the following manner. Each grid point $(0, N-1)$ can have a condensation impulse according to the probability $p(m, m_0)$ and so the expected contribution from the sum of impulses is

$$\begin{aligned} \langle G_{n, m_0 B} \rangle &= \sum_{m=0}^{N-1} p(m, m_0) e^{2\pi i m n / N} \\ &= \sum_{m=0}^{N-1} \frac{1}{a\sqrt{2\pi}} \int_{x_m - \frac{\Delta x}{2}}^{x_m + \frac{\Delta x}{2}} dx e^{-\left(\frac{|x-x_0|}{a}\right)^2} e^{2\pi i m n / N} \end{aligned}$$

The brackets $\langle \rangle$ around the symbol G_{n, m_0} refer to its expected value.

In addition to the probability distribution of condensation points, there is an additional factor in the magnitude of the impulse. This comes from the fact that condensation will occur proportionately to the vertical velocity (actually to ω), if ω is of one sign (negative) and that condensation will not occur at all if ω is of the other sign. The square brackets around ω refer to:

$$[-\omega] = -\omega \quad \text{if} \quad \omega < 0$$

$$[-\omega] = 0 \quad \text{if} \quad \omega \geq 0$$

So to the expected value of the nth spectral component of model B corresponding to condensation at m , the additional factors are added

$$\langle G_{n,m_B} \rangle = \langle \rho(m, m_0) [-\omega_m] e^{2\pi i m n / N} \rangle$$

For an impulse at m_0 , then there is an nth spectral component for both model A and B and if the impulse can occur at grid point m with the magnitude $[-\omega_m]$, error energy will be imparted to the system's nth component in the amount $\|G_{nA} - G_{nB}\|$ where $\|\dots\|$ refers to the magnitude of the difference between the two energies of models A and B.

Furthermore, a net expected value of the error impulse spectrum is determined from a grand ensemble in which model A has condensation at points 0 to $N-1$ at magnitude 1 and for each m in model A, model B has corresponding expected condensation. The grand ensemble expected value for component n is noted by G_n^* and is computed in the following manner:

$$G_n^* = \frac{1}{N} \sum_{m_0=0}^{N-1} \|G_{nA} - G_{nB}\|$$

II. Two-dimensional singly cyclic case.

The case of a two-dimensional domain, which is an $M \times N$ grid point region cyclic in the x-direction is analagous to that in one-dimension for two simultaneously running models A and B. At each point (m_{ox}, m_{oy}) in model A, condensation may occur, and furthermore, considering the occurrence at (m_{ox}, m_{oy}) the probability of condensation occurrence is a certain distribution $p(x, y, x_0, y_0)$ which is assumed to be a function of the difference in distance between (m_{ox}, m_{oy}) and (m_x, m_y) . If $y_0 = m_{oy} \Delta y$ and $x_0 = m_{ox} \Delta x$, the distance d is

$$d = |(x_0, y_0) - (x, y)|$$

which is measured considering the singly cyclic region.

The model A impulse of the two-dimensional case has spectral component n_x, n_y

$$G_{n_x, n_y, A} = e^{2\pi i (\vec{n} \cdot \vec{m}_0) / N}$$

where $\vec{n} \cdot \vec{m}_0 = n_x m_{0x} + n_y m_{0y}$.

The probability that condensation will occur at a location in model B is considered to be dependent upon only the distance from the condensation. If again, the function is considered a Gaussian,

$$\begin{aligned} p(x, y, x_0, y_0) &= \frac{1}{a^2 \cdot 2\pi} \int_{y-\frac{\Delta x}{2}}^{y+\frac{\Delta x}{2}} \int_{x-\frac{\Delta x}{2}}^{x+\frac{\Delta x}{2}} \exp\left[-\left(\frac{x-x_0}{a}\right)^2 + \left(\frac{y-y_0}{a}\right)^2\right] dx dy \\ &= \left(\frac{1}{a\sqrt{2\pi}} \int_{x-\frac{\Delta x}{2}}^{x+\frac{\Delta x}{2}} \exp\left[-\left(\frac{x-x_0}{a}\right)^2\right] dx\right) \left(\frac{1}{a\sqrt{2\pi}} \int_{y-\frac{\Delta x}{2}}^{y+\frac{\Delta x}{2}} \exp\left[-\left(\frac{y-y_0}{a}\right)^2\right] dy\right) \end{aligned}$$

Thus the n_x, n_y spectral component for model B is computed as follows for each (m_{0x}, m_{0y})

$$\langle G_{n_x, n_y, m_{0x}, m_{0y}, B} \rangle = \sum_{m_x, m_y=0}^{N-1} p(x, y, x_0, y_0) \left[-\omega_n \epsilon_{m_y} \right] \cdot \exp(2\pi i \vec{m} \cdot \vec{n} / N)$$

The spectral component of the error impulse is obtained by means of the difference between the expected values of models A and B, that is,

$$\| G_A - \langle G_B \rangle \|$$

Furthermore, a grand ensemble analagous to that in the one-dimensional case is obtained

$$G_{n_x n_y}^* = \frac{1}{N^2} \sum_{m_{0x}, m_{0y}=1}^{N-1} \|G_A - G_B\|$$

In addition, the average value for the spectral component of a given scalar wavevector of magnitude $(n_x^2 + n_y^2)^{1/2}$ can be obtained by combining the value of each spectral component to a distribution dependent upon the magnitude of the scalar component's wavevector. This is known as the expected scalar wavevector of the grand ensemble $|G^*|$.

Appendix 4

Derivation of the increase of moisture in saturated air.

The following derivation of the time change of water vapor is adapted from Haltiner (1971).

The equation of continuity of water vapor is as follows

$$\frac{\partial \rho_v}{\partial t} = -\nabla \cdot \rho_v V + S \quad (\text{A4.1})$$

where S represents any sources or sinks of water vapor in mass per unit volume per unit time and ρ_v is the density of water vapor, while the equation of continuity of the total mass of air is

$$\frac{\partial \rho}{\partial t} = -\nabla \cdot (\rho V) \quad (\text{A4.2})$$

and ρ and ρ_v are related by $\rho_v = \rho q$ where q is the specific humidity. Combining equations (A4.1) and (A4.2), the following result is obtained for the increase of specific humidity

$$\frac{dq}{dt} = \frac{\partial q}{\partial t} + V \cdot \nabla q = \frac{S}{\rho} \quad (\text{A4.3})$$

The decrease of water vapor can be considered to result only through condensation. Taking into account the relation between the saturation specific humidity q_s , and the saturation vapor pressure e_s ,

$$q_s = \frac{0.622 e_s}{P} \quad (\text{A4.4})$$

the following results through differentiation of (A4.4)

$$\frac{1}{q_s} \frac{dq_s}{dt} = \frac{1}{e_s} \frac{de_s}{dt} - \frac{\omega}{p} \quad (\text{A4.5})$$

The Clausius-Clapeyron relationship for the vapor pressure during phase change is as follows:

$$\frac{de_s}{e_s} = \frac{L}{R_v} \frac{dT}{T^2} \quad (\text{A4.6})$$

where R_v is the gas constant of water vapor and so

$$\frac{1}{q_s} \frac{dq_s}{dt} = \frac{L}{R_v T^2} \frac{dT}{dt} - \frac{\omega}{p} \quad (\text{A4.7})$$

The first law of thermodynamics relates the potential temperature change to the latent heat release and the following is obtained therefrom

$$-L \frac{dq_s}{dt} = c_p \frac{dT}{dt} - \frac{RT}{p} \omega \quad (\text{A4.8})$$

One equation results from (A4.7) and (A4.8) when $\frac{dT}{dt}$ is eliminated

$$\frac{dq_s}{dt} = \frac{\delta F}{p} \omega \quad (\text{A4.9})$$

where

$$F = q_s T \left(\frac{L R - c_p R_v T}{c_p R_v T^2 + q_s L^2} \right) \quad (\text{A4.10})$$

Included is the additional factor δ which is 1 if condensation can occur, that is, if $\omega < 0$ and $q_s \geq 80\%$ of relative humidity and δ is 0 otherwise.

References.

- Arakawa, A., 1966, "Computational design for long-term integration of the equations of atmospheric motion," J. Computational Physics, 11, pp. 119-143.
- Arakawa, A., 1970, "Numerical simulation of large-scale atmospheric motions," Numerical Simulation of Field Problems in Continuum Physics, Amer. Math. Soc., Providence, R.I., pp.24-40.
- Blumen, W., 1976, "Experiments in atmospheric predictability," J. Atmo. Sci., 33, pp.161-169.
- Charney, J., et. al., 1966, "The feasibility of a global observation and analysis experiment," Bull. Amer. Meteor. Soc., pp.200-220.
- Defant, A., 1961, Physical Oceanography, v.1, Pergamon Press, New York, pp. 109-110.
- Fleming, R., 1971, "On stochastic dynamic prediction, II. Predictability and utility," Mon. Wea. Rev., 99, pp. 927-938.
- Haltiner, G., 1971, Numerical Weather Prediction, John Wiley and Sons- New York.
- Hamming, R., Numerical Methods for Scientists and Engineers, 1962, McGraw Hill, New York.

Hildebrand, F., 1956, Introduction to Numerical Analysis, McGraw Hill, New York.

Holloway, J. and Manabe, S., 1971, "Simulation of climate by a global general circulation model: I. Hydrological cycle and heat balance," Mon. Wea. Rev., 99, pp. 335-370.

Holton, An Introduction to Dynamic Meteorology, 1972, Academic Press, New York.

Howcraft, J., 1966, "Fine-mesh limited area forecasting model," Air Weather Service Technical Report 188, pp. 71-75.

International Mathematical and Statistical Libraries, Inc., 1974, Houston, Texas.

Jastrow, R. and Halem, M., 1970, "Simulation studies related to GARP," Bull. Amer. Meteor. Soc., 51, pp. 490-513.

Jastrow, R. and Halem, M., 1973, "Simulation studies and the design of the first GARP experiment," Bull. Amer. Meteor. Soc., 54, pp. 13-21.

Kasahara, A. and Washington, W., 1971, "General circulation experiments with a six-layer NCAR model, including orography, cloudiness

and surface temperature calculations, J. Atmo. Sci., 28, pp. 657-701.

Kasahara, A., 1972, "Simulation experiments for meteorological observing systems during GARP," Bull. Amer. Meteor. Soc., 53, pp. 252-264.

Knighting, E., 1960, "On the grid length to be adopted in numerical weather prediction," Quar. J. Roy. Meteor. Soc., 86, pp.265-270.

Kraichnan, R., 1970, "Instability in fully developed turbulence," Phys. Fluids, 13, 569-575.

Krishnamurti, T. and Maxim, W., 1971, "On parameterization of convective and non-convective latent heat release," J. App. Meteor., 10, pp. 3-13.

Leith, C., 1964, Numerical simulation of the earth's atmosphere. Report under contract No. W-7405-eng-48, Lawrence Livermore Lab., Livermore, Calif., Univ. of Calif.

Leith, C., 1971, "Atmospheric predictability and two-dimensional turbulence," J. Atmo. Sci., 28, pp. 145-161.

Leith, C. and Kraichnan, R., 1972, "Predictability of turbulent flows," J. Atmo. Sci., 29, 1041-1058.

- Lorenz, E., 1960, "Energy and numerical weather prediction," Tellus, 12, pp. 364-373.
- Lorenz, E., 1963, "Deterministic non-periodic flow," J. Atmo. Sci., 20, pp. 130-141.
- Lorenz, E., 1965, "A study of the predictability of a 28-variable atmospheric model," Tellus, 17, pp. 321-333.
- Lorenz, E., 1969a, "Atmospheric predictability as revealed by naturally occurring analogues," J. Atmo. Sci., 26, pp. 636-646.
- Lorenz, E., 1969b, "The predictability of a flow which possesses many scales of motion," Tellus, 21, pp. 289-306.
- Lorenz, E., 1971, "An N-cycle time differencing scheme for stepwise numerical integration," Mon. Wea. Rev., 99, pp. 644-648.
- Lorenz, E., 1973, "On the existence of extended range predictability," J. App. Meteor., 12, pp. 543-546.
- Manabe, S., et. al., 1970, "Simulated climatology of a general circulation model with a hydrological cycle," Mon. Wea. Rev., 98, pp. 175-211.

Mintz, Y., 1965, "Very long-term global integration of the primitive equations of atmospheric motion," Pro. WMO/IUGG Symp. on Research and Development, Aspects of long-range forecasting, Boulder, Colorado, 1964, WMO Tech. Note 66, pp.141-167.

Mintz, Y., 1968, "Very long-term global integration of the primitive equations of atmospheric motion: An experiment in climate simulation," Meteor. Monogr., 8, No. 30, pp. 20-36.

Miyakoda, K., et. al., "The effect of horizontal grid resolution in an atmospheric model," J. Atmo. Sci., 28, pp. 481-499.

Phillips, N., 1973, "Principles of large scale numerical weather prediction," Dynamic Meteorology, Reidel, Dordrecht, Holland.

Richards, T., 1970, "The Great Lakes as models for sea-air interaction studies--Techniques for estimating evaporation," Meteorological Service of Canada Report.

Robinson, G., 1971, "The predictability of a dissipative flow," Quar. J. Roy. Meteor. Soc., 97, pp. 300-312.

Smagorinsky, J., 1963, "General circulation experiments with the primitive equations. I. The basic experiment," Mon. Wea. Rev., 91, 99-164.

- Smagorinsky, 1969, "Problems and promises of deterministic extended range forecasting," Bull. Amer. Meteor. Soc., 50, pp. 286-311.
- Somerville, R., et. al., 1974, "The GISS model of the global atmosphere," J. Atmo. Sci., 31, pp. 84-117.
- Sweet, R., 1974, "A generalized cyclic reduction algorithm," SIAM Journal on Numerical Analysis, 11, pp.506-520.
- Thompson, P., 1957, "Uncertainty of initial state as a factor in the predictability of large scale atmospheric flow patterns," Tellus, 9, 275-295.
- Walsh, J., 1967, Numerical Analysis; an Introduction, Thompson Book Company, Washington.
- Warshaw and Rapp, 1973, "An experiment on the sensitivity of a global circulation model," J. App. Meteor., 12, pp. 43-49.
- Wellck, R., et. al., 1971, "The effect of horizontal resolution in a finite-difference model of the general circulation," Mon. Wea. Rev., 99, pp. 673-683.

Williamson, D. and Kasahara, A., 1971, "Adaption of meteorological variables forced by updating," J. Atmó. Sci., 28, 1313-1324.

Young, D., 1954, "Iterative methods for solving partial difference equations of the elliptic type," American Mathematical Society Transactions, 76, pp. 92-111.

Biographical note.

David Alan Salstein was born May 17, 1950 in New York City, the son of William and Beatrice Cohen Salstein. His early schooling was in the public schools of New York City, and he graduated from Stuyvesant High School.

He received an S.B. degree from M.I.T. in mathematics in 1972 and an S.M. degree from M.I.T. in meteorology in 1973. He is a member of Phi Beta Kappa and Sigma Xi.

He has worked at the Atomic Energy Commission, Risø, Roskilde, Denmark in the micrometeorological division and the Meteorological Institute, University of Munich, Germany. He will commence a fellowship in the Advanced Study Program, National Center for Atmospheric Research, Boulder, Colorado in October 1976.

His publications to date include:

- (1) Salstein, D.A., "Channel flow driven by a stationary thermal source," Tellus, 26, 1974, pp. 638-651.
- (2) Starr, V.P., Anati, D.A. and Salstein, D.A., "Effectiveness of controlled convection in producing precipitation," Journal of Geophysical Research, 79, 1974, pp. 4047-4052.
- (3) Salstein, D.A., "Effects of moisture upon atmospheric predictability," Joint DMG/AMS International Conference on Simulation of Large-Scale Atmospheric Processes, August 30-September 4, 1976, Hamburg, Germany, Proceedings.